TriDurLE

National Center for Transportation Infrastructure Durability & Life-Extension

Project ID: 2021-SDSU-01

Drone-Based Measurements for Bridge Field Testing – Development Phase

Final Report

by

Giovanni Lavezzi[a], Marco Ciarcià[a], Kwanghee Won[b], and
Mostafa Tazarv[c]

Departments of Mechanical Engineering [a], Electrical Engineering and Computer Science [b], and
Civil and Environmental Engineering [c]
South Dakota State University
Brookings, South Dakota

for

National University Transportation Center TriDurLE
Department of Civil & Environmental Engineering
405 Spokane Street PO Box 642910
Washington State University Pullman, WA 99164-2910

September 12, 2023

ACKNOWLEDGEMENTS

The work presented in this report was conducted with a support from South Dakota State University and the National Center for Transportation Infrastructure Durability and Life-Extension (TriDurLE), a University Transportation Center (UTC) funded by the U.S. Department of Transportation. The contents of this report reflect the views of the authors, who are responsible for the facts and accuracy of the information presented.

DISCLAIMER

ABSTRACT

More than 40% of the US in-service bridges are at least 50 years old, 10% are posted with limited passing loads, and the cost to repair the US bridges in their current condition is $125 billion. Load rating is usually performed to assess the performance and capacity of old bridges and is carried out either analytically or experimentally. Despite several advantages of bridge field testing, it is not a common practice for the evaluation of bridge performance. Instead, the analytical load rating is more common. One main reason is the cost of field operations and instrumentation. One effective way to reduce the inspection cost is to utilize new technologies such as drones. Furthermore, recent studies have confirmed the feasibility of field-testing bridges using computer vision in which video recording from fixed cameras are used to extract bridge response with no need to use conventional sensors.

The main goal of this project, which is the first phase of a two-phase study, is to develop frameworks and necessary tools to field test bridges using a novel non-contact measurement technique in which instead of conventional displacement or strain sensors and data acquisition system (DAQ), digital image correlation (DIC), uncrewed aerial vehicles (UAVs or drones), opensource computer programs, and cost-effective cameras are utilized to estimate bridge structural responses. The development of the proposed measurement technique including mission strategy, camera system, DIC software, drones and their payloads is presented. The accuracy of the proposed measurement technique is evaluated through more than 70 experiments on a truss bridge in a laboratory.

The proposed DIC-UAV based displacement measurement strategy and computational tools were found feasible with submillimeter accuracies, significantly advancing the state-of-the-art methodologies.

TABLE OF CONTENTS

ABBREVIATIONS

AASHTO	American Association of State Highway and Transportation Officials
AI	Artificial Intelligence
AOI	Area Of Interest
ArUco	Augmented Reality University of Cordoba
BDI	Bridge Field
BLDC	Brushless Direct Current
°C	Degree Celsius
CCD	Charge-Coupled Device
CMOS	Complementary Metal Oxide Semiconductor
DAQ	Data Acquisition System
deg	Degree
DIC	Digital Image Correlation
DSfM	Dense Structure-from-Motion
ESC	Electronic Speed Controller
°F	Degree Fahrenheit
FOV	Field-of-View
FPS	Frames Per Second
FPV	First Person View
ft	Feet
GB	Gigabyte
GNSS	Global Navigation Satellite System
GPIO	General-Purpose Input/Output
GPS	Global Positioning System
HD	High Definition
HDMI	High-Definition Multimedia Interface
HPF	High-Pass Filter
HQ	High Quality
ID	Identity
IM	Image Mosaicking
in.	Inch
IR	Infrared
kg	Kilogram
lbs.	Pound
LDV	Laser Doppler Vibrometer
LFP	Lithium Iron Phosphate
LiPo	Lithium Polymer
LiDAR	Light Detection and Ranging
LPF	Low-Pass Filter
LVDT	Linear Variable Differential Transformers
MAC	Modal Assurance Criterion
m	Meter
mAh	Milliampere hour
min	Minute
mm	Millimeter
MP	Megapixel

mph	Miles per hour
NiMH	Nickel–Metal Hydride
No.	Number
NUCE	National University of Civil Engineering
OpenCV	Open Source Computer Vision Library
PC	Personal Computer
PM	Potentiometer
PWM	Pulse Width Modulation
RAM	Random Access Memory
RMS	Root Mean Square
RMSE	Root Mean Square Error
ROI	Region Of Interest
RTK	Real Time Kinematics
SDSU	South Dakota State University
sec	Second
SIFT	Scale Invariant Feature Transform
SSD	Solid-State Drive
UAV	Unmanned Aerial Vehicle
USB	Universal Serial Bus
VGG	Visual Geometry Group
VVS	Virtual Visual Sensors
μm	Micrometer

LIST OF TABLES

LIST OF FIGURES

EXECUTIVE SUMMARY

ES.1 Introduction

More than 40% of the US in-service bridges are at least 50 years old, and the cost to repair the US bridges in their current condition is $125 billion. With the current budget allocation, it will take 50 years to repair the US bridges assuming no further deterioration. When a bridge is old or deteriorated, the evaluation of the load carrying capacity of the bridge, usually referred to as “load rating”, is necessary to ensure the safety of the traveling public and to prevent excessive bridge damage and, possibly, collapse. Even though field testing offers actual insights into bridge behavior, it is not a common practice for bridge evaluation. Instead, the analytical load rating is often used. One main reason is the cost related to field operations.

One effective way to reduce the inspection cost is to utilize new technologies such as drones or unmanned aerial vehicles (UAVs). During an inspection, drones increase accessibility and safety, and may carry different types of sensors such as cameras, infrared cameras, stereo-vision cameras, and lidar cameras. By using these sensors mounted on drones, one may generate 3D models of bridges, detect damages (cracking, spalling, etc.) through computer vision and artificial intelligence enabled software, or obtain new information about bridges such as displacements, stresses, and strains. Digital image correlation (DIC) allows extracting full-field displacements and strains from images and videos. The present project was to develop a novel solution that combines the use of drones equipped with cameras and a computer vision system to perform drone-based displacement measurements for bridge field testing.

ES.2 Objectives

The main goal of this project, which is the first phase of a two-phase study, was to develop computer tools to field test bridges using drones and DIC. To achieve the project goal, several camera configurations were studied to determine the best camera candidates for use in DIC-drone applications. Subsequently, different mission strategies were proposed in which a drone (or a fleet of drones) equipped with a set of cameras is deployed to perform bridge field testing using DIC software, instead of conventional displacement/strain sensors. A DIC system is developed using an open-source computer program and the best DIC marker configuration was selected using test data. A drone platform was then built using off-the-shelf hardware, aiming to prove the mission feasibility, and to reduce the total costs with respect to other commercial or professional drones available in the market. The accuracy of the proposed drone-based displacement measurement tools was then evaluated by performing several experimental tests on a scaled truss bridge model. A summary of each task is presented herein, and the detailed discussion for each task is presented in the following chapters of the report.

ES.3 Literature Review

The literature was reviewed to collect information on bridge inspection and field testing using new technologies such as drones and DIC. During bridge field testing, girder vertical displacements (using Linear Variable Differential Transformers, LVDTs) and/or girder longitudinal strains (using surface-mount strain transducers) are measured. Such measurements allow calculation of girder distribution factors then adjustment of analytical load rating values. Note that any field measurement should be done for all girders of a bridge at a section (usually at the midspan for the moment distribution calculation, and sometimes at the girder ends for the shear distribution estimation). Several bridges have been field tested in the past (**Fig. ES.1**). Measuring the girder displacement was common in early studies. However, strain measurements are more common nowadays since the strain transducers do not need a reference point. Furthermore, reusable strain gauges specific to bridge field testing (e.g., BDI sensors shown in **Fig. ES.1b**) are currently available on the market. **Table ES.1** presents a summary of past bridge field testing including the maximum responses measured in these tests.

(a) Bridge Underneath

(b) Installation of Strain Gauges with Extension

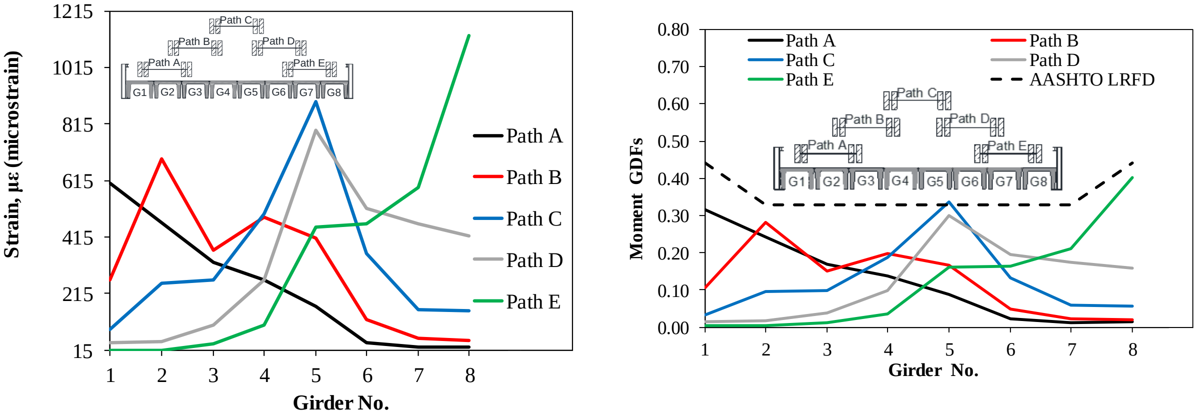

(c) Maximum Measured Flexural Tensile Strains

(d) Moment Girder Distribution Factors

Figure ES.1. Sample Results of a Bridge Field Testing by Rimal et al. (2019)

Table ES.1. Measured Bridge Responses in Past Field Testing

Reference	**Span Length, ft (m)**	**Girder Type**	**Peak Measured Displ., in. (mm)**	**Peak Measured Strain, με**	**Peak Measured Accel., in/sec^2 (mm/sec^2)**
Issa et al. (1993)	45.5 (13.9)	AASHTO type II	N/A	250	N/A
Issa et al. (1993)	66 (20.12)	AASHTO type III	0.385 (9.98)	195	40 (1016)
Issa et al. (1993)	121 (36.89)	AASHTO type IV	0.755 (19.35)	263	N/A
Nowak et al. (1996)	21.5 (6.55)	Reinforced T-beams	0.132 (3.380)	N/A	N/A
Nowak et al. (1996)	48 (14.63)	Steel girders	0.188 (4.82)	N/A	N/A
Nowak et al. (1996)	48.5 (14.783)	Steel girders	N/A	N/A	N/A
Nowak et al. (1996)	38.5 (11.73)	Steel girders	0.094 (2.41)	N/A	N/A
Nowak et al. (1996)	25.5 (7.77)	Reinforced T-beams	0.040 (1.02)	N/A	N/A
Chajes et al. (2000)	35, 58, 35 (10.67, 17.68, 10.67)	Steel girders	N/A	135	N/A
Phares et al. (2005)	70 (21.34)	Deep welded girders	N/A	51 to 210	N/A
Schiff et al. (2006)	42.5 (12.95)	Steel girder	N/A	65	N/A
Suksawang et al. (2007)	78.7 (24)	I-girder	N/A	35	N/A
Suksawang et al. (2007)	52.5 (16)	I-girder	N/A	45	N/A
Suksawang et al. (2007)	18.9 (15.75)	I-girder	N/A	55	N/A
Suksawang et al. (2007)	34.4 (10.5)	I-girder	N/A	38	N/A
Suksawang et al. (2007)	147.6 (45)	I-girder	N/A	105	N/A
Islam et al. (2014)	84.5 (25.76)	Prestressed box beam	N/A	N/A	N/A
Islam et al. (2014)	85 (25.91)	Prestressed box beam	N/A	N/A	24 (610)
Sanayei et al. (2015)	38.6, 77.1, 38.6 (11.76, 23.50, 11.76)	Steel girders	N/A	104.4	N/A
Torres (2016)	51 (15.54)	Double Tee	0.789 (20.23)	480	N/A
Rimal et al. (2019)	42 (12.8)	Prestressed Double-Tee	N/A	400	N/A
Rimal et al. (2019)	50 (15.24)	Prestressed Double-Tee	N/A	1150	N/A
Dong et al. (2020)	52 (15.85)	AASHTO Type II	0.037 (0.94)	N/A	N/A
		Maximum =	0.789 (20.23)	1150	40 (1016)

Frequent inspection and condition assessment of bridges are required to document their deteriorations and damages over time. The use of non-contact monitoring systems is gaining momentum in the US since they are easier to install and maintain compared with conventional instruments (e.g., LVDTs, strain gauges). Computer vision could be used as one of the non-contact structural response measurement methods. Vision-based displacement measurement methods usually require either physical (a printout patten attached to the surface of interest) or virtual speckles (or targets) to improve measurements in non-stationary imagery environments. To minimize the use of physical targets, feature points (or virtual markers) can be utilized. For example, Dong and Catbas (2019) used a feature matching strategy to replace handcrafted descriptors with learned descriptors (**Fig. ES.2a-d**). They combined Scale Invariant Feature Transform (SIFT) feature points with Visual Geometry Group (VGG) descriptors as a new strategy for vision-based displacement measurements. A two-span bridge model was selected for testing. A scaled-down model of a mid-size bridge was used and loaded with a toy truck with variable weights. Vision-based displacement measurement methods using four feature matching methods (SIFT, SURF, SIFT-VGG and SURF-VGG), and one conventional displacement sensor (a potentiometer, PM) were used to obtain the displacement time histories of a target point on the model bridge loaded with the moving toy truck. The results obtained from the proposed method (SIFT-VGG) were consistent with those obtained from the physical sensor (**Fig. ES.2e**). Furthermore, the other vision-based methods showed good accuracy in terms of displacement measurements. Subsequently, a field application was performed on a railway bridge to verify the feasibility of the proposed displacement measurement method. The camera was placed at approximately 33 m (108 ft) away from the target region on the bridge. **Figure ES.2f** shows the railway bridge test results. The measured displacements using the proposed method were affected by camera motions. They proposed a method to remove the camera motions from the structural displacements.

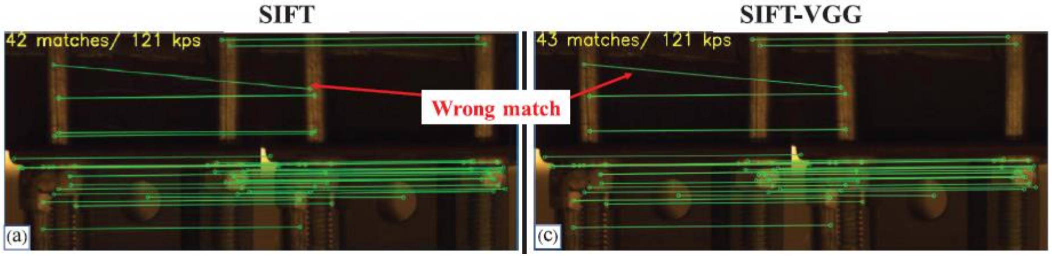

(a) SIFT Feature Matching

(c) SIFT-VGG Feature Matching

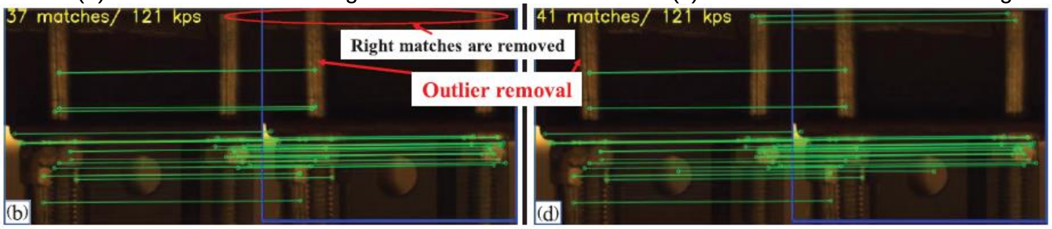

(b) SIFT Outlier Removal

(d) SIFT-VGG Outlier Removal

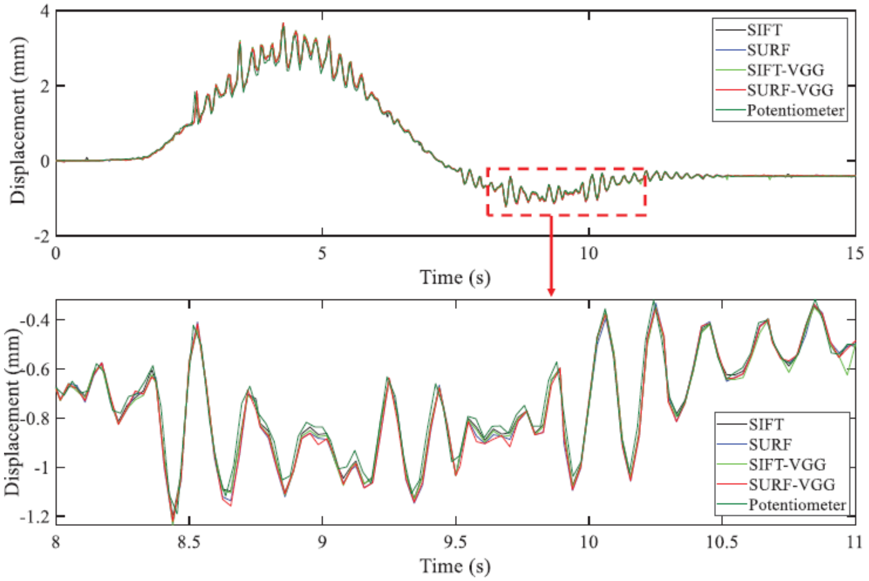

(e) Comparison of Displacement Time Histories for a Scaled Bridge

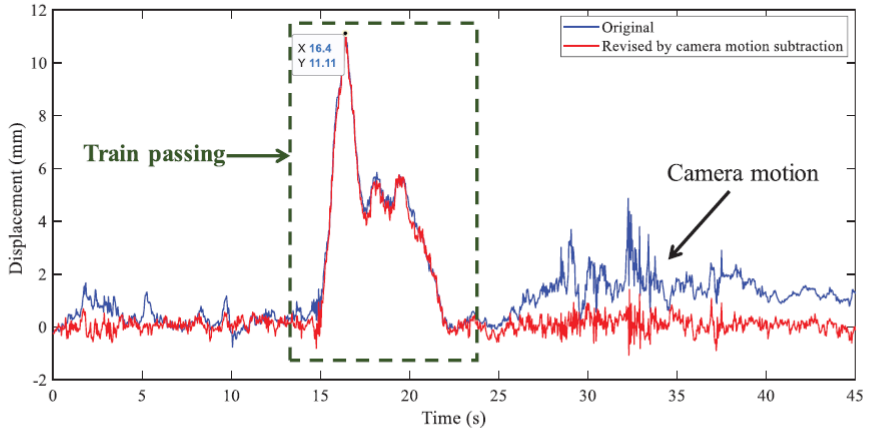

(f) Comparison of Displacement Time Histories for a Real Bridge

Figure ES.2. Sample of DIC Displacement Measurements for Bridges (Dong and Catbas, 2019)

The research team of the abovementioned study implemented the SIFT feature detector and VGG descriptor in a portable system consisting of a set of cameras, a set of synchronization modules, a computer, and a suite of software, to determine girder distribution factors for a highway bridge (Dong et al., 2020). One camera was used to record the traffic to determine which lane of the bridge was loaded and the other cameras were monitoring the deflection of the bridge girders (**Fig. ES.3**). To verify the proposed approach, two sets of experiments were conducted: (1) static loading, and (2) loading under normal traffic. Five potentiometers were installed at the midspan of each girder to measure the displacements. Three cameras were employed to measure the displacements at the same location. **Figure ES.3b** shows a sample displacement measurement by camera and LVDT, and **Fig. ES.3c** shows the girder distribution factors calculated by camera displacements, strains by strain gauges, and an analytical finite element model. Overall, a reasonable accuracy was reported when DIC was used compared with conventional measurements.

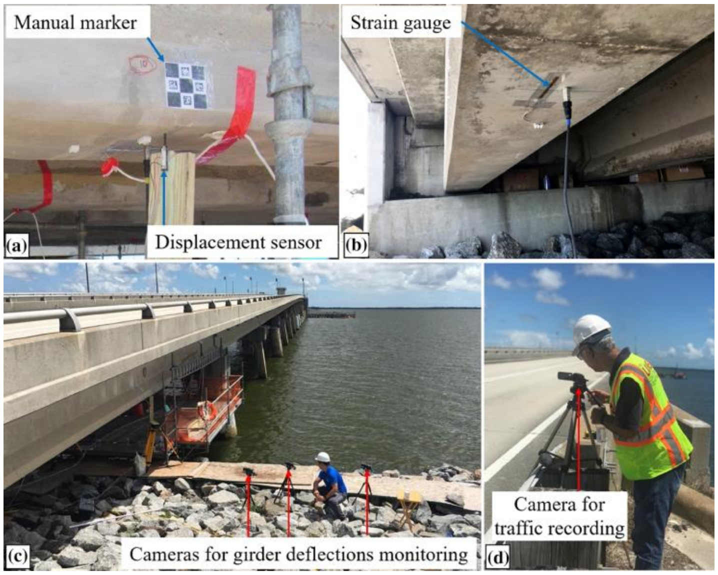

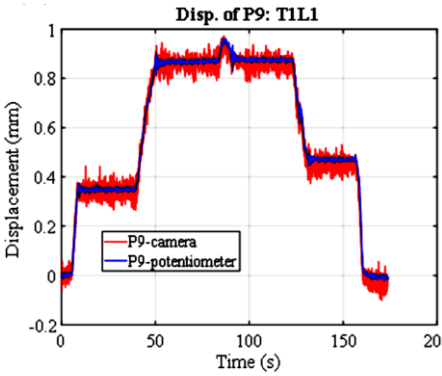

(b) Girder Displacements by DIC

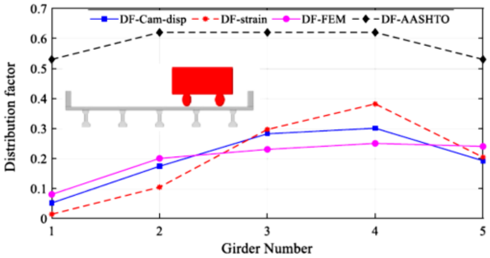

(a) Conventional and DIC Instruments

(c) Girder Distribution Factors

Figure ES.3. Bridge Field Testing and Measurement using DIC (Dong et al., 2020)

DIC systems are viable non-contact tools for the measurement of structural deformations, obtaining full-field strains, and simulating geometry profiles of structures. Moreover, UAVs have emerged as valuable tools for bridge inspection due to their low-cost operation and providing access to areas that are either difficult or dangerous for human inspectors. Yoon et al. (2018) presented a framework to achieve absolute displacements of a structure from a video taken by a UAV using a multi-step approach. First, a target-free method was implemented to extract relative structural displacements from the video. Next, the six degree-of-freedom camera motion was estimated by tracking the background feature points. Finally, the absolute structural displacement was estimated by combining relative structural displacements with camera motions (**Fig. ES.4**). In laboratory tests, vertical dynamic displacements of a steel truss bridge under a train traffic for 250 sec were reproduced using a servo-hydraulic motion simulator (**Fig. ES.5a**). The simulator can produce displacements with an accuracy of 0.1%. A DJI Phantom 3 equipped with a 4K resolution camera operating at 24 frames per second (fps) was selected for this experiment. A total of 6,000 frames were obtained during 250 sec. The camera recorded the video at 15 ft (4.57 m) from the motion simulator, which corresponded to the clearance required by the Federal Railroad Administration. **Figure ES.5b** shows the absolute displacement of the bridge determined using the proposed approach. The estimated absolute displacements matched well with the measured absolute displacements of the motion simulator. The root mean square error (RMSE) was 2.14 mm, corresponding to 1.2 pixels of resolution.

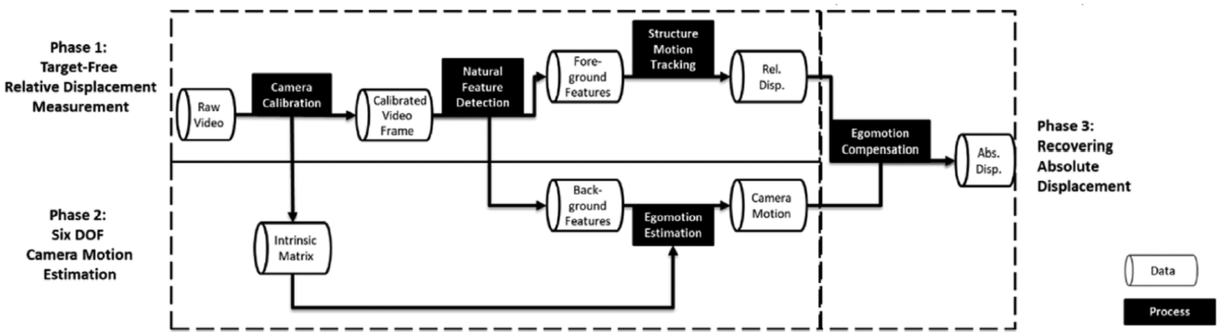

Figure ES.4. Structural Displacement Measurement Using UAV (Yoon et al., 2018)

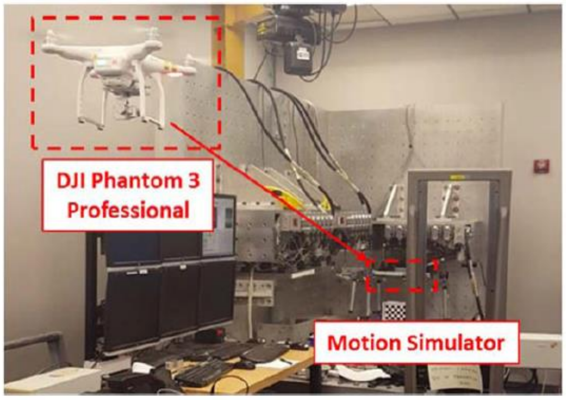

(a) Experiment Setup Using Motion Simulator

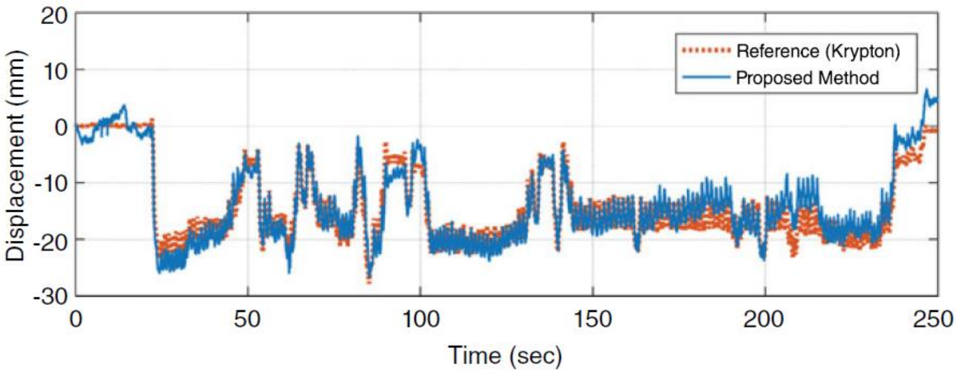

(b) Absolute Displacements

Figure ES.5. UAV Based Displacement Measurement Results (Yoon et al., 2018)

Hoskere et al. (2019) presented camera-enabled UAVs as a new sensing modality, and a novel vision-based data extraction pipeline to conduct modal surveys of full-scale civil infrastructure. The first step of the proposed approach was to obtain video of the vibrating structure through a divide-and-conquer strategy, where the UAV surveyed one portion of the structure at a time (**Fig. ES.6**). Once the video of the structure was obtained, the next part of the proposed approach included a vision-based pipeline to compute the modal properties from the recorded video (**Fig. ES.7**). To eliminate the drone movement from structural deformations, the study used signal filtrations assuming the drone hovering frequency to be predominantly low frequency (below 0.5 Hz) for UAVs with commercially available gimbals. The test results on a six-story shear-building model in a laboratory on a uniaxial shaking table showed that the proposed approach can estimate the structure natural frequencies with less than 0.5% error, and the modal assurance criterion (MAC) values all being greater than 0.996. An additional test was conducted on a full-scale pedestrian suspension bridge. The results showed that MAC values were all above 0.925, and the difference in the natural frequencies was less than 1.6% for three modes included in the analysis.

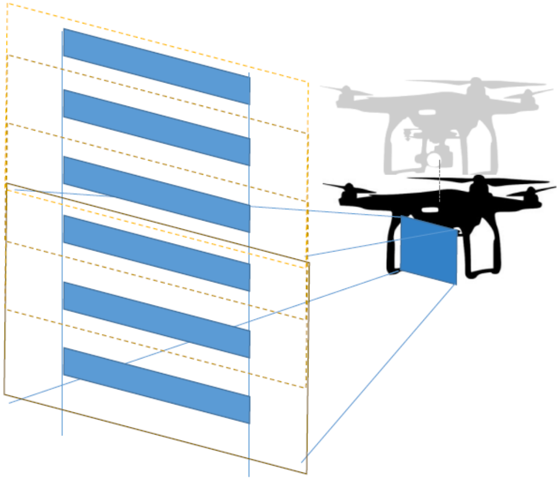

Figure ES.6. UAV Based Modal Property Measurement using Divide-and-Conquer Strategy (Hoskere et al., 2019)

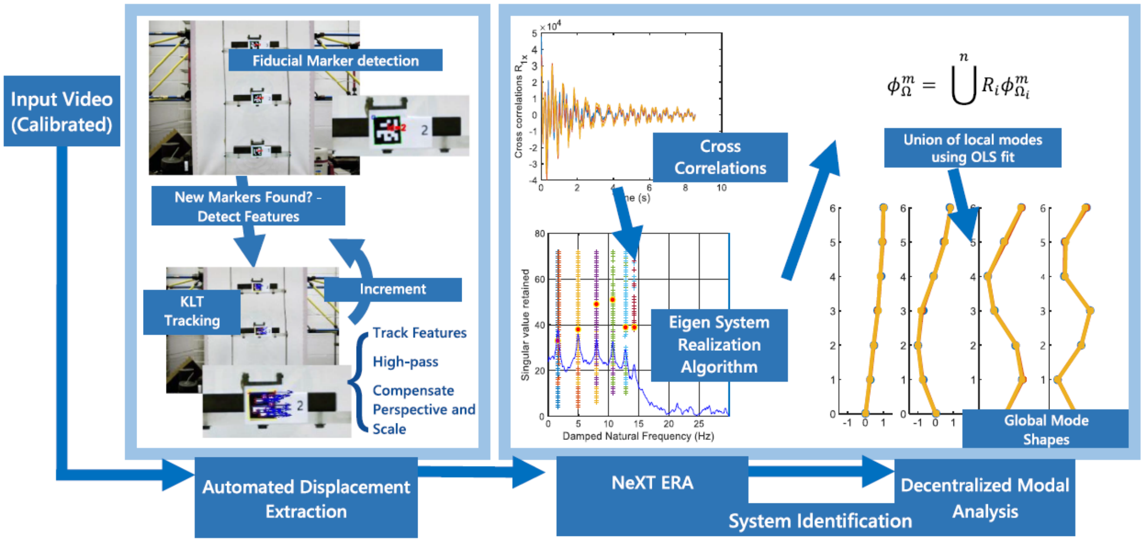

Figure ES.7. Pipeline for Automated Mode Shape Extraction Using Video Segments (Hoskere et al., 2019)

ES.4 Development of DIC-Drone-Based Displacement Measurement Tools

Three different mission strategies were proposed in this project to performed bridge field testing using drone-based displacement measurements. The select strategy (**Fig. ES.8**) involves a fleet of drones, each equipped with two DIC cameras. For each drone, one camera acquires the position of a target marker installed on the bridge, whereas the second camera looks at a reference marker placed on the bridge components with negligible vertical displacements during field testing such as bents and abutments. Virtual targets can also be utilized in this method. The difference between the DIC measurements from the reference and target makers is the girder displacement in which the drone motions are removed.

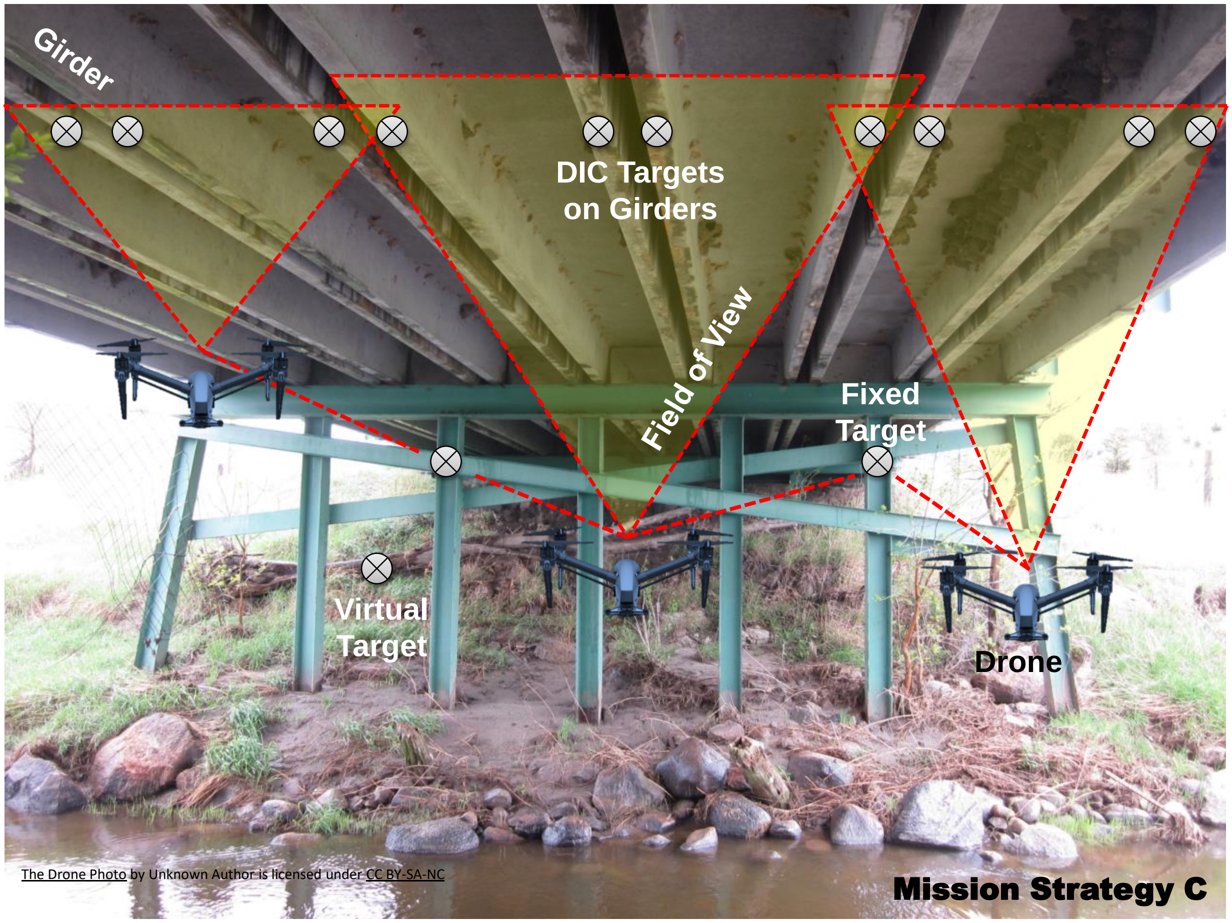

The Drone Photo by Unknown Author is licensed under CC BY-SA-NC

Figure ES.8. Proposed DIC Mission Strategy C Using Drone with Two Cameras

In this pilot study, physical ArUco markers were utilized. An ArUco marker is a synthetic square marker composed of a wide black border and an inner binary matrix that determines its identifier (ID). The black border facilitates its fast detection in the image, and the binary codification allows its identification and the application of error detection and correction techniques. Individual ArUco markers can be combined into a cluster of markers, as shown in **Fig. ES.9**. The dimension of the ArUco marker (or the cluster of markers) was selected based on the distance of the marker from the camera and the lens focal length.

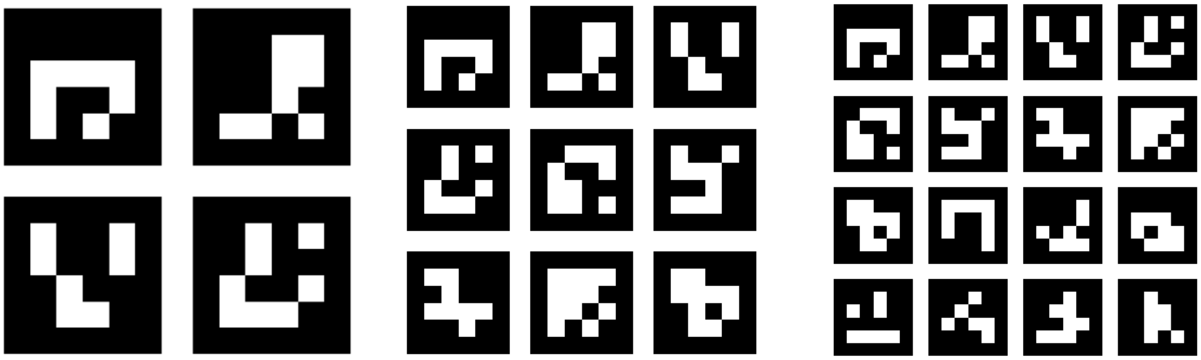

(a) Clusters of 4 Markers (b) Clusters of 9 Markers (c) Clusters of 16 Markers

Figure ES.9. Samples of ArUco Marker Clusters from 4x4 Dictionary

Given the camera parameters provided by the camera calibration and an image containing ArUco markers, the DIC marker-based displacement measurement technique returns a list of detected markers by using Python, as the select programming language, in combination with OpenCV, an open-source computer vision library, which implements real-time computer vision algorithms (OpenCV, 2022a). When a marker is detected, the camera pose with respect to the marker can be computed as a 3D transformation from the marker coordinate system to the camera coordinate system. A built-in OpenCV function is used for the camera pose estimation, knowing the four corners of the detected ArUco marker, its dimension, and the camera calibration parameters. The function returns the markers' pose estimation with respect to the camera individually. For each marker, rotation and translation vectors are returned. The returned transformation is the one that transforms points from each marker coordinate system to the camera coordinate system. The marker coordinate system is centered in the middle of the marker, with the z-axis perpendicular to the marker plane. Then, the rotation vector is converted to a rotation matrix. By knowing the rotation matrix, *R*, and the translation vector, *t*, displacement of the ArUco marker between two consecutive frames can be retrieved. For a single marker appearing in two frames, the displacement *d* can be computed as:

$$d = R_1^T(t_2 - t_1) \qquad \text{(Eq. ES.1)}$$

where, R_1^T is the transpose of the rotation matrix at frame 1, and t_1 and t_2 are respectively the translation vector at frames 1 and 2. For a cluster of markers, the rotation matrix of the cluster was calculated by extracting the four corners of the cluster of markers. Subsequently, the cluster rotation matrix, R_c, was retrieved using the camera calibration parameters, the cluster dimensions, and the cluster's corners, all as the inputs of the OpenCV built-in function for the pose estimation. Using information of two frames, the displacement *d* was computed as:

$$d = R_{c1}^T(\bar{t}_2 - \bar{t}_1) \qquad \text{(Eq. ES.2)}$$

where, R_{c1}^T is the transpose of the cluster rotation matrix at frame 1, and $\bar{t}_1$ and $\bar{t}_2$ are the mean translation vectors of all the single markers in the cluster at frames 1 and 2.

When two clusters of markers, one as the reference marker and another as the target, are considered in a test, the displacement, d_{tr} of the target with respect to the reference can be computed as:

$$d_{tr} = R_{r_i}^T\left(b_{t_i} - b_{r_i}\right) \qquad \text{(Eq. ES.3)}$$

$$b_{r_i} = \left(\bar{t}_{r_i} - \bar{t}_{r_o}\right)$$

$$b_{t_i} = \left(\bar{t}_{t_i} - \bar{t}_{t_o}\right)$$

$$with\ i = 1, \dots, n_{frames}$$

where, $\bar{t}_{t_o}$and $\bar{t}_{r_o}$ are respectively the mean translation vectors of all the single markers in the target and reference cluster at the initial frame, $\bar{t}_{t_i}$ and $\bar{t}_{r_i}$ are the mean translation vectors of all the single markers in the target and reference clusters in the subsequent frames, and $R_{r_i}^T$ is the transpose of the rotation matrix of the reference cluster at the i^{th} frame.

An experimental study was conducted to determine the best camera option(s) for use in DIC-drone applications. The trade-off in selecting the camera system was based on the following criteria:

- Weight.
- Image sensors: complementary metal oxide semiconductor (CMOS) vs. charge-coupled device (CCD). CMOS should allow higher frame rate, it is cheaper, and its quality and capabilities are now similar to CCD. In addition, CMOS sensors have a smaller size and lower power consumption than CCD sensors.
- Pixel size: large pixel results in a higher dynamic range and signal-to-noise ratio, but lower spatial resolution with respect to a small pixel size.
- High lens focal length means low FOV, and vice versa.
- Maximum lens focal length depends on the type of lens mount.
- Depending on the marker size and its distance from the camera, high lens focal length (e.g., ≥ 50 mm) or small camera pixel size (or both) may be required.
- A camera that supports different lenses and lens focal lengths might be necessary.
- A minimum frame rate of 30 per second.
- A camera characterized by both high resolution and high frame rate is more expensive than a camera that has only one of the two features.

Four cameras were included in the evaluation study: an Intel RealSense D435i, a Canon EOS 7D, a Blackfly S USB3, and a GoPro HERO4. **Table ES.2** presents the specifications of these cameras.

Table ES.2. Cameras Used in Evaluation Study

Camera	Shooting Mode	Resolution	Pixel Size (μm)	Frame per Second (FPS)	Focal Length (mm)
INTEL d435i	Photo	1920 × 1080	3.0 × 3.0	N.A.	26
CANON EOS 7D	Photo	5184 × 3456	4.305 × 4.305	N.A.	250
Blackfly S USB 3	Video	2448 × 2048	3.45 × 3.45	24	16
GoPro HERO4	Narrow Video	1920 × 1080	9.4 × 9.4	30	27

These cameras were evaluated using two test methods. The first test was done by taking multiple pictures of a steady marker and extracting the position of the marker from the images, to assess the noise and uncertainty level of a still image. These tests showed that the use of a cluster of markers reduced the mean error. The second series of the camera evaluation tests were focused on the measurement of the vertical (y direction) displacement of the marker in which the marker was manually displaced by 10.3666 mm (**Fig. ES.10**). At the beginning of each test, the marker was placed on the top of a spacer with a depth of 10.3666 mm, which was measured using a caliper. Subsequently, the spacer was removed. Pictures were taken with different cameras before and after removing the spacer. Note that the camera was fixed.

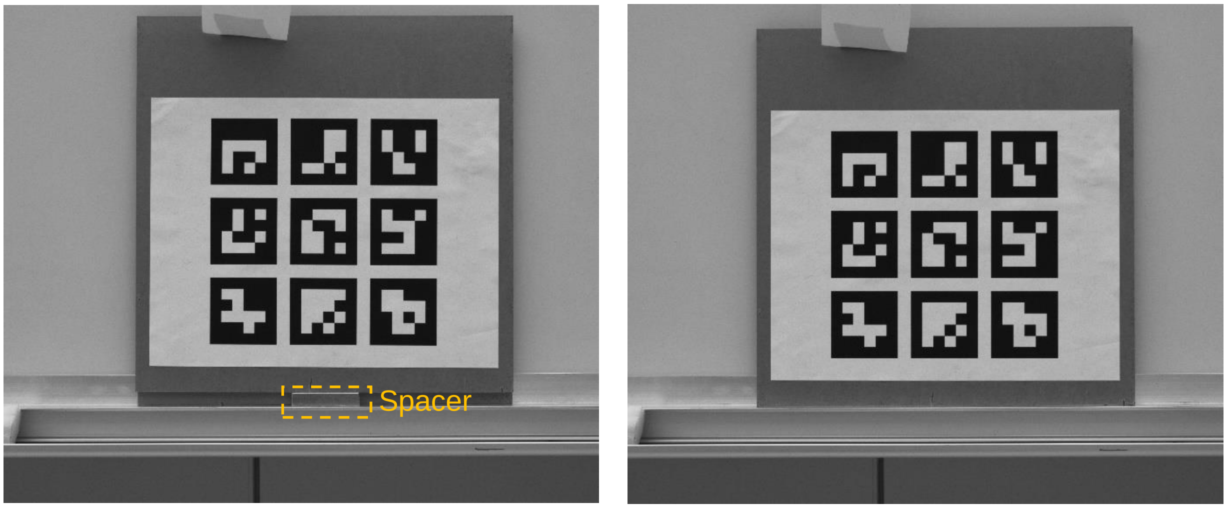

(a) Marker on Spacer (b) Marker when Spacer was Removed

Figure ES.10. Camera Evaluation by Displacing Markers to a Known Position

Blackfly Camera, cluster of 9 markers at ~ 1000 mm distance and ~ 0° orientation

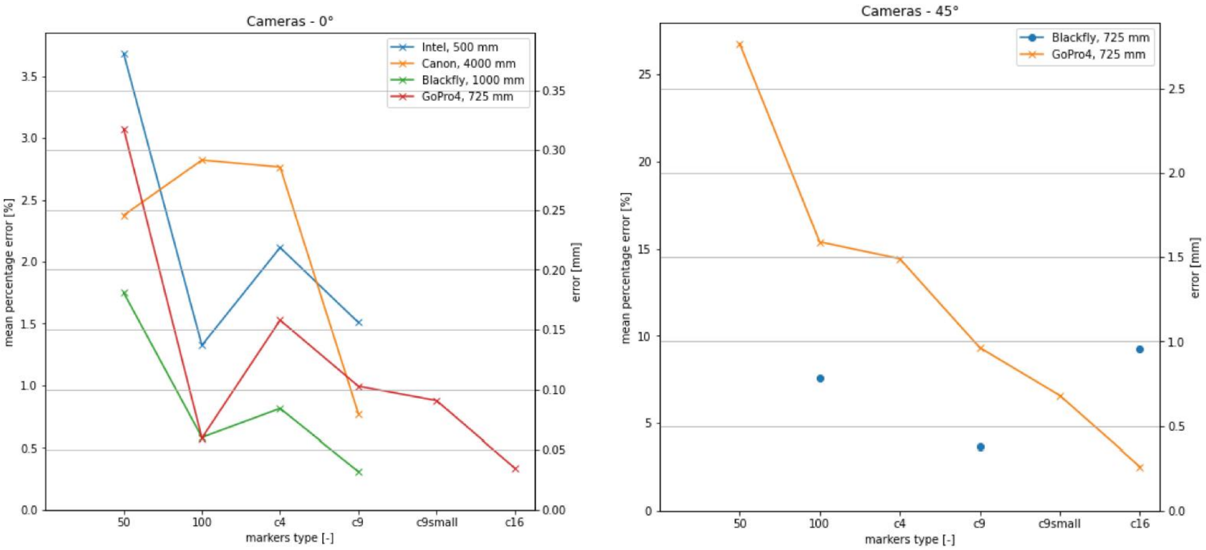

(a) Camera Sensor Parallel to Marker (b) Camera Sensor Oriented at 45° of Marker

Figure ES.11. Camera Performance in Known Displaced Marker Tests

Using these two pictures or frames, the displacement in the *y*-direction by the DIC methods described in the previous section was estimated. This process was repeated six times, and the mean percentage error and the maximum percentage error of the measurement were computed. **Fig. ES.11** shows the test results for all cameras in terms of the mean percentage error and its equivalent physical value. It can be seen that the least mean percentage error was usually achieved when a cluster of markers was used, specifically the cluster of nine markers. Since the cluster of 16 markers had the same overall size as the cluster of nine markers, their constitutive markers were smaller in the 16-marker case. This reduced the software's accuracy in detecting and extracting markers' positions at the pixel level. In addition, the use of a cluster of markers increased the accuracy of the displacement measurements by merging results from multiple markers at the same time. Another finding was that an increase in the orientation between camera and marker always adversely affected the displacement measurements. Parallel measurements (i.e., 0°) are recommended. Based on these evaluation tests, Blackfly S camera was selected for further investigations due to its high accuracy and cost effectiveness.

Finally, a UAV system was built which consisted of a Tarot FY690S Full 6-axis Carbon Fiber frame 3K Folding hexacopter, six Tarot high power BLDC motors with carbon propellers, a Cube Orange Standard Set, with H7 Processor and ADS-B Carrier Board, Flycolor 40A ESC, and daier ESC power distribution board, a Pixhawk 2.1 Power Module, a Cubepilot Here 3, and a high precision Global navigation satellite system (GNSS). In addition, a Herelink HD Video Transmission System was used as an integrated remote controller using wireless digital transmission system. It allows remote control, HD video, and telemetry data to be transmitted up to 12.4 miles (20 km) between the ground station and air unit. The hexacopter had a final total weight of 4.1 kg, allowing a max payload capacity of about 2 kg, and a maximum flight time of about 18 min, with a 5000 mAh battery (**Fig. ES.12**). The payload is mainly composed of two cameras, a mini-PC, and two electric batteries. A carbon fiber plate placed at the bottom of the drone was used to accommodate the payload. This configuration allowed having an adequate distribution of weights, balance, and flight stability. The on-board computer was a MeLE Fanless Mini PC Quieter3Q Intel Celeron N5105 with 8GB of RAM and 500 GB of SSD storage, whereas the battery was a HRB 4S 14.8v 5000mAh 50C Lipo Battery. The camera system was composed of two Blackfly S USB3 cameras (Model: BFS-U3-51S5M-C: 5.0 MP, 75 FPS, Sony IMX250, Mono), mounting lenses with different focal lengths depending on the test scenario. Either a 16-mm (0.63-in.) focal length Kowa LM16JC5M2 or a 50-mm (1.97-in.) focal length Edmund Optics lens was used. Two USB 3.0 cables were used to power the cameras. Two Hirose HR10 (6 Pin) GPIO cables and a simple circuit were utilized to synchronize the frames. Lastly, an HDMI cable was used to stream the camera feeds to the Herelink HD Video Transmission System for a real-time First Person View (FPV). This was necessary to check if the markers were inside the camera FOV. The total weight of this payload, with the 50-mm lens, was 1.58 kg.

Figure ES.12. UAV Built with Commercial-off-the-shelf Hardware

ES.5 Verification of Drone-Based Displacement Measurement Tools

A bridge model was selected in which it could be loaded to 10 mm (0.4 in.) without the use of hydraulic actuators or heavy equipment. The bridge model was a truss made of three parts. Each part was 1.5 m (59 in.) in length and had a square cross section with a side dimension of 203 mm (8 in.). The total length of the truss bridge was 4.5 m (177 in.). As shown in **Fig. ES.13**, the truss bridge was placed on the top of a series of concrete blocks, to reach a height that was easy to load the bridge without any equipment and to fly drones. At the bridge midspan, a piece of plywood was attached on the bridge using a bolt to secure the target DIC marker. Target in this study is the displacement of interest. Another marker is added in some tests to serve as the reference marker. A pedestal is positioned underneath the bridge at its midspan to install displacement sensors and the reference DIC marker.

Figure ES.13. Photograph of Truss Bridge Model and Test Setup

Conventional sensors were used in all experiments to measure vertical displacements of the bridge test model under different loading. Specifically, Series TR / TRS LVDTs by Novotechnik were used. The LVDTs were connected to a Vishay data acquisition system (DAQ), and the data was recorded using StrainSmart software. The 128-channel DAQ can record up to 2000 measurements per second. In the present study, a rate of 10 or 100 data per second was used. The 10-Hz sampling rate was sufficient for static tests, but 100 Hz was used in dynamic tests.

As discussed earlier, Blackfly S USB3 was selected for the DIC measurement in the bridge testing. Furthermore, a Raspberry Pi HQ camera with a 16-mm (0.63-in.) telephoto lens was also utilized as a possible low-cost alternative. Different configurations or combinations of cameras were used over the course of the experimental study, which were:

- Tests with a single camera in which either the Blackfly or the Pi camera was used.
- Tests with two cameras but without synchronization in which a combination of the Blackfly and the Pi cameras were used. In some cases, two Blackfly cameras were used.
- Tests with two synchronized cameras in which both cameras were Blackfly.

Furthermore, different testing methods were considered:

- Static testing: performed by slowly adding weights on the top of the bridge at its midspan.
- Dynamic testing: performed by either suddenly releasing a heavy bucket, which was attached to the bridge, or manually pulling the bridge down.
- Bridge testing with moving cameras: since it was desired to mimic the drone movements in a controlled setup and to further fine tune the DIC measurements, two techniques were implemented. In the first method, the camera system was secured on the top of a moving cart, which was then manually displaced 50 to 100 mm (2 to 4 in.) back and forth. In the second method, we built an oscillating platform on the top of which the camera system was secured to simulate a more realistic drone movement. In this case, the camera system was moved by gently tapping the wood platform.
- Bridge testing with drone mount cameras: we built a drone system in-house, which can carry two cameras and a mini-PC for processing. Due to time limitations, we were not able to successfully use this drone inside the laboratory due to weak GPS signals. The GPS mounted on the drone allows the drone to enter a stable controlled flight and reduce hovering oscillations. This is especially important when a drone is watching a DIC marker. For these issues, the proposed DIC system was mounted on a different drone, a DJI MATRICE 210 V2 (**Fig. ES.14**). This drone has a maximum flight time of 38 min, a maximum payload of 2.34 kg (5.15 lbs.), a wind resistance of 12 m/s (26.8 mph), and can operate in -20 °C to 45 °C (-4 °F to 113 °F). After a few test flights, we found that this DJI drone can fly both outdoors and indoors. Subsequently, the DIC system was mounted to this drone then a few tests were performed indoors to validate the DIC measurement.

Figure ES.14. DJI Drone with DIC Payload and Field of View of Cameras

More than 70 tests were conducted. In the early tests, the feasibility of retrieving the vertical displacement of the truss bridge model was explored by extracting data from only one marker attached to the bridge (referred to as the target marker) using a single fixed (or ground) camera looking at the bridge. Based on the findings of these experiments and since the ultimate goal of the project was to mount the camera system on a drone, a reference marker attached to a stationary point was included. This allowed the measurement of the vertical displacement of the bridge with respect to the reference marker using only one camera, and consequently to counteract the motion of the drone that otherwise would be unknown. Then, since the marker/image fill factor influenced the results, one camera was not sufficient to include both target and reference markers in its FOV. Therefore, two cameras were utilized to improve the measurements in a more realistic manner. In the last rounds of testing, two cameras were mounted on the drone.

Figure ES.15 shows the measured vertical displacement of the bridge in a static testing using one Raspberry Pi HQ camera seeing both reference and target markers. The plot shows the displacement of each cluster of ArUco markers, and the combination of the two, which is referred to as "total displacement". It can be seen that the total displacements (shown in green) match well with those of LVDTs with less than 1% error at the peak load. Note that 1% error at the peak load in this test was equal to 0.09 mm (0.0035 in.) displacement. Further, the displacements toward the end of the testing were not zero, which might be due to a slight movement of the bridge during testing, or a slight slip of LVDTs. Overall, the vertical displacements of the bridge by both DIC and LVDTs were the same.

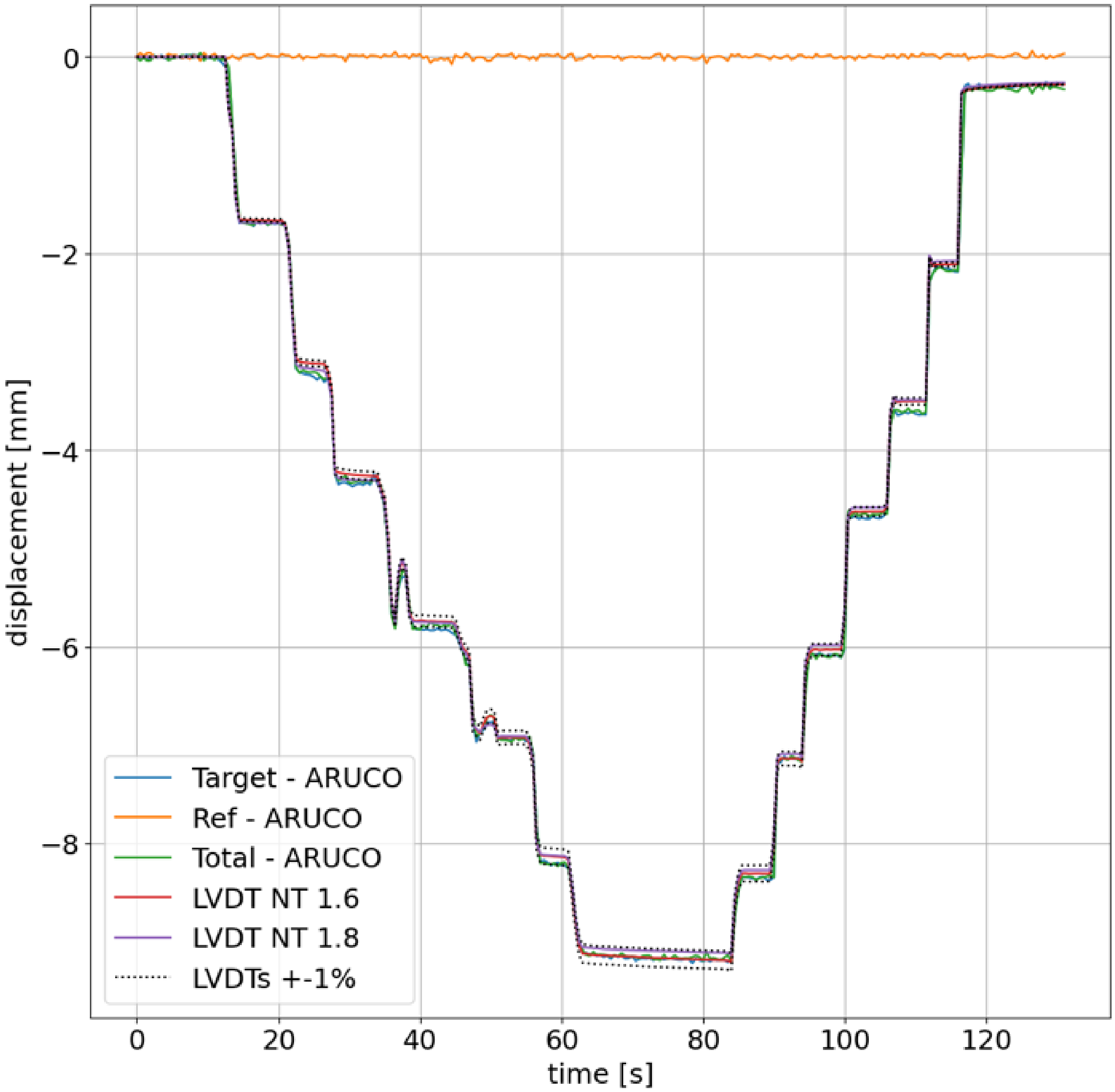

Figure ES.15. Static Test Results with Ground Raspberry Pi HQ Camera with Two Targets

1% error at peak load is equal to 0.09 mm (0.0035 in.)

Figure ES.16 shows the result of another static test but using the Blackfly camera on the moving cart. Similar to the previous test, the figure shows the displacement of each individual ArUco marker (the target and reference) and the total displacement. During this static test, the cart was displaced twice at approximately 45 and 90 seconds. Despite the cart-tripod-camera system vibration, the total displacements (marked green) matched well those of LVDTs with less than 2% error at the peak load. This error was equal to 0.18 mm (0.007 in.) displacement.

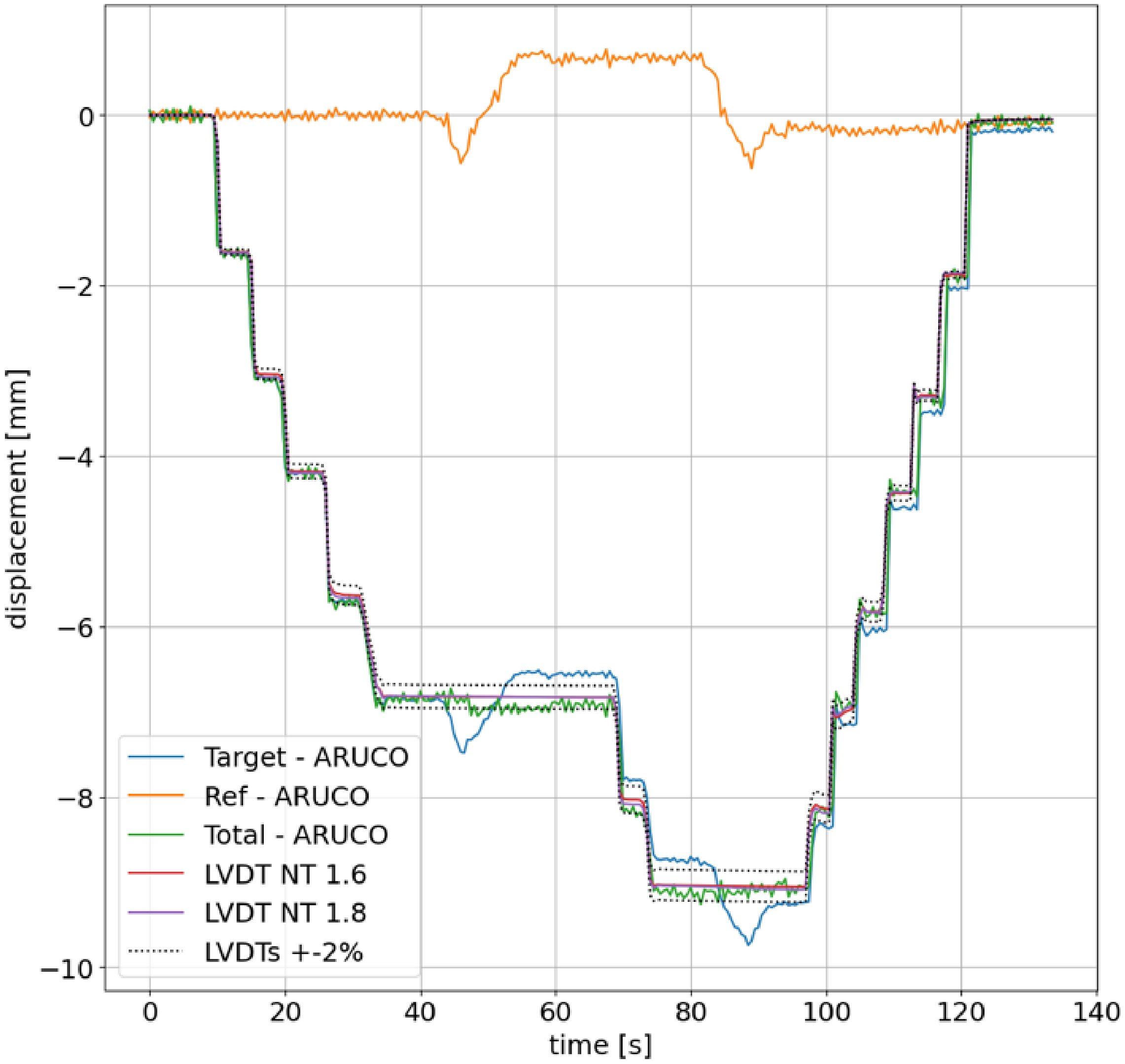

Figure ES.16. Static Test Results with Blackfly Camera on Moving Cart

2% error at the peak load was equal to 0.18 mm (0.007 in.)

Overall, results of experiments shown in **Fig. ES.15** and **ES.16** confirm that the proposed DIC method using a single camera and two markers is viable for static testing as it can measure the bridge displacements with high accuracy. The method can successfully remove camera motions caused by a moving platform from structural displacements.

Figure ES.17 shows the result of another static test with the 117.5-mm (4.62-in.) target marker at 1.2 m (3.93 ft) from the Pi camera, and the 117.5-mm (4.62-in.) reference marker at 1.5 m (4.92 ft) from the Blackfly. Nevertheless, the markers were in the opposite direction. The figure includes the displacement of each individual ArUco marker (the target and reference) and the total displacement, which is the bridge displacement by DIC. It is evident that the total displacements (marked green) were very close to those measured by LVDTs (red) with less than 1% error at the peak load. Note 1% error in this test was equivalent to 0.082 mm (0.003 in.) displacement.

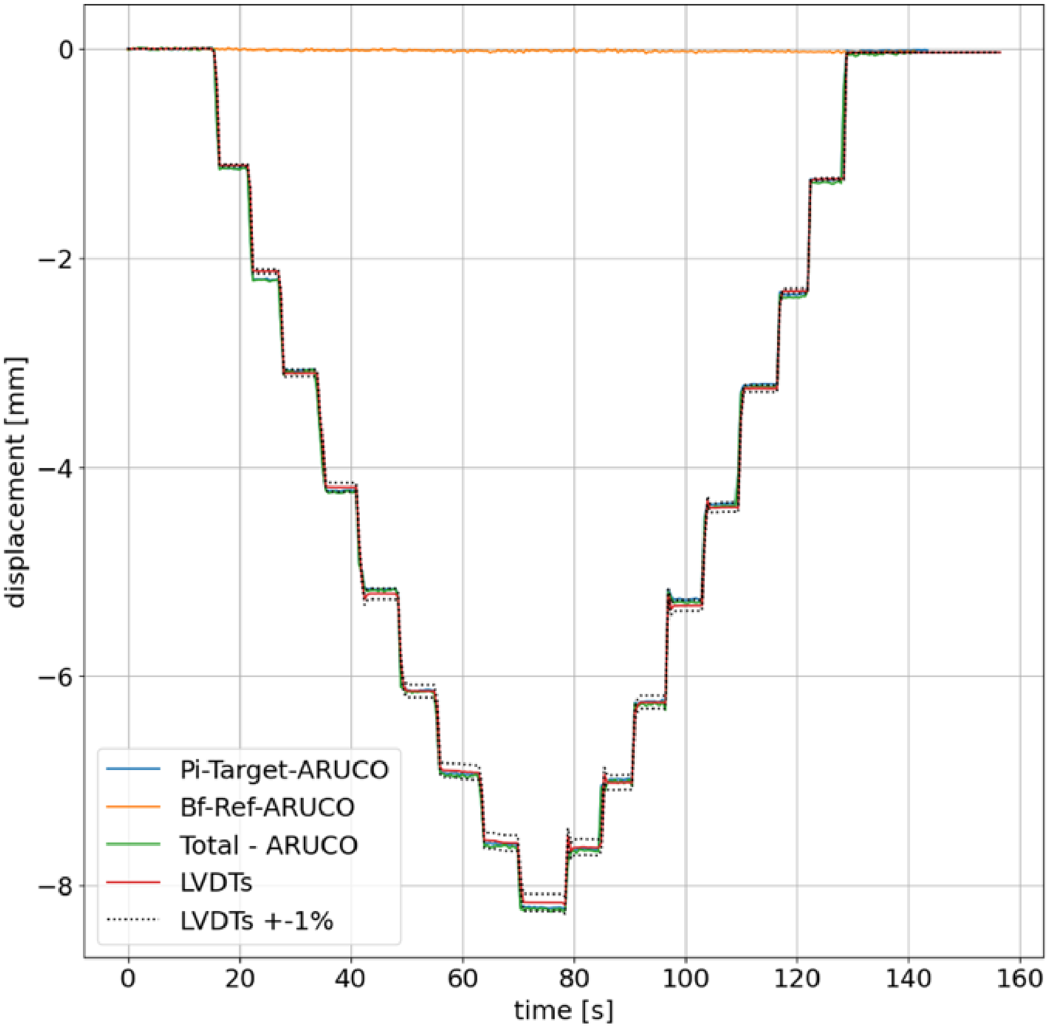

Figure ES.17. Static Test Results with Two Unsynchronized Cameras and Two Opposite Markers

1% error at the peak load was equal to 0.082 mm (0.003 in.)

Similar static tests were performed but using larger reference markers placed at a longer distance. The results of these static tests performed with the 406.5 mm (16 in.) or 1064.5 mm (41.9 in.) reference markers at 6 m (19.70 ft) from the Blackfly and the Pi camera at 1.2 m (3.93 ft) or 1.5 m (4.92 ft) from the truss bridge showed that the bridge displacements measured by DIC were very close to those of LVDTs. Nevertheless, static tests with two cameras on an oscillating platform showed large displacement errors. Lack of camera synchronization in time and frame rates was found as the main source of this inferior performance compared with other static tests.

Fig. ES.18 shows the results of two static tests in which two synchronized cameras were on the oscillating platform. In one test, both cameras were looking at the markers in the same direction, and in another test the cameras were looking at markers in opposite directions. The distance between the camera system and the two small size ArUco markers (the reference and target) was approximately 1.2 m (3.93 ft.). During each test, the camera platform was tapped three times to oscillate, which can be easily distinguished in the response (**Fig. ES.18**). The DIC displacements in both tests were close to the LVDT displacements, mostly with less than 5% errors equivalent to 0.41 mm (0.016 in.) displacement. Note that the right-side images are the same as the left ones but just show the total displacements by DIC. There were several spikes in the signal during the camera motions, which might be due to blurred images and limitations of the proposed system. The spikes were minimal when the camera motion stopped. These tests proved that syncing two cameras in terms of timing and frame rates can significantly improve the DIC measurements by reducing the number and amplitude of spikes resulting in a better displacement measurement.

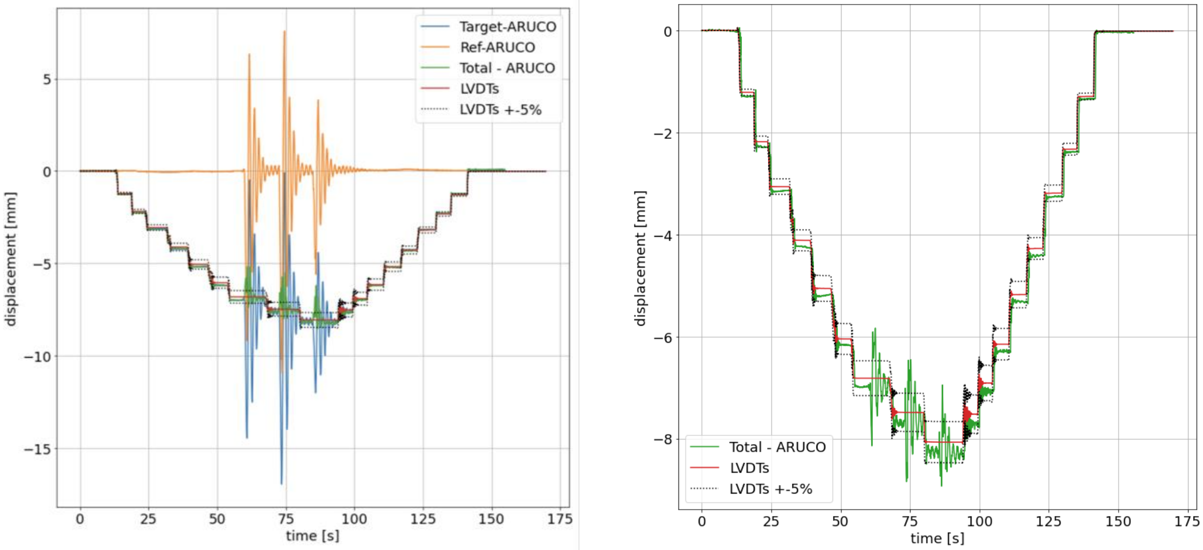

(a) Cameras facing the same direction, right showing DIC and LVDT response

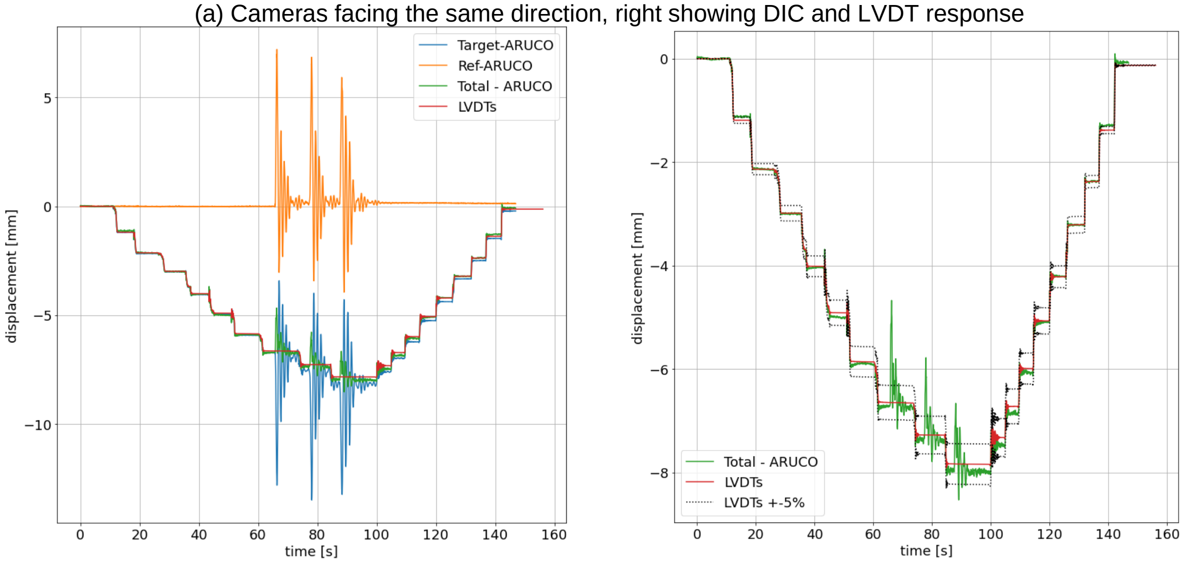

(b) Cameras facing opposite directions, right showing DIC and LVDT response

Figure ES.18. Static Test Results with Two Synchronized Oscillating Cameras

5% error at the peak load was equal to 0.41 mm (0.016 in.)

Figure ES.19 shows the results of two dynamic tests utilizing the two synchronized cameras on the oscillating platform. In other words, these tests were to evaluate the accuracy of the DIC method when the bridge was dynamically loaded, and the cameras were oscillating. Both cameras had 16-mm (0.63-in.) focal length lenses. In one test, both cameras were looking at the markers in the same direction, and in another test the cameras were looking at the markers in opposite directions. The distance between the camera system and the two small-size ArUco markers (the reference and target) was approximately 1.2 m (3.93 ft.). During each dynamic test, the camera platform was tapped four times to oscillate. The DIC total displacements followed well the LVDT response (**Fig. ES.19**) in these dynamic tests. The error at each peak of the four dynamic loads was 2% (0.08 mm or 0.003 in.), 14.1% (0.57 mm or 0.02 in.), 6% (0.29 mm or 0.01 in.), 15% (0.71 mm or 0.027 in.), and 7.3% (0.38 mm or 0.015 in.) in the test shown in **Fig. ES.19a.**, and 3.2% (0.14 mm or 0.005 in.), 6.4% (0.3 mm or 0.011 in.), 5.9% (0.27 mm or 0.01 in.), 2.47% (0.12 mm or 0.005 in.), 2.36% (0.125 mm or 0.005 in.) in the test shown in **Fig. ES.19b**. It is evident that the proposed DIC method was able to extract camera motions from the structural displacements.

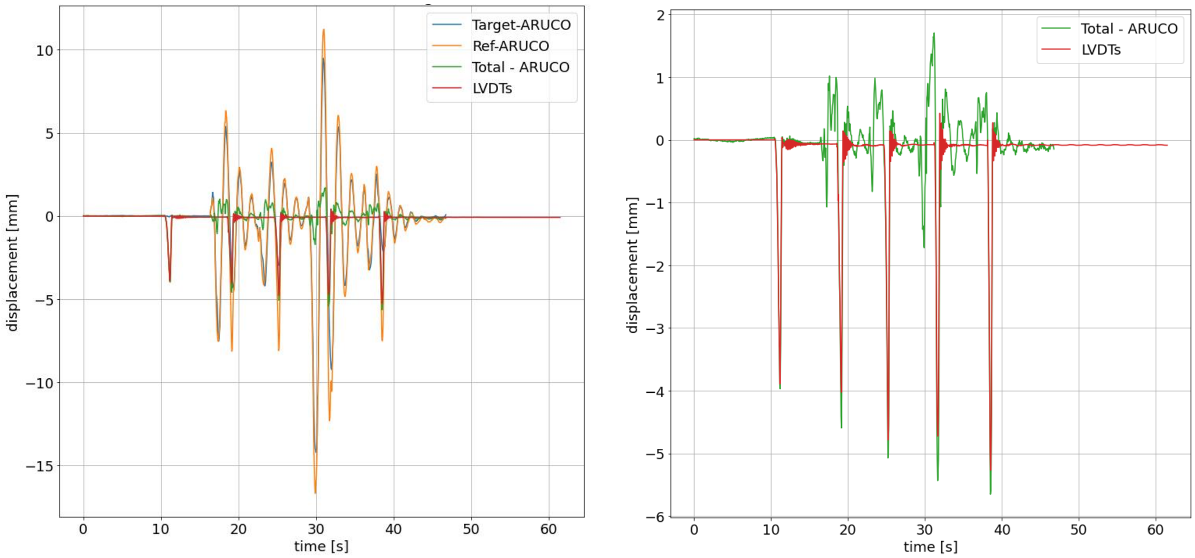

(a) Cameras facing the same direction, right showing DIC and LVDT response

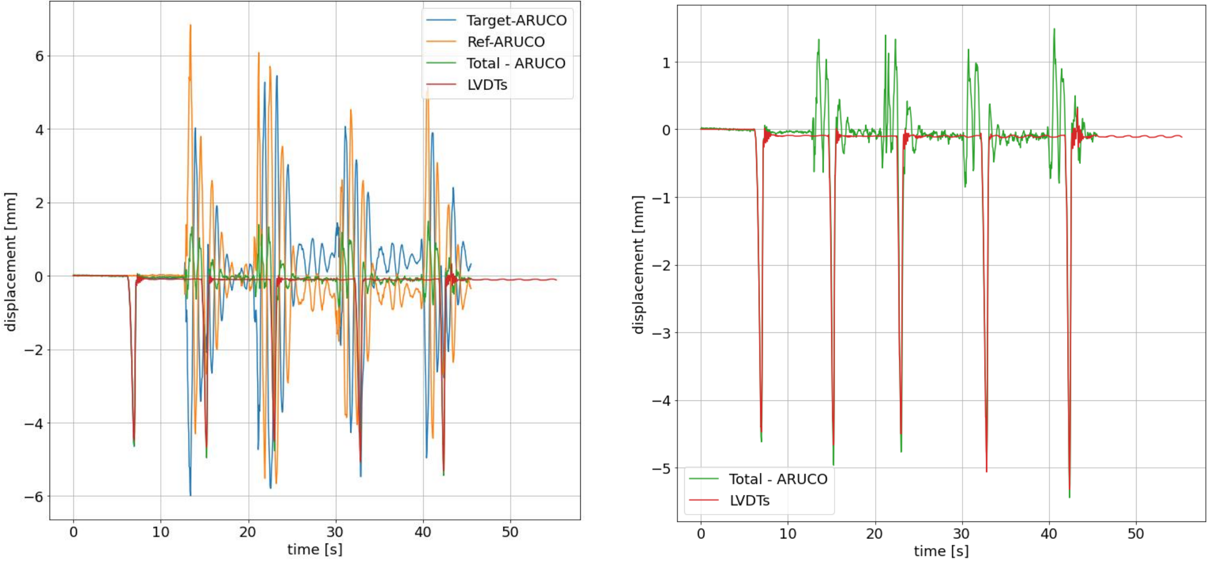

(b) Cameras facing opposite directions, right showing DIC and LVDT response

Figure ES.19. Dynamic Test Results with Two Synchronized Oscillating Cameras

The last series of testing in this project was to mount the camera system on a drone to evaluate the accuracy of the proposed DIC method. Based on the lessons learned from the previous experiments, two Blackfly cameras each equipped with a 16-mm (0.63-in.) focal length lens were synchronized and then attached to a mini-PC for data recording. During each test, the drone was flying at approximately 1.5 m (4.9 ft.) from the truss bridge and the video was recorded at 20 fps. The reference (bottom) and the target (top) ArUco markers were included. These markers had a side dimension of 117.5 mm (4.62 in.).

To investigate the drone measured displacements under fast loading, dynamic tests were performed. **Figure ES.20** shows the displacement of the bridge calculated using combined data from both drone cameras. The combined use of drone data (one for reference, one for target) showed some level of accuracy. However, several spikes exist.

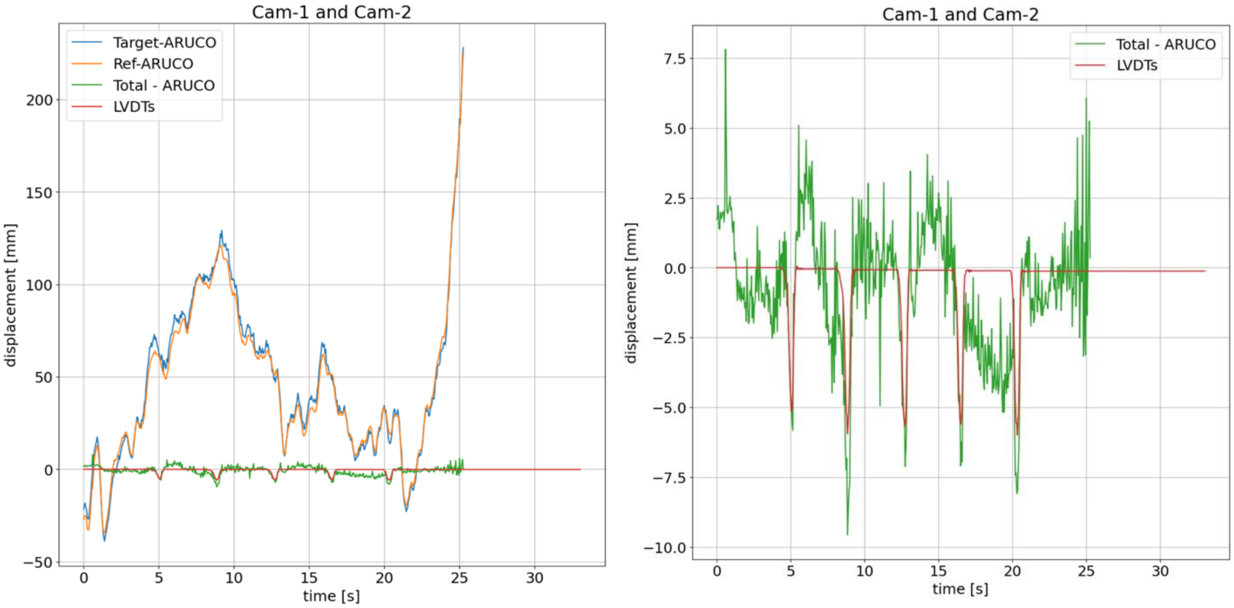

(a) Blackfly Cameras 1 & 2 Combined

(b) Same as (a) but showing DIC and LVDT response

Figure ES.20. Dynamic Test Results with Drone using Combination of Two Camera Data

To improve the results, the frequency content of the total displacement was calculated. As shown in **Fig. ES.21**, the signal was affected by noise with frequencies less than 2 Hz. To compensate for this effect, a high-pass filter (HPF) with a cut-off frequency equal to 0.22 Hz was applied. Subsequently, Savitzky-Golay filter was applied to the signal to smoothen the data. The combined use of HPF and Savitzky-Golay filters allowed removing high frequency noises and smoothing the signal without the loss of information related to the truss bridge vibration (**Fig. ES.22**). The displacement error between the proposed drone-based DIC method and LVDT at each peak of the five-cycle dynamic loading was 14.45% (0.74 mm or 0.03 in.), 16.17% (0.96 mm or 0.037 in.), 5.41% (0.306 mm or 0.012 in.), 1.53% (0.085 mm or 0.0033 in.), and 10.85% (0.65 mm or 0.025 in.).

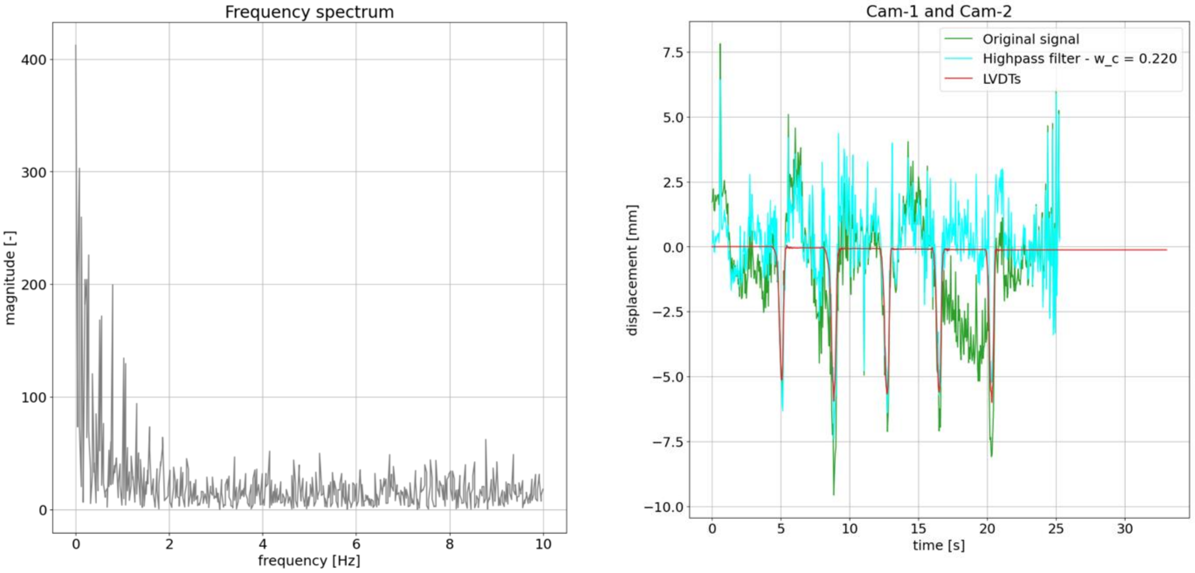

(a) Frequency spectrum (b) High-pass filter on total displacement

Figure ES.21. Signal Processing of Drone Measured Displacements

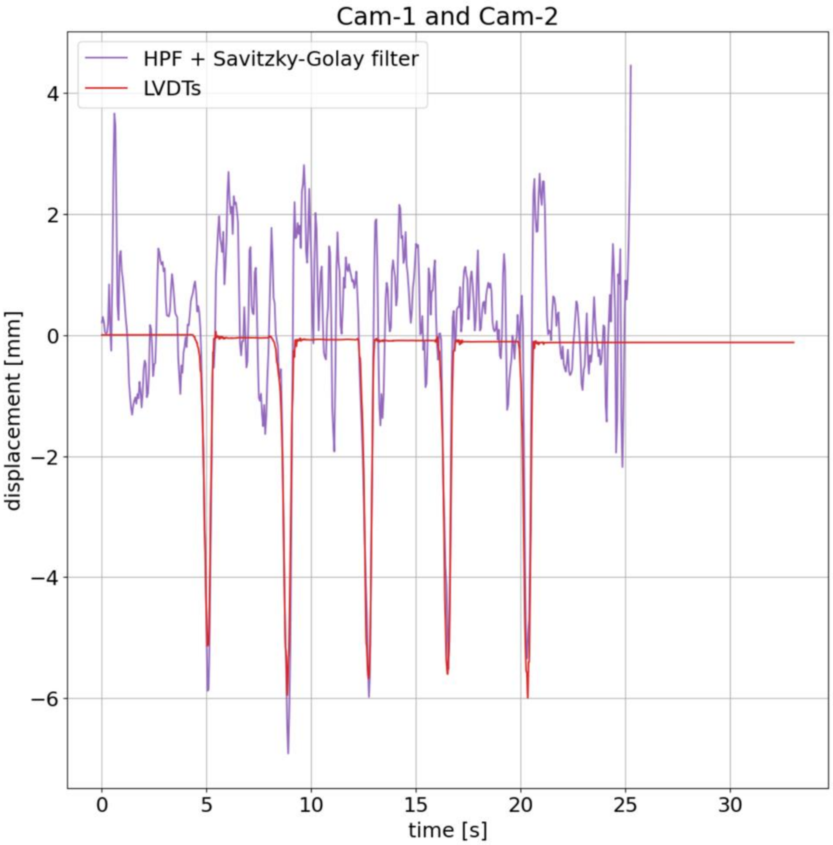

Figure ES.22. Drone-Based DIC Measured Displacements of Bridge after Applying High-Pass and Savitzky–Golay Filters

ES.6 Summary and Conclusions

The main goal of the present study was to develop a novel solution for bridge field testing in which drones equipped with DIC cameras are used to measure girder displacements, instead of conventional sensors, to be used in load rating. To achieve the project goal, several cost-effective camera configurations were studied to determine the best camera candidates for use in DIC-drone applications. Subsequently, different mission strategies were proposed in which a drone (or a fleet of drones) equipped with a set of cameras is deployed to perform bridge field testing using DIC techniques. A DIC system was developed using an open-source computer program and the best DIC marker configuration was selected using a preliminary experimental study. A drone platform was then built using off-the-shelf hardware, aiming to prove the mission feasibility, and to reduce the total costs with respect to other commercial or professional drones available in the market. The accuracy of the proposed drone-based displacement measurement tools was then evaluated by performing more than 70 tests on a truss bridge. Different camera configurations, test methods, and camera movement scenarios were included in the experimental study.

The following conclusions were drawn based on the experimental investigations:

- The proposed mission strategy in which one drone is equipped with two DIC cameras was selected for tool development as this method does not require a ground camera.

- The dimension of ArUco markers (or cluster of markers) should be selected based on the distance of the marker from the camera and the lens focal length. The lens focal length affects the camera field of view thus the marker/image fill factor (i.e., how big is the marker with respect to the full image).

- A DIC marker-based displacement measurement technique was developed in OpenCV, which can detect and estimate the pose of ArUco markers. In the proposed method, two DIC markers must be included, a target marker attached to the bridge, and a reference marker with zero displacements during bridge testing. The girder vertical displacements are retrieved by measuring the relative displacement of the target marker with respect to the reference marker.

- A cluster of nine ArUco markers was found as the best candidate for use in bridge applications since they resulted in the least displacement errors. Furthermore, the use of a cluster of markers increased the accuracy of the displacement measurements by merging results from multiple markers at the same time. Another finding was that an increase in the orientation between camera and marker always adversely affected the displacement measurements. Parallel measurements (i.e., 0°) are recommended. Among all low-cost cameras, the Blackfly S USB3 camera exhibited the highest accuracy in displacement measurements than Intel RealSense D435i, Canon EOS 7D, and GoPro HERO4. Both Blackfly S USB3 and Raspberry Pi HQ were included in the truss bridge model testing.

- Compared with conventional displacement sensors (e.g., LVDTs), Raspberry Pi HQ as the ground camera tracking the target marker on the truss bridge measured vertical displacements in the static tests with 1% error (equivalent to 0.08 mm or 0.003 in. displacement error) at 0° camera-to-marker inclination, 2% error (0.16 mm or 0.006 in. displacement error) at 22° inclination, 3% error (0.24 mm or 0.009 in. displacement error) at 45° inclination.

- Compared with LVDTs, Raspberry Pi HQ as the ground camera tracking two markers in static tests measured displacements with less than 1% error at the peak load, which was equal to 0.09 mm (0.0035 in.) displacement error.

- Raspberry Pi HQ placed on the top of a moving cart tracking two markers in static tests exhibited large spikes in the DIC measurements during the cart movement. When the cart-camera system was not moving, the DIC displacement followed those of LVDTs with less than 1% error.

- Blackfly S placed on the top of a moving cart tracking two markers in static tests produced displacements that matched well those of LVDTs with less than 2% error at the peak load, which was equivalent to 0.18 mm (0.007 in.) displacement error. The Blackfly S camera performed better than the Raspberry Pi HQ camera since no large spike in the displacement was seen when the Blackfly camera was used.

- Two unsynchronized ground cameras (Blackfly S and Raspberry Pi HQ) tracking the target and reference markers in the opposite directions in static tests resulted in less than 1% displacement error at the peak load. Nevertheless, the same two unsynchronized cameras mounted on an oscillating platform tracking the target and reference markers in static tests produced several spikes with large displacement errors. These tests showed that the lack of camera synchronization was the main source of large spikes and errors.

- Two synchronized ground Blackfly S cameras tracking the target and reference markers respectively at 117.5 mm (4.62 in.) and 1200 mm (47.27 in.) distance in static tests resulted in less than 3% displacement error at the peak load, which was equivalent to 0.24 mm (0.009 in.) displacement error.

- Two synchronized oscillating Blackfly S cameras tracking the target and reference markers both at 1200 mm (47.27 in.) distance in static tests resulted in less than 5% errors in displacements compared with those of LVDTs. Therefore, synchronization improves displacement measurements in a multi-camera DIC system.

- Two synchronized oscillating Blackfly S cameras tracking the target and reference markers both at 1200 mm (47.27 in.) distance in dynamic tests produced displacements with errors ranging from 2% (0.08 mm or 0.003 in.) to 15% (0.71 mm or 0.027 in.). When the reference marker was placed at further distance, the displacement error significantly increased.

- Two synchronized Blackfly S cameras mounted on a drone tracking the target and reference markers both at a 1500 mm (59.05 in.) distance in static tests measured displacements that had less than 5% errors (0.375 mm or 0.014 in. displacement error) compared with those of LVDTs. A low pass filter was used.

- Two synchronized Blackfly S cameras mounted on a drone tracking the target and reference markers both at 1500 mm (59.05 in.) distance in dynamic tests measured displacements with an error range of 1.53% (0.085 mm or 0.0033 in. displacement error) to 16.17% (0.96 mm or 0.037 in. displacement error). A high pass filter to remove signal noises and the Savitzky-Golay filter to smoothen the data were included.

Overall, the proposed DIC-drone-based displacement measurement strategy and computational tools were found feasible with submillimeter level accuracies advancing the state-of-the-art methodologies.

CHAPTER 1. INTRODUCTION

1.1 Introduction

More than 40% of the US in-service bridges are at least 50 years old, and the cost to repair the US bridges in their current condition is $125 billion. With the current budget allocation, it will take 50 years to repair the US bridges assuming no further deterioration. Furthermore, more than 60,000 bridges in the US are posted with limited passing loads. Overall, the national bridge inventory is graded “C” meaning that the nation’s bridges are in fair to good conditions, exhibit general signs of deterioration, and require attention (ASCE Report Card, 2021).

When a bridge is old or deteriorated, the evaluation of the load carrying capacity of the bridge, usually referred to as “load rating”, is necessary to ensure the safety of the traveling public and to prevent excessive bridge damage and, possibly, collapse. Load rating of bridges can be performed using either experimental (field testing) or analytical methods (AASHTO MBE, 2015).

Even though field testing offers actual insights into bridge behavior, it is not a common practice for bridge evaluation. Instead, the analytical load rating is often used. One main reason is the cost related to field operations. For bridge field testing, the cost is higher compared with an inspection due to the use of sensors, data acquisition system, test trucks, and data processing.

One effective way to reduce the inspection cost is to utilize new technologies such as drones or unmanned aerial vehicles (UAVs). During an inspection, drones increase accessibility and safety and may carry different types of sensors such as cameras, infrared cameras, stereo-vision cameras, and lidar cameras. By using these sensors on drones, one may generate 3D models of bridges, detect damages (cracking, spalling, etc.) through computer vision and artificial intelligence enabled software, or obtain new information about bridges such as displacement, stresses, and strains.

Digital image correlation (DIC) allows extracting full-field displacements and strains from images and videos. DIC has a wide range of applications in many disciplines including structural engineering. For a bridge field testing, DIC offers several advantages including low-cost displacement measurements (using commercial off-the-shelf cameras with a cost of less than a few hundred dollars), no need to use special inspection equipment, no need to close the traffic, and no need to use conventional sensors.

The present project is to develop a novel solution that combines the use of drones equipped with cameras and a computer vision system to perform drone-based measurements for bridge field testing.

1.2 Objectives and Scope

The main goal of this study, which is the first phase of a two-phase project, is to develop tools and frameworks to field test bridges using drones and DIC. To achieve the project goal, several camera configurations were studied to determine the best camera candidates for use in the DIC-drone applications. Subsequently, different mission strategies were proposed in which a drone (or a fleet of drones) equipped with a set of cameras is deployed to perform bridge field testing using DIC software, instead of conventional displacement/strain sensors. A DIC system was developed using an open-source computer program and the best DIC marker was selected using test data. A drone platform was then built using off-the-shelf hardware, aiming to prove the mission feasibility, and to reduce the total costs with respect to other commercial or professional drones available in the market. The accuracy of the proposed drone-based displacement measurement tools was then evaluated by performing more than 70 tests on a scaled truss bridge.

1.3 Expected Contributions

The main outcomes of this phase of the project are a DIC-drone-based displacement measurement framework and open-source computer programs that process the recorded videos for the estimation of structural displacements. The main products in this phase of the project are:

1. A camera system trade-off to select the best option for the mission.
2. A project-specific DIC software based on open-source programming languages.
3. A UAV built with commercial-off-the-shelf hardware.
4. A demonstration of the feasibility of the proposed DIC-drone-based displacement measurement framework and software tools.

1.4 Document Outline

As part of cover materials, an executive summary was presented in a chapter with the same name. Chapter 1 presents an introduction to the study and the scope of the work. A literature review on health monitoring, sensing, drones, DIC, and 3D reconstruction of bridge model using drone is conducted, and a summary is presented in Chapter 2. Chapter 3 discusses the development of the DIC drone-based displacement measuring tools, including hardware and software adopted. Chapter 4 describes the experimental program of the study including software, hardware, tests setup, and test results. Finally, the summary and conclusions of the study are presented in Chapter 5.

CHAPTER 2. LITERATURE REVIEW

2.1 Introduction

More than 40% of the US in-service bridges are at least 50 years old, and the cost to repair the US bridges in their current condition is $125 billion. With the current budget allocation, it will take 50 years to repair the US bridges assuming no further deterioration. Furthermore, more than 60,000 bridges in the US are posted with limited passing loads. Overall, the national bridge inventory is graded "C" meaning that the nation's bridges are in fair to good condition, exhibit general signs of deterioration, and require attention (ASCE Report Card, 2021).

When a bridge is old or deteriorated, the evaluation of the load carrying capacity of the bridge, usually referred to as "load rating", is necessary to ensure the safety of the traveling public and to prevent excessive bridge damage and, possibly, collapse. Load rating of bridges can be performed using either experimental (field testing) or analytical methods (AASHTO MBE, 2015).

Even though field testing offers actual insight into bridge behavior, it is not a common practice for bridge evaluation. Instead, the analytical load rating is often used. One main reason is the cost associated with field operations. For a bridge field testing, the cost is higher compared with an inspection due to the use of sensors, data acquisition system (DAQ), test trucks, and data processing.

One effective way to reduce the inspection cost is to utilize new technologies such as drones or unmanned aerial vehicles (UAVs). Ziehl et al. (2020) and Wells and Lovelace (2017) respectively estimated a cost saving of 55% and 66% when drones were used in inspections. Another study showed that the average inspection cost saving using drones for different bridge types was 40% (Wells and Lovelace, 2018). Furthermore, drones increase accessibility and safety during an inspection. Another important advantage of deploying drones is that if equipped with cameras, they can generate a 3D model of the bridges being inspected (e.g., Lattanzi and Miller, 2015; Khaloo et al., 2018; Chen et al., 2019; Popescu et al., 2019; Jalinoos et al., 2019; Liu et al., 2020). A 3D reconstructed bridge model provides a virtual reality platform to remotely inspect a bridge.

Digital image correlation (DIC), originally developed at the University of South Carolina in the early 1980s, is an optical method of extracting full-field displacements and strains from images and videos. DIC has a wide range of applications in many disciplines including structural engineering. For bridge field testing, DIC offers several advantages including low-cost displacement measurements (using commercial off-the-shelf cameras with a cost of less than a few hundred dollars), no need to use special inspection equipment, no need to close the traffic, and no need to use conventional sensors and DAQ.

This chapter presents a brief review of the literature on bridge inspection and field testing using new technologies such as drones and DIC.

2.2 Bridge Field Testing

During bridge field testing, girder vertical displacements (using Linear Variable Differential Transformers, LVDTs) and/or girder longitudinal strains (using surface-mount strain transducers) are measured. Such measurements allow the calculation of the girder distribution factors then adjustment of the analytical load rating values. Note that any field measurement should be done for all girders of a bridge at a section (usually at the midspan for the moment distribution calculation, and sometimes at the girder ends for the shear distribution estimation).

Several bridges have been field tested in the past (**Fig. 2.1**). Measuring the girder displacement was common in early studies. However, strain measurements are more common nowadays since the strain transducers do not need a reference point. Further, reusable strain gauges specific to bridge field testing (e.g., BDI sensors) are currently available in the market. **Table 2.1** presents a summary of the past bridge field testing including the maximum responses measured in these tests.

(a) Bridge Underneath

(b) Installation of Strain Gauges with Extension

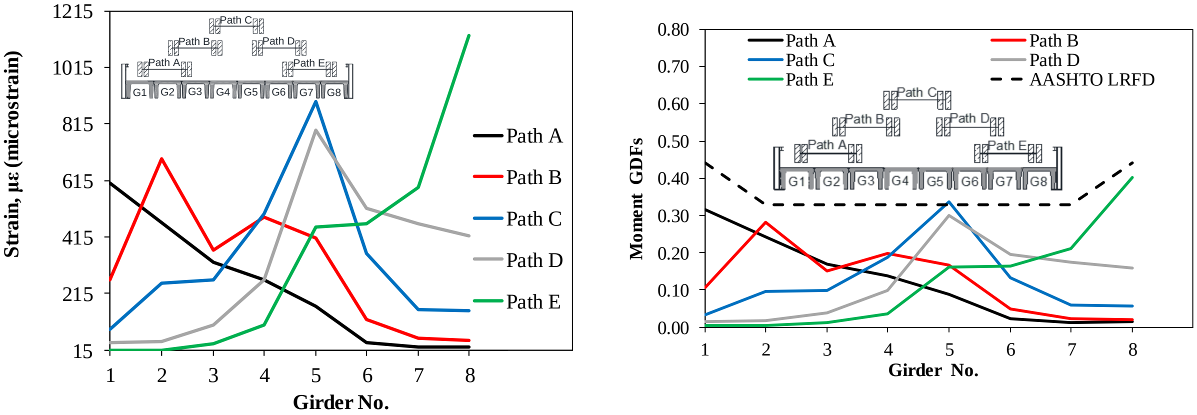

(c) Maximum Measured Flexural Tensile Strains

(d) Moment Girder Distribution Factors

Figure 2.1. Sample of Bridge Field Testing by Rimal et al. (2019)

Table 2.1. Measured Bridge Responses in Past Field Testing

Reference	Span Length, ft (m)	Girder Type	Peak Measured Displ., in. (mm)	Peak Measured Strain, με	Peak Measured Accel., in/sec^2 (mm/sec^2)
Issa et al. (1993)	45.5 (13.9)	AASHTO type II	N/A	250	N/A
Issa et al. (1993)	66 (20.12)	AASHTO type III	0.385 (9.98)	195	40 (1016)
Issa et al. (1993)	121 (36.89)	AASHTO type IV	0.755 (19.35)	263	N/A
Nowak et al. (1996)	21.5 (6.55)	Reinforced T-beams	0.132 (3.380)	N/A	N/A
Nowak et al. (1996)	48 (14.63)	Steel girders	0.188 (4.82)	N/A	N/A
Nowak et al. (1996)	48.5 (14.783)	Steel girders	N/A	N/A	N/A
Nowak et al. (1996)	38.5 (11.73)	Steel girders	0.094 (2.41)	N/A	N/A
Nowak et al. (1996)	25.5 (7.77)	Reinforced T-beams	0.040 (1.02)	N/A	N/A
Chajes et al. (2000)	35, 58, 35 (10.67, 17.68, 10.67)	Steel girders	N/A	135	N/A
Phares et al. (2005)	70 (21.34)	Deep welded girders	N/A	51 to 210	N/A
Schiff et al. (2006)	42.5 (12.95)	Steel girder	N/A	65	N/A
Suksawang et al. (2007)	78.7 (24)	I-girder	N/A	35	N/A
Suksawang et al. (2007)	52.5 (16)	I-girder	N/A	45	N/A
Suksawang et al. (2007)	18.9 (15.75)	I-girder	N/A	55	N/A
Suksawang et al. (2007)	34.4 (10.5)	I-girder	N/A	38	N/A
Suksawang et al. (2007)	147.6 (45)	I-girder	N/A	105	N/A
Islam et al. (2014)	84.5 (25.76)	Prestressed box beam	N/A	N/A	N/A
Islam et al. (2014)	85 (25.91)	Prestressed box beam	N/A	N/A	24 (610)
Sanayei et al. (2015)	38.6, 77.1, 38.6 (11.76, 23.50, 11.76)	Steel girders	N/A	104.4	N/A
Torres (2016)	51 (15.54)	Double Tee	0.789 (20.23)	480	N/A
Rimal et al. (2019)	42 (12.8)	Prestressed Double-Tee	N/A	400	N/A
Rimal et al. (2019)	50 (15.24)	Prestressed Double-Tee	N/A	1150	N/A
Dong et al. (2020)	52 (15.85)	AASHTO Type II	0.037 (0.94)	N/A	N/A
		Maximum =	0.789 (20.23)	1150	40 (1016)

2.3 Digital Image Correlation in Bridges

Frequent inspection and condition assessment of bridges are required to document their deteriorations and damage over time. The use of non-contact monitoring systems is gaining momentum in the US since they are easier to install and maintain compared with conventional instruments (e.g., LVDTs, strain gauges, etc.). Computer vision is one of the non-contact structural response measurement methods, which is discussed herein.

Vision-based displacement measurement methods usually require either physical (a printed patten attached to the surface of interest) or virtual speckles (or targets) to improve measurements in non-stationary imagery environments. To minimize the use of physical targets, feature points (or virtual markers) can be utilized. For example, Dong and Catbas (2019) used a feature matching strategy to replace handcrafted descriptors with learned descriptors (**Fig. 2.2a-d**). They combined Scale Invariant Feature Transform (SIFT) feature points with Visual Geometry Group (VGG) descriptors as a new strategy for vision-based displacement measurements. A two-span bridge model was selected for testing. A scaled-down model of a mid-size bridge was used and loaded with a toy truck with variable weights. Vision-based displacement measurement methods using four feature matching methods (SIFT, SURF, SIFT-VGG and SURF-VGG), and one conventional displacement sensor, potentiometer (PM), were used to obtain the displacement time histories of a target point on the model bridge loaded with the moving toy truck. The results obtained from the proposed method (SIFT-VGG) were consistent with those obtained from the conventional sensor (**Fig. 2.2e**). Furthermore, the other vision-based methods showed good accuracy in terms of displacement measurements. Subsequently, a field test was performed on a railway bridge to verify the feasibility of the proposed displacement measurement method. The camera was placed at approximately 33 m (108 ft) away from the target region on the bridge. **Figure 2.2f** shows the railway bridge test results. The measured displacements using the proposed method were affected by camera motions. They proposed a method to remove the camera motions from the structural displacements.

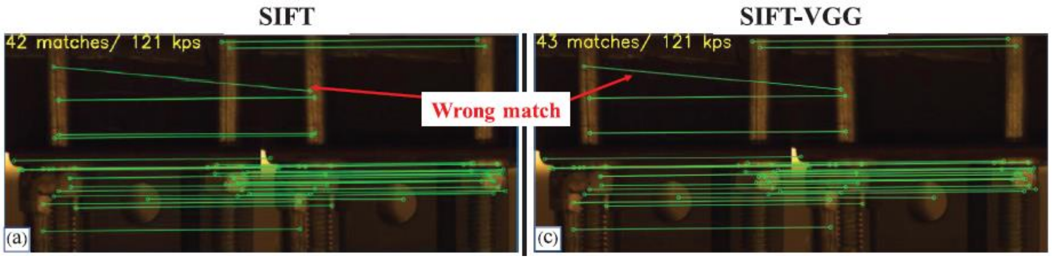

(a) SIFT Feature Matching

(c) SIFT-VGG Feature Matching

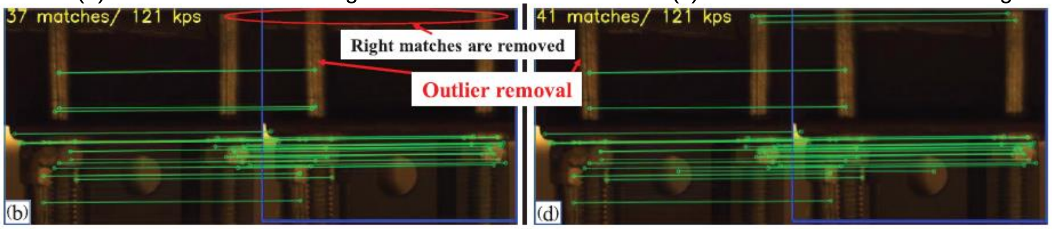

(b) SIFT Outlier Removal

(d) SIFT-VGG Outlier Removal

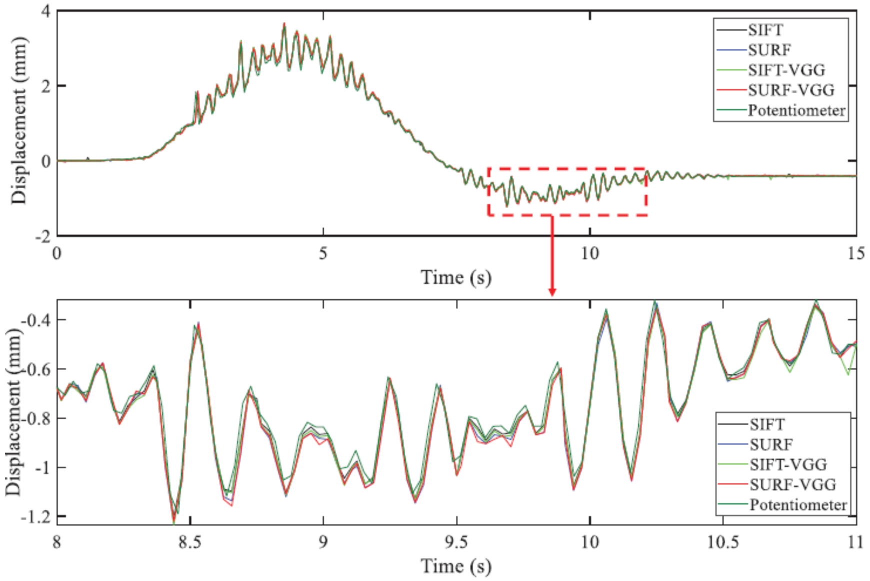

(e) Comparison of Displacement Time Histories for a Scaled Bridge

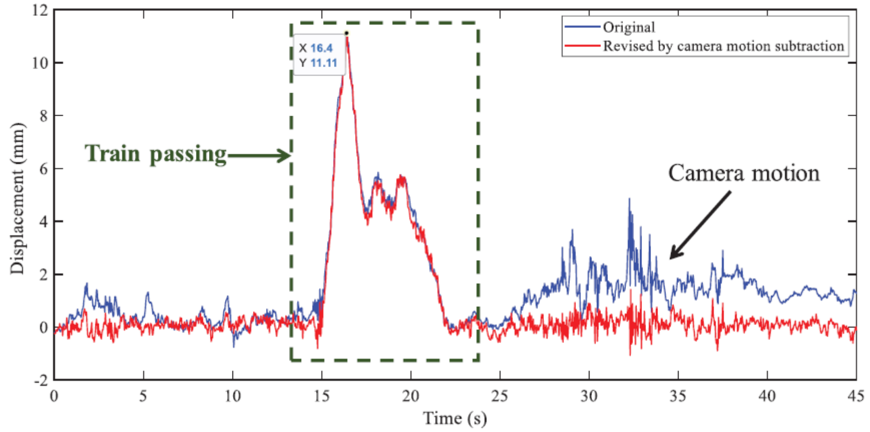

(f) Comparison of Displacement Time Histories for a Real Bridge

Figure 2.2. Sample of DIC Displacement Measurements for Bridges (Dong and Catbas, 2019)

The research team of the abovementioned study implemented the SIFT feature detector and VGG descriptor in a portable system consisting of a set of cameras, a set of synchronization modules, a computer, and a suite of software, to determine girder distribution factors for a highway bridge (Dong et al., 2020). One camera was used to record the traffic to determine which lane of the bridge was loaded and the other cameras were monitoring the deflection of the bridge girders (**Fig. 2.3**). To verify the proposed approach, two sets of experiments were conducted: (1) static loading, and (2) loading under normal traffic. Five potentiometers were installed at the midspan of each girder to measure the displacements. Three cameras were employed to measure the displacements at the same location. **Figure 2.3b** shows a sample displacement measurement by camera and LVDT, and **Fig. 2.3c** shows the girder distribution factors calculated by camera displacements, strains by strain gauges, and an analytical finite element model. Overall, a reasonable accuracy was reported when DIC was used compared with conventional measurements.

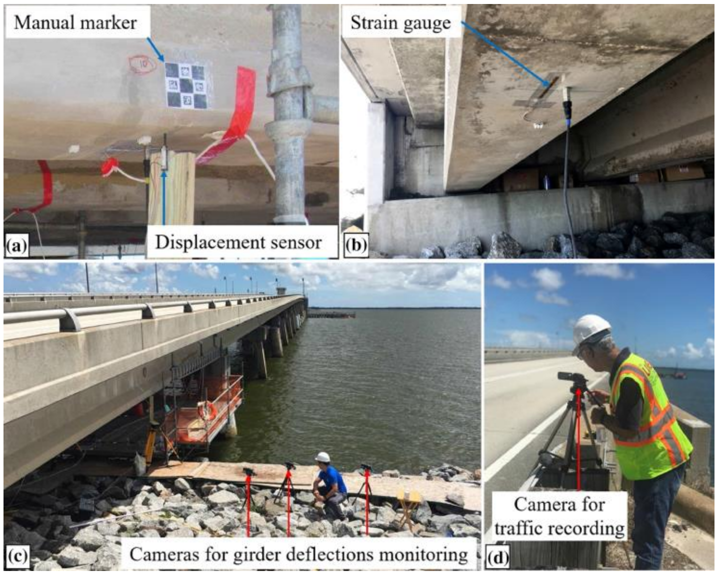

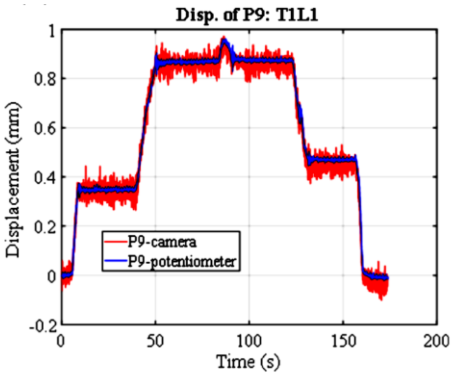

(b) Girder Displacements by DIC

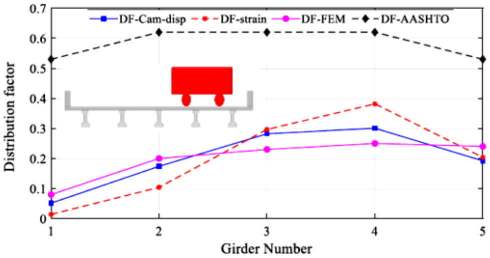

(a) Conventional and DIC Instruments

(c) Girder Distribution Factors

Figure 2.3. Bridge Field Testing and Measurement using DIC (Dong et al., 2020)

Because of some limitations of the current vision-based displacement measurement methods, such as the use of manual targets, parameter adjustment, and significant user involvement to reach a desired accuracy, Dong et al. (2019) proposed a novel structural displacement measurement method using deep learning based full-field optical flow methods. The performance of the proposed method was verified via a laboratory experiment and a field test. The results showed that the proposed method provides a higher accuracy than traditional optical flow algorithms and exhibited comparable results with displacement sensors.

Ngeljaratan and Moustafa (2020) used two high-speed cameras, FasMotion software, and GOM photogrammetric software, to measure displacement response history of a bridge under dynamic testing (**Fig. 2.4a**). They also tested this system on an actual pedestrian truss bridge. The study found that the proposed DIC techniques is viable in dynamic testing with a minimum camera recording rate 30 fps. At low shaking amplitudes, a 26% difference was observed between the displacements measured by DIC and string potentiometers in the shake table testing (**Fig. 2.4b**). This difference was smaller at higher amplitudes of ground shaking. Furthermore, the acceleration response measured by the target-tracking DIC and accelerometers matched well in the bridge model, which further validated the DIC method. For the pedestrian bridge, the maximum coefficient of variation of acceleration from the DIC measurements was 2.2%, that is less than the value retrieved by using accelerometers, about 6%.

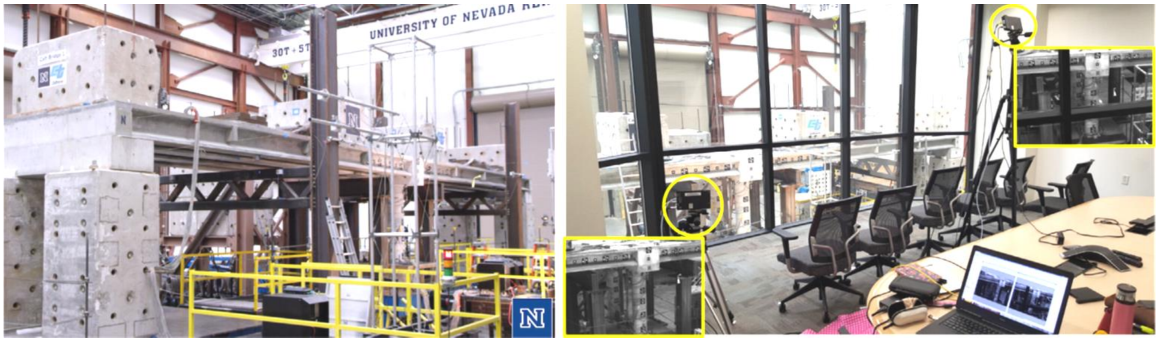

(a) Bridge Model on Shake Table and DIC System

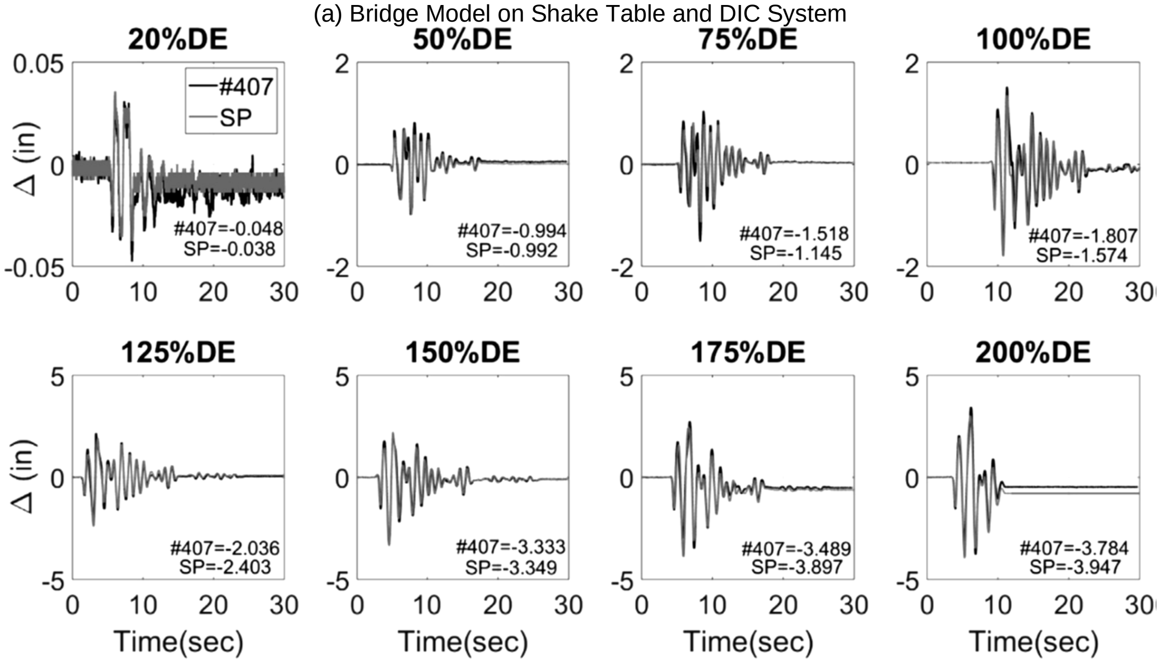

(b) Displacements by DIC (#407) & String Potentiometer

Figure 2.4. DIC Displacement Measurements for Bridge on Shake Table (Ngeljaratan and Moustafa, 2020)

2.4 Structural Response Measurements Using DIC and Drones

As discussed above, DIC systems are viable non-contact tools for the measurement of structural deformations, obtaining full-field strains, and simulating geometry profiles of structures. Moreover, drones have emerged as valuable tools for bridge inspection due to their low-cost operations and accessibility to areas that are either difficult or dangerous for human inspectors. This section reviews the current state-of-the-art developments on the combined use of DIC and drones.

Reagan et al. (2017) proposed to use UAV and DIC to measure displacement fields of bridge target areas. The approach was developed in a laboratory and then was tested for a long-term monitoring of two concrete bridges (**Fig. 2.5**). The study found that the proposed technique can detect changes of the bridge geometry over time with an accuracy between 0.05 and 0.09 mm (0.002 and 0.0035 in.).

(a) Drone Performing an Inspection of Target Areas

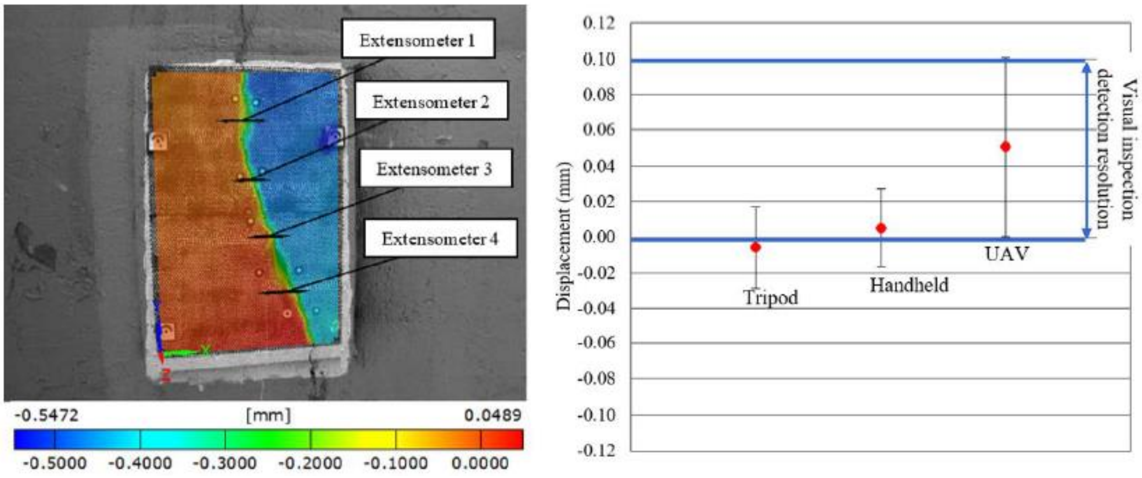

(b) Full-Field X-Displacement Contour (c) Displacement Measurements

Figure 2.5. Full-Field Displacement Monitoring Using Drones (Reagan et al., 2017)

Moreu and Taha (2018) developed a system that integrates a laser doppler vibrometer (LDV) sensor with a copter-type UAV, to perform contact-free, reference-free transverse bridge displacement measurements (**Fig. 2.7a**). Both laboratory and field testing were performed. In the lab testing, the authors conducted multiple tests with varying distances from 3 to 7.5 m (10 to 24.6 ft) to determine the optimal operating distance for the drone. It was observed that the root mean square (RMS) differences between the LVDT and the LDV signals were between 1% and 3% and did not increase with distance (**Fig. 2.7b**). In the field testing, the research team compared the signals for peak and RMS differences and observed that both the peak and the RMS differences were less than 2 mm (0.079 in.). The average peak error of the three tests was approximately 10%, and the average RMS difference was around 8%. These results proved that an LDV mounted on a UAS could be used for measurements of the bridge dynamic displacements.

(a) Drone Measuring Displacements Using LDV on left, LVDT on right

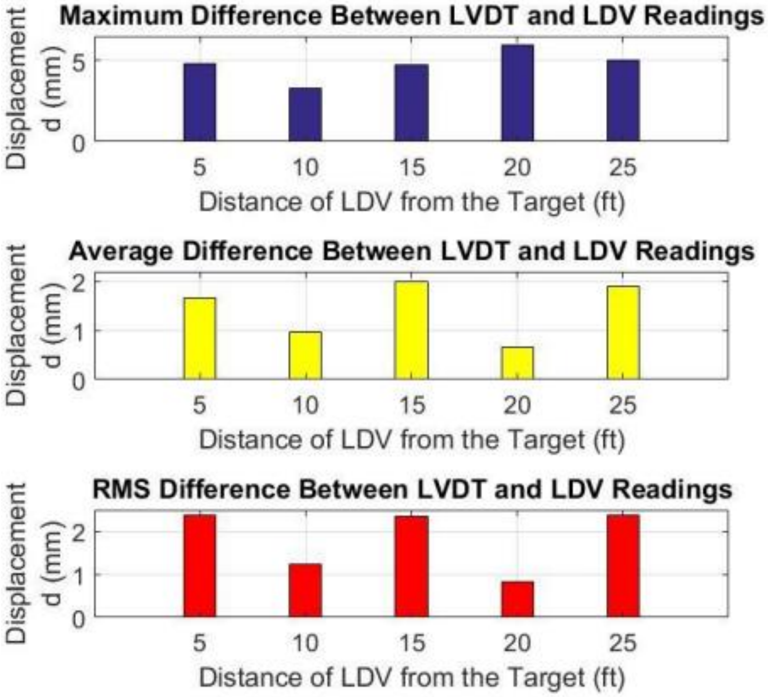

(b) Displacement Measurements by LVDT and LDV

Figure 2.6. Displacement Measurements Using Laser Doppler Vibrometer and Drone (Moreu and Taha, 2018)

Yoon et al. (2018) presented a framework to achieve absolute displacements of a structure from a video taken by a drone using a multi-step approach. First, a target-free method was implemented to extract the relative structural displacement from the video. Next, the six degree-of-freedom camera motions were estimated by tracking the background feature points. Finally, the absolute structural displacement was recovered by combining the relative structural displacement and the camera motion (**Fig. 2.8**).

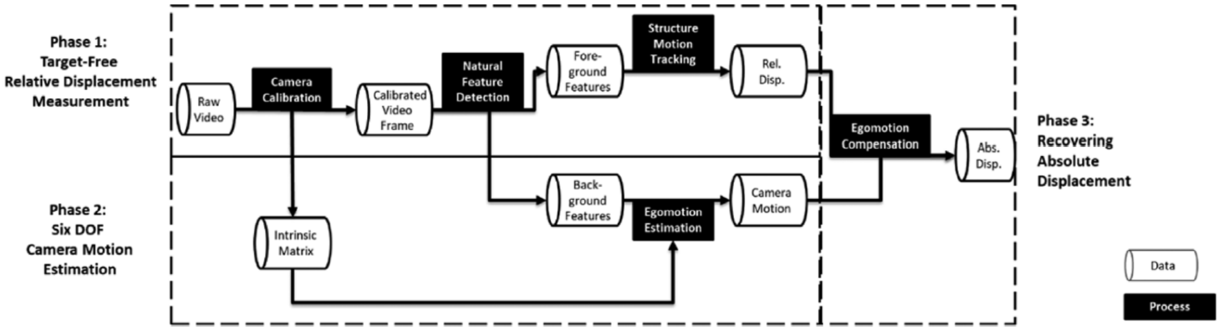

Figure 2.7. Structural Displacement Measurement Using Drone (Yoon et al., 2018)

In laboratory tests, vertical dynamic displacements of a steel truss bridge under train traffic for 250 sec were reproduced using a servo-hydraulic motion simulator (**Fig. 2.8a**). The simulator produced displacements with an accuracy of 0.1%. A DJI Phantom 3 equipped with a 4K resolution camera operating at 24 fps was selected for this experiment. A total of 6,000 frames were obtained. The camera recorded the video at 15 feet (4.57 m) from the motion simulator, which corresponded to the clearance required by the Federal Railroad Administration. **Figure 2.8b** shows the absolute displacement of the bridge determined using the proposed approach. The estimated absolute displacements matched well with the measured absolute displacements of the motion simulator. The root mean square error (RMSE) was 2.14 mm, corresponding to 1.2 pixels of resolution.

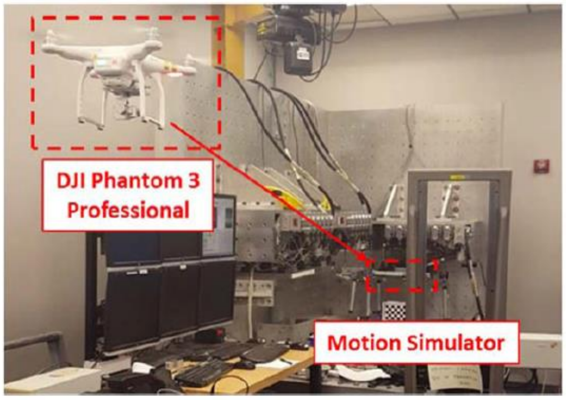

(a) Experiment Setup Using Motion Simulator

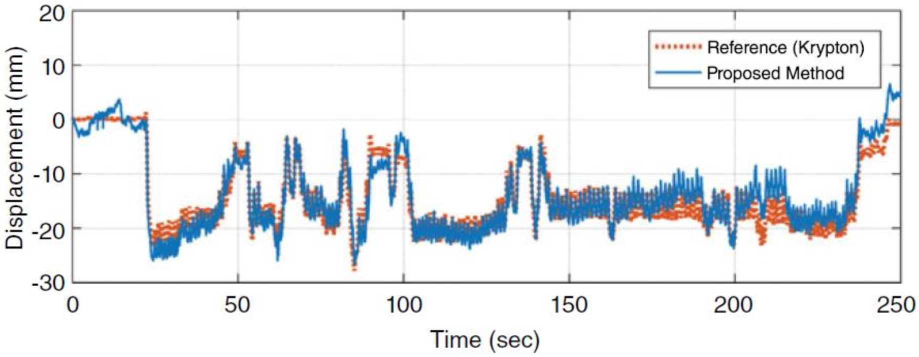

(b) Absolute Displacements

Figure 2.8. Experiment Setup and Measurement Results (Yoon et al., 2018)

Catt et al. (2019) tested a prototype mobile DIC platform in which all the necessary tools were mounted on a drone, which was remotely controlled. The drone was built using a TAROT X8 8-Axis Octocopter FPV Frame TL8X000 Multicopter, with a total payload of 10 kg (**Fig. 2.9**). To perform DIC measurements, two Point Grey GS3-U3-32S4M-C cameras with Fujinon 1:1.4/12.5mm CF12.5HA-1 lenses were used. “VIC 3D” software was used for image processing. During the test, the drone was 2.24 to 2.30 m (7.34-7.54 ft.) away from the target, recording at 10 fps, whereas the target board was deformed by pushing against the center of it from the back side with a ruler, for an approximate deformation of 64 mm (2.5 in.). The maximum deflection of the target board measured by the prototype DIC-drone platform was 57.02 to 60.94 mm (2.25-2.39 in.). However, characteristics of the drone’s flight impacted the results. For example, the software did not track all points in the area of interest (AOI) due to the movement of the target within the field of view (FOV). As shown in **Fig. 2.10**, the target AOI had a large deformation that increased from left to right across the area. However, the target area was flat, similar to that shown in **Fig. 2.10a** for the reference image. The false deformations can be attributed to the drone not being positioned in flight to where the cameras were equidistant to the target.

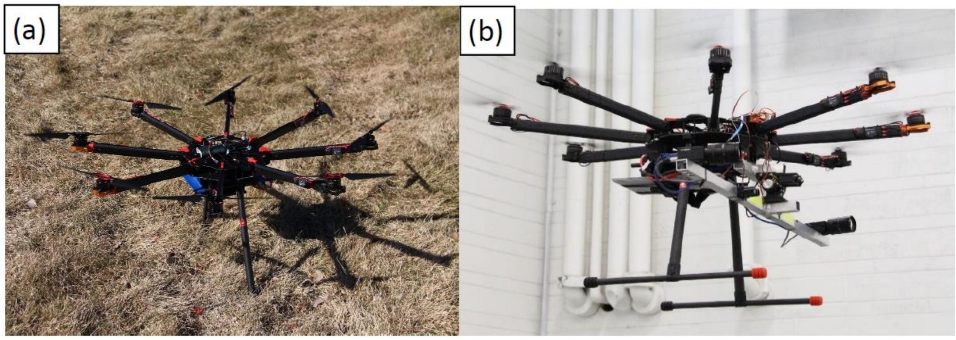

(a) Drone platform without payload (b) Drone platform with payload

Figure 2.9. Drone platform (Catt et al., 2019)

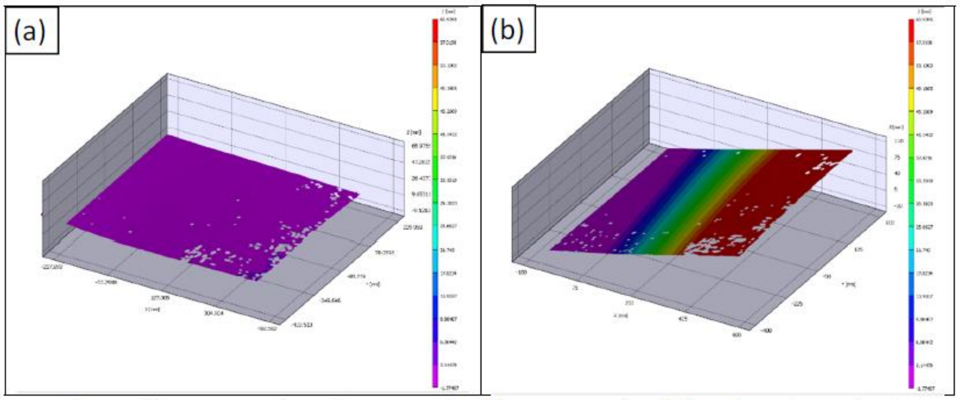

(a) Post-processing Reference 3D Plot (b) Post-processing Deflected AOI (poor photo)

Figure 2.10. Image deformation due to movement of the target within the drone FOV (Catt et al., 2019)

Hoskere et al. (2019) presented camera-enabled UAVs as a new sensing modality, and a novel vision-based data extraction pipeline to conduct modal surveys of full-scale civil infrastructure. The first step of the proposed approach was to obtain video of the vibrating structure through a divide-and-conquer strategy, where the UAV surveyed one portion of the structure at a time (**Fig. 2.11**). Once the video of the structure was obtained, the next step of the proposed approach included a vision-based pipeline to compute the modal properties from the recorded video (**Fig. 2.12**). To eliminate the drone movements from structural deformations, the study used signal filtrations assuming that the drone hovering frequency to be predominantly low (below 0.5 Hz) for UAVs with commercially available gimbals.

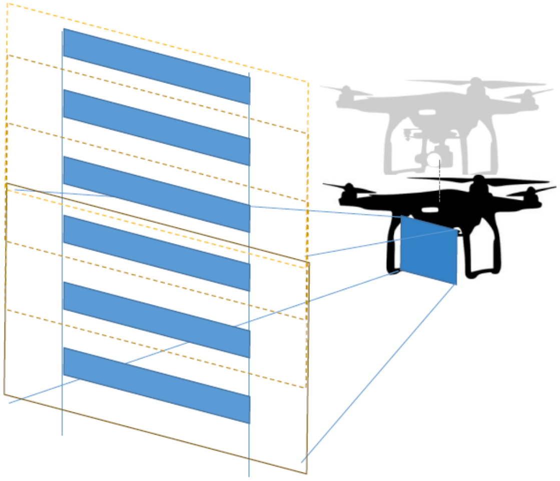

Figure 2.11. Divide-and-Conquer Strategy Proposed by Hoskere et al. (2019)

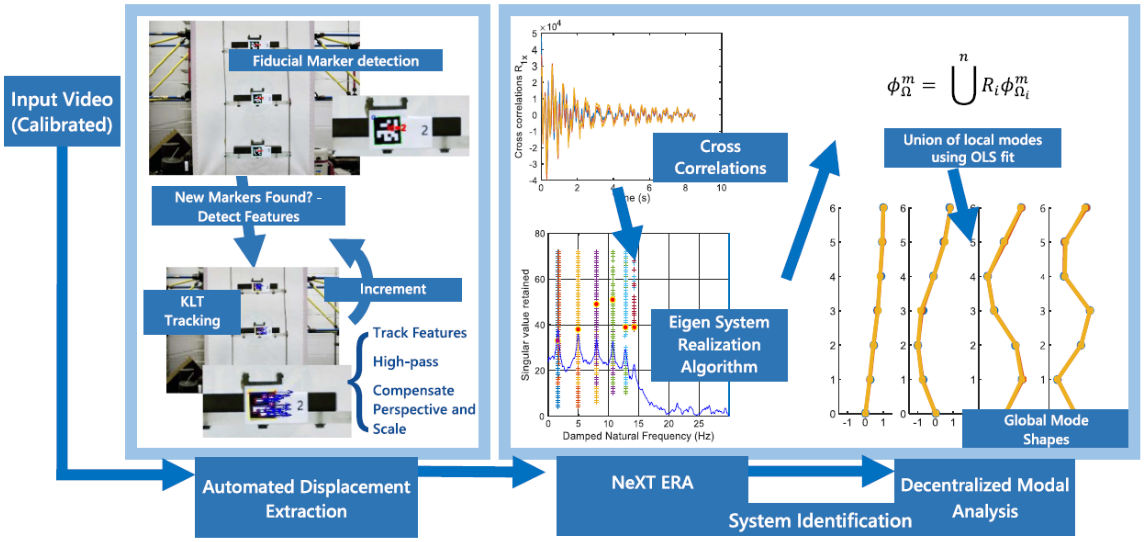

Figure 2.12. Proposed Pipeline for Automated Mode Shape Extraction Using Video Segments (Hoskere et al., 2019)

Shaking table testing of a six-story shear-building showed that the proposed approach can produce reliable results with a less than 0.5% error in the structure natural frequencies, and the modal assurance criterion (MAC) values all being greater than 0.996. An additional test was conducted on a full-scale pedestrian suspension bridge. The results showed that MAC values were all above 0.925, and the difference in the natural frequencies was less than 1.6% for three modes included in the analysis. One drawback of the proposed approach was that it cannot measure structural frequencies below 0.5 Hz by using commercial grade UAVs (such as DJI Phantom 4) limiting its application for long-span bridges. Also, the measurement accuracy of the proposed system depends on the motion oscillation of the UAV while hovering; for example, sudden wind changes can affect the accuracy. It can be noted that the MAC values obtained from the field test were not as high as the laboratory test. The main cause for the lower accuracy was an increased frequency and amplitude of oscillation of the UAV due to wind gusts. This issue might be addressed by using heavier drones and more advanced autopilots to achieve stable flights while videos and images are acquired. Moreover, hovering accuracy might be further improved by using drones equipped with Real Time Kinematics Global Positioning System (RTK GPS) for centimeter level navigation.

Khuc et al. (2020) introduced an enhanced noncontact displacement measurement method that employed UAV and computer vision algorithms. In particular, the swaying displacements of tower-type structures were measured by a UAV without physical calibration pattern (or target). This was achieved via elimination of three UAV translations using a known-dimension part of the monitored structure, combined with some advanced computer vision algorithms, such as key-point detection, Hough transform, and Canny edge detection (**Fig. 2.13**).

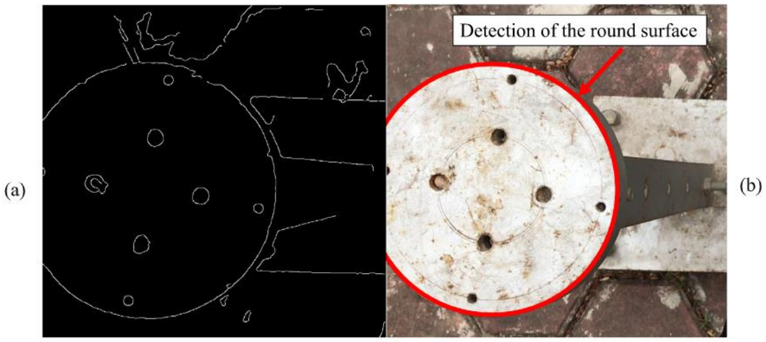

(a) Canny Edge Detection (b) Hough Transform Algorithm

Figure 2.13. Algorithms for Detecting Steel Round Plate (Khuc et al., 2020)

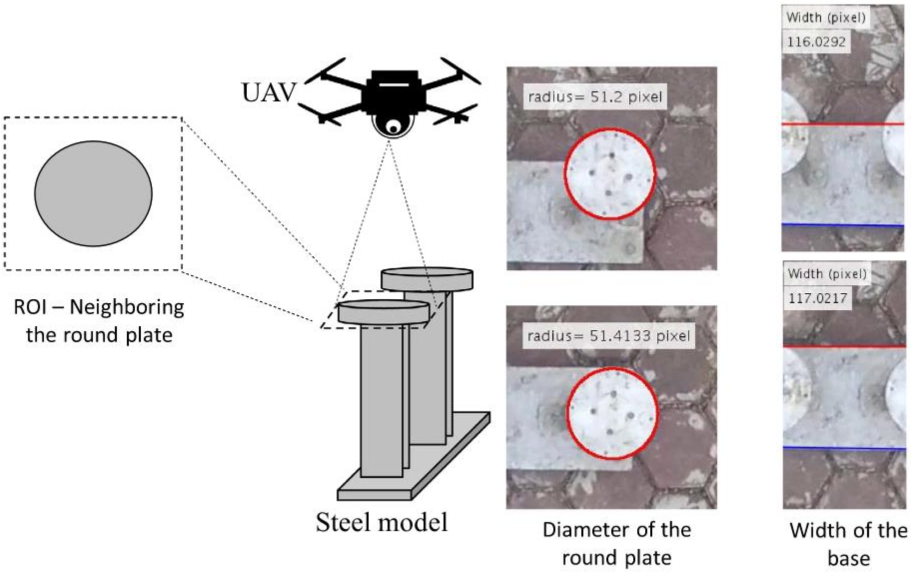

Figure 2.14. Measurement of Steel Plate Properties at 1st and 150th Images in UAV Video Clip with Autonomous Scheme (Khuc et al., 2020)

UAV motions were calculated by visually tracking fixed objects in the background, whereas scale factors (pixel to length) were obtained by measuring a known-dimension object (**Fig. 2.14**). The proposed UAV vision-based displacement measurement method was verified on a steel model, which was a tower-type apparatus for dynamic experiments (**Fig. 2.15**). The sensing system used in this verification was an integration of a consumer-grade UAV (DJI Phantom 3), a camcorder Canon VIXIA HF R42 attached to a tripod, and an accelerometer wired to a DAQ (NI-9234 module). In this experiment, displacements of the round steel plate on the top of the tower were monitored using UAV.

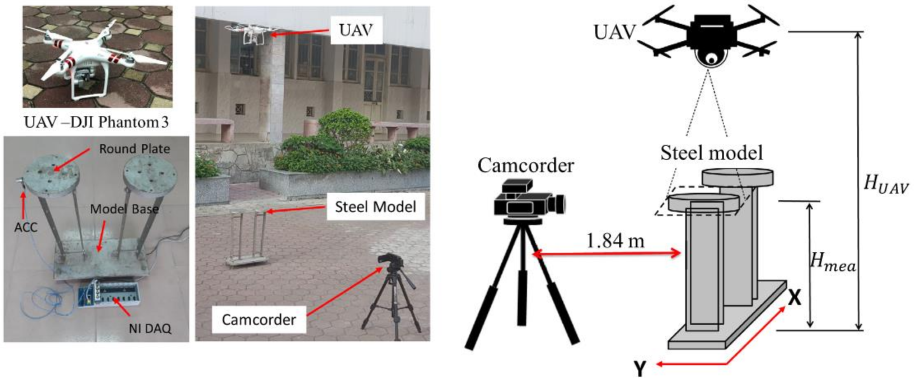

Figure 2.15. Experimental Setup with Steel Model, UAV, and Fixed Camcorder (Khuc et al., 2020)

The results showed that the motions of the moving object determined by both methods highly matched in terms of displacement levels and vibration pattern. However, several mismatching patterns were observed on the time windows between 35-40 sec and 52-56 sec, which could have been induced by sudden turbulences and movements of the UAV under a strong wind during hovering (**Fig. 2.16**). The determination coefficient, R^2, using the outcomes from both methods was 0.9723, which is very close to 1.0, indicating good correlation between displacements measured by UAV and the ground camera.

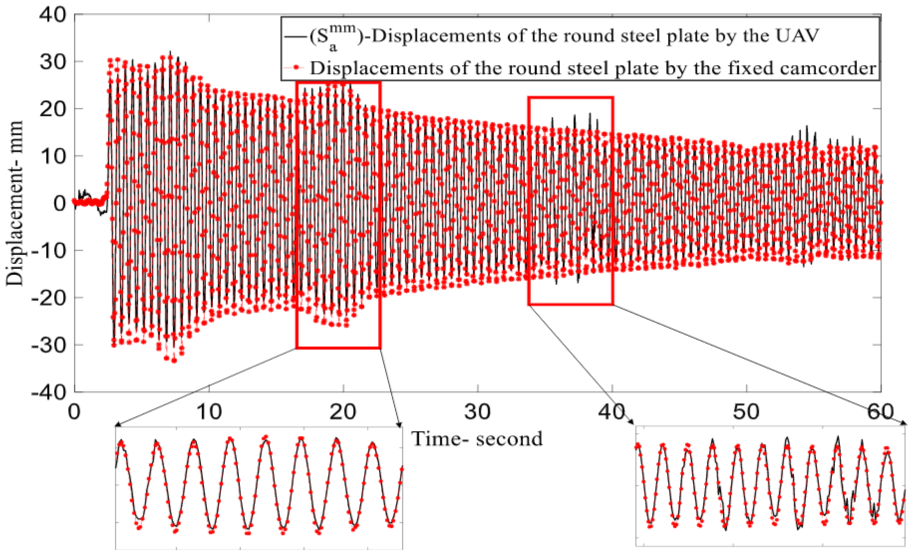

Figure 2.16. Displacements of Steel Model Using UAV and Fixed Camcorder. (Khuc et al., 2020)

Chen et al. (2021) presented a homography-based method by combining UAV and DIC for vibration measurements of bridges. From experiments in an outdoor environment, it was found that the homography transformation established from the reference points can be used to effectively eliminate the false displacement caused by the UAV motion, and then the structural displacement can be obtained. In addition, natural frequencies and mode shapes of a bridge model obtained by a UAV were close to those measured with a fixed camera. Moreover, the UAV measurements were found more accurate at short distances.

Perry and Guo (2021) presented a new remote sensing technique to measure dynamic structural response of 3D structures by integrating both optical and infrared (IR) cameras with a UAV platform, and by developing new data processing algorithms. This represents an advantage over the existing UAV-based displacement measurement techniques that allow the measurements in only one or two directions using optical cameras or laser sensors, and a portable alternative for short-term monitoring or modal testing. Furthermore, the proposed technique allows measuring the response over the entire FOV of the sensors with a single sensor suite. The study achieved a fast data processing and computational efficiency. In one epoch, it took about 0.071 sec to extract the targets, track their movements, and measure both regions of interest (ROI) and stationary references. The accuracy achieved by the proposed technique (in terms of RMSE) compared with other related work in the literature was from 5 to 13%.

2.5 3D Reconstruction of Bridge Models Using Drones

A 3D reconstructed bridge model provides a virtual reality platform to remotely inspect a bridge. Furthermore, the bridge geometry and apparent damage can be determined using this technology, and finite element models could be extracted from a 3D reconstructed bridge model. Utilizing an integrated combination of a UAV and computer vision may decrease costs and expedite inspections.

In this context, Lattanzi and Miller (2014) compared two methods for reconstructing 3D scenes. The two methods considered are dense structure-from-motion (DSfM) and image mosaicking (IM). The primary metrics used in the comparison include the accuracy of the reconstructions for inspection measurement purposes, the nature and prevalence of reconstruction artifacts, and the resolution demands for adequate reconstruction accuracy. To test the accuracy of these methods, an aluminum section, a scaled structure, and a bridge footing and column were chosen as shown in **Fig. 2.17**. For the aluminum section, both methods resulted in consistent and scale-accurate reconstructions, with discrepancies less than 6 mm, which was on the order of the potential accuracy of a field inspection. For the scaled structure, the IM method provided accurate results for all measurements, with discrepancies less than 3 mm. The large gaps and inconsistencies in the DSfM reconstruction for this case prevented accurate measurement of any of the features. For the bridge column, both methods produced scale-accurate measurements, with most measurement discrepancies less than 3 mm. Regarding artifacts, overall, those created by the IM method were typically easy to spot and generally resulted in a distortion of existing features rather than in the introduction of realistic looking features not present in the actual structure (**Fig. 2.17**). Regarding the resolution, the DSfM method resulted in meshes with several orders of magnitude more vertices than the IM approach, and this could be challenging for large-scale structures. A proof-of-concept verification using a UAV (a human-piloted Parrot AR Drone 2.0 UAV with an 11-megapixel auxiliary camera) was carried out on a bridge. The bridge was a reinforced concrete arch pedestrian bridge. The maximum viewing distance of the inspection robot was chosen to capture images at a pixel density greater than 0.8 pixel/mm. It was observed that bright lighting or heavy shadows make the reconstruction process more challenging. The DSfM method created artifacts of a similar nature to those of the small-scale test. The areas with dark shadows during the reconstruction process were problematic due to the low-image texture in those regions. Further, several of the relatively large planar surfaces on the bridge distorted the reconstruction as well.

(a) Mosaicking Reconstruction

(b) Dense Structure-from-Motion Reconstruction

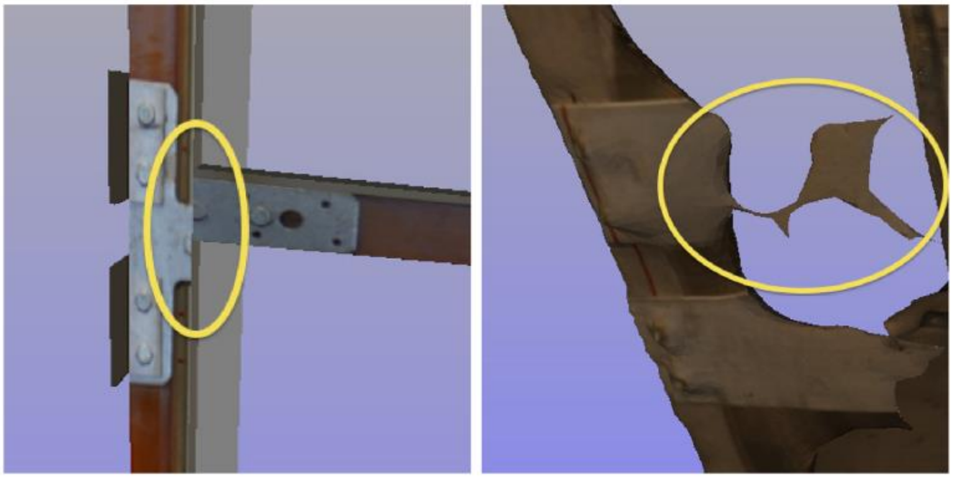

(c) Mosaicking Artifact

(d) Dense Structure-from-Motion Artifact

Figure 2.17. Reconstruction of a Scaled Structure (Lattanzi and Miller, 2014)

Khaloo et al. (2018) implemented a 3D model of a bridge using UAV captured images and a hierarchical DSfM algorithm. The image-based 3D point clouds were generated using an adaptation of a DSfM process referred to as Hierarchical Point Cloud Generation (HPCG). The results are compared against models generated through laser scanning. From the rendered viewpoint, the quality of the two models were close. However, the noise characteristics were very different between these two 3D reconstruction techniques. The LiDAR scanner produced a rather consistent precision and very low noise model with a mean estimated roughness value of 1.8 mm. However, due to imperfect correspondence between 3D point clouds, higher local noise was consequently introduced into the final model within the registration process of multiple scans. The image-based 3D reconstruction exhibited noise that was one to two greater orders of magnitude, based on the calculated roughness values. This increase in noise can be attributed in part to fundamental differences in 3D reconstruction methods, and it can also be due to the complex interactions of the bridge with the low contrast sky that was in the background of many captured images, highlighting the impact of environmental and radiometric factors on the quality of the image-based reconstruction. In terms of the deficiencies and damages that were visually apparent, the more flexible nature of UAV imaging provided a more accurate and complete dense 3D model than the LiDAR model. Indeed, findings suggest that LiDAR could effectively generate point cloud models for inspection purposes when it was possible to place the scanner near the structure. The true value of the UAV inspection system was the ability to accurately reconstruct details in regions where it was not possible to set up a LiDAR scanner within reasonable proximity.

Chen et al. (2019) proposed a process using an imagery-based point cloud for 3D bridge reconstruction and a low-cost UAV (**Fig. 2.18**). In general, the study demonstrated that the method could offer significant advantages in equipment cost, surveying time, point distribution, and ultimate data coverage. However, problems such as high noise levels, low geometry accuracy, and long postprocessing times were reported.

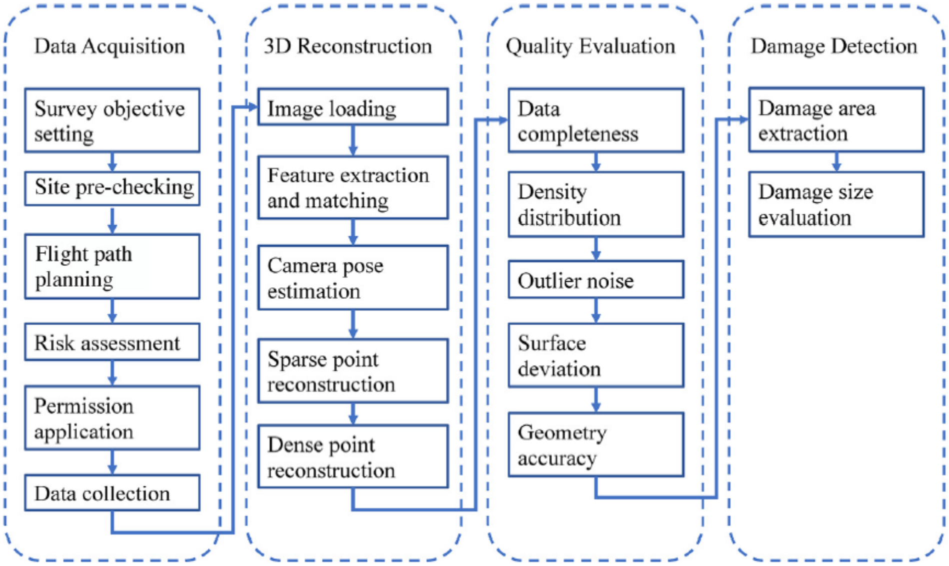

Figure 2.18. Framework for UAV Inspection (Chen et al., 2019)

Liu et al. (2020) proposed an image-based crack assessment methodology for bridge piers using UAV and 3D scene reconstruction, which corrects both the perspective distortion and geometry distortion by non-flat structural surfaces, and localizes the crack (**Fig. 2.19**).

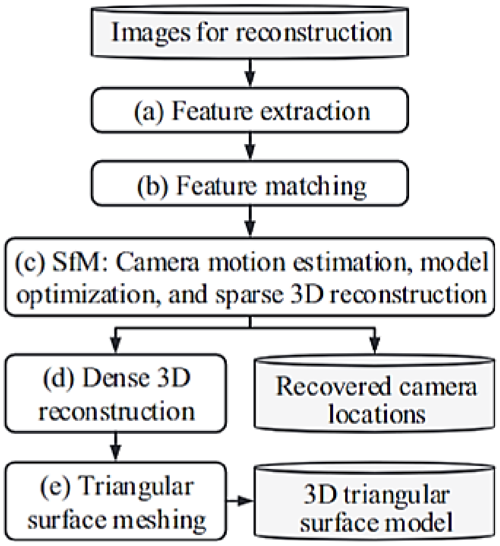

Figure 2.19. Flow diagram of the process of 3D scene and surface reconstruction (Liu et al., 2020)

Liu et al. (2020) performed 3D reconstructed crack assessment of a bridge pier using a UAV (DJI Inspire 2 with X5S camera). The obtained crack width feature sequences were projected onto the 3D triangulated surface model. After size correction, the width of the crack was obtained by calculating the distance between the two projected crack width points. The shape of the projected cracks matched the shape of the actual cracks, as shown in **Fig. 2.20**. In addition, when the measured crack width was more than 7 pixels, the relative error was less than 10%.

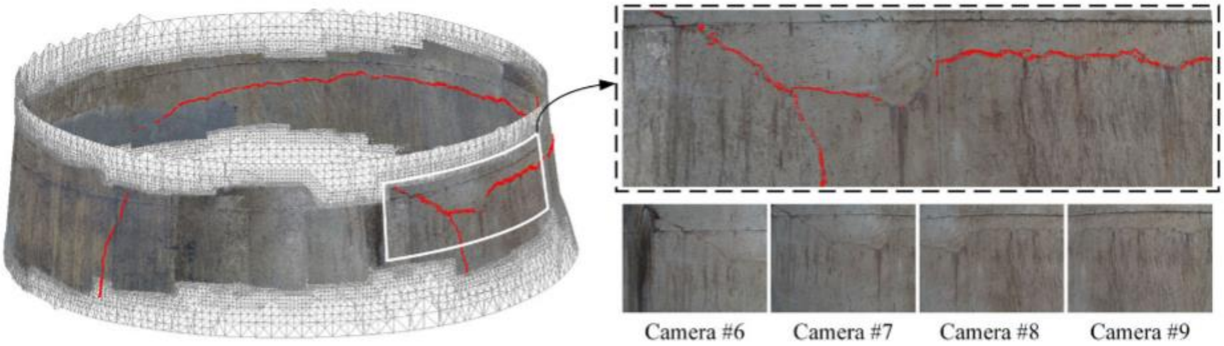

Figure 2.20. 3D Reconstruction and Crack Localization of Bridge Column (Liu et al., 2020)

Popescu et al. (2019) compared the performance of three different imaging technologies for 3D geometric modeling of existing structures: terrestrial laser scanning, close-range photogrammetry, and infrared scanning. The technologies were compared in terms of geometric deviations, visualization capabilities, inspector's experience, and degree of automation. The results suggested that all methods were viable to create 3D models; however, with different levels of accuracies. Measurements based on terrestrial laser scanning were closer to the actual dimensions (less than 2.2% error) compared with photogrammetry (up to 12.2% error) and infrared scanning (up to 2.3% error).

2.6 Recent Developments on Sensing Technologies

Recent sensing technologies to monitor structural responses during load testing of reinforced concrete bridges have been reviewed in Garnica et al. (2022). In addition to DIC, virtual visual sensors (VVS), microwave interferometer radar, and acoustic emission sensors have been utilized for structural measurements.

The first technique proposes that every pixel in a digital video taken from a structure represents a candidate of a VVS. The methodology uses a Eulerian specification where a pixel is selected and its intensity is monitored over time and analyzed using the Fast Fourier Transform, to reveal the fundamental frequency of vibration. Natural frequencies of vibration can be extracted using the Discrete Fourier Transform and the displacement amplitudes can be estimated using targets (**Fig. 2.21**). The equipment needed to implement this technique consists of a digital camera, an algorithm to process the video and to analyze the vibration, and targets to improve the signal. The main advantages are that it is a non-contact technique, thus multiple objects can be monitored continuously, and it has comparable accuracy to accelerometer-based techniques. The limitations are that small structural vibrations are difficult to measure. Further, the accuracy depends on the resolution and frame rate of the digital camera, the distance to the region of interest, the optical lens zoom, and the spatial gradient.

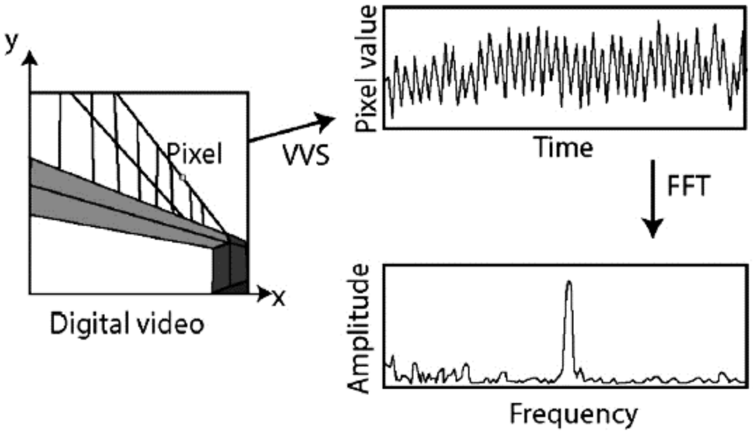

Figure 2.21. Methodology to Measure Vibrations Using Virtual Visual Sensors (Garnica et al., 2022)

Microwave interferometer radar is a sensor that detects differential displacements of targets in its cone of view by exploiting the phase information of the back-reflected microwave signal (**Fig. 2.22**). The phase differences depend on the distance between the radar and the target. If the target moves fractions of a wavelength, the differential displacement can be detected as a phase shift. The radar transmits a modulated signal that provides the sensor with the ability to detect displacements of several targets. The microwave radar measures the static deflections of several points on a large structure as well as vibrations to identify resonant frequencies and mode shapes. Every discontinuity on the structure is a potential reflecting target. A microwave interferometer radar usually consists of a sensor module mounted on a tripod, a control unit, and a power supply. The main benefits of the microwave interferometer radar are that it is a real-time remote sensing technique and operates day and night and in all weather conditions. Some of the limitations are that it only measures the relative displacements of the targets in the line of sight thus the location of the measurements requires careful planning with the absence of disturbances such as vegetation.

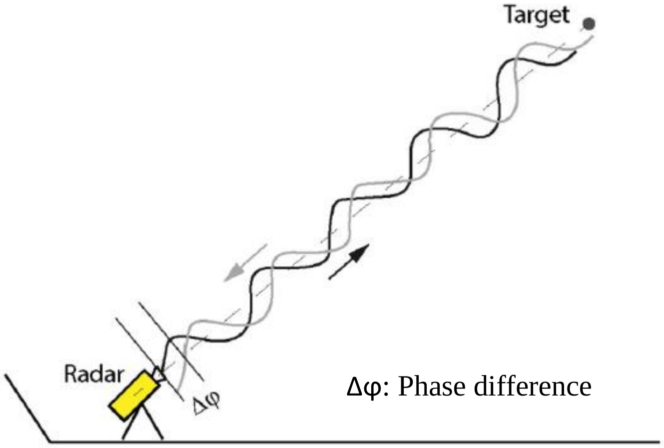

Figure 2.22. Working Principle of Microwave Interferometric Radar (Garnica et al., 2022)

CHAPTER 3. DEVELOPMENT OF DIC-DRONE BASED DISPLACEMENT MEASUREMENT TOOLS

3.1 Introduction

A review of the most relevant studies on bridge field testing and the use of digital image correlation (DIC) was presented in the previous chapter. The main objective of the study is to perform field testing of bridges using drones and DIC. In this chapter, the steps taken for the development of DIC drone-based displacement measurement tools are discussed. Several configurations were studied to achieve the best performance in terms of costs, usability, and accuracy. The configurations are different in mission strategies, hardware, software, and DIC markers. The hardware components are the drone and its payload, which is mainly composed of a set of cameras, a mini-PC, and an electric battery. The software must be able to run on the mini-PC that is mounted on the drone and must achieve reasonable accuracy when measuring structural displacements. Open-source computer programs might be preferred to lower the costs. DIC markers can be either (predefined) or natural (virtual). Physical markers are usually a printout of black squares/circles with white dots/shapes inside. Non-physical markers can be defined by a set of feature points extracted from the natural characteristics or defects of members (e.g., construction lines, discoloration, spots, etc.). Proposed mission strategies and the components of the DIC-drone systems are discussed in this chapter.

3.2 Proposed Mission Strategies

In this section, different mission strategies and the select one are introduced. A mission strategy in this project refers to the overall methodology to perform bridge field testing using the combined incorporation of DIC and drones.

3.2.1 Strategy A – Ground and Drone Cameras

A fleet of drones (two or more drones depending on the bridge type, geometry, and girder configurations), each equipped with a single DIC camera, will monitor the bridge girder vertical displacements during the field testing (**Fig. 3.1**). DIC markers are placed on girders. Furthermore, the drone movement is measured using a ground camera placed close to the bridge tracking a set of markers installed on the drone. Therefore, the ground camera(s) can accurately identify, at any instance, the current position of the drone, which in turn, is acquiring the position of the markers on the bridge. By properly combining this chain of relative positions, the absolute position of the DIC targets as the girder displacement can be derived.

The Drone Photo by Unknown Author is licensed under CC BY-SA-NC
This Camera Photo by Unknown Author is licensed under CC BY-SA

Figure 3.1. Proposed DIC Mission Strategy A Using Ground and Drone Cameras

3.2.2 Strategy B – Alternative Ground and Drone Cameras

Alternative to the previous method, the ground camera can monitor the vertical displacement of an exterior girder at either side of the bridge (**Fig. 3.2**). Each drone has a single camera monitoring the DIC targets placed on girders. In this case, the drone camera must always see DIC markers on two girders. The ground camera will produce the vertical displacement of the exterior girder as needed for the girder distribution factor analysis. The displacement of the second girder next to the exterior girder is the exterior girder displacement plus the relative DIC measurements from the first drone watching the first and the second girders. Note that the first drone will see the relative displacements between the two markers. The displacement of the third girder is calculated by adding the relative measurements of two DIC markers placed on the second and third girders, which are seen by the second drone. Similarly, the displacement of the remaining girders can be determined.

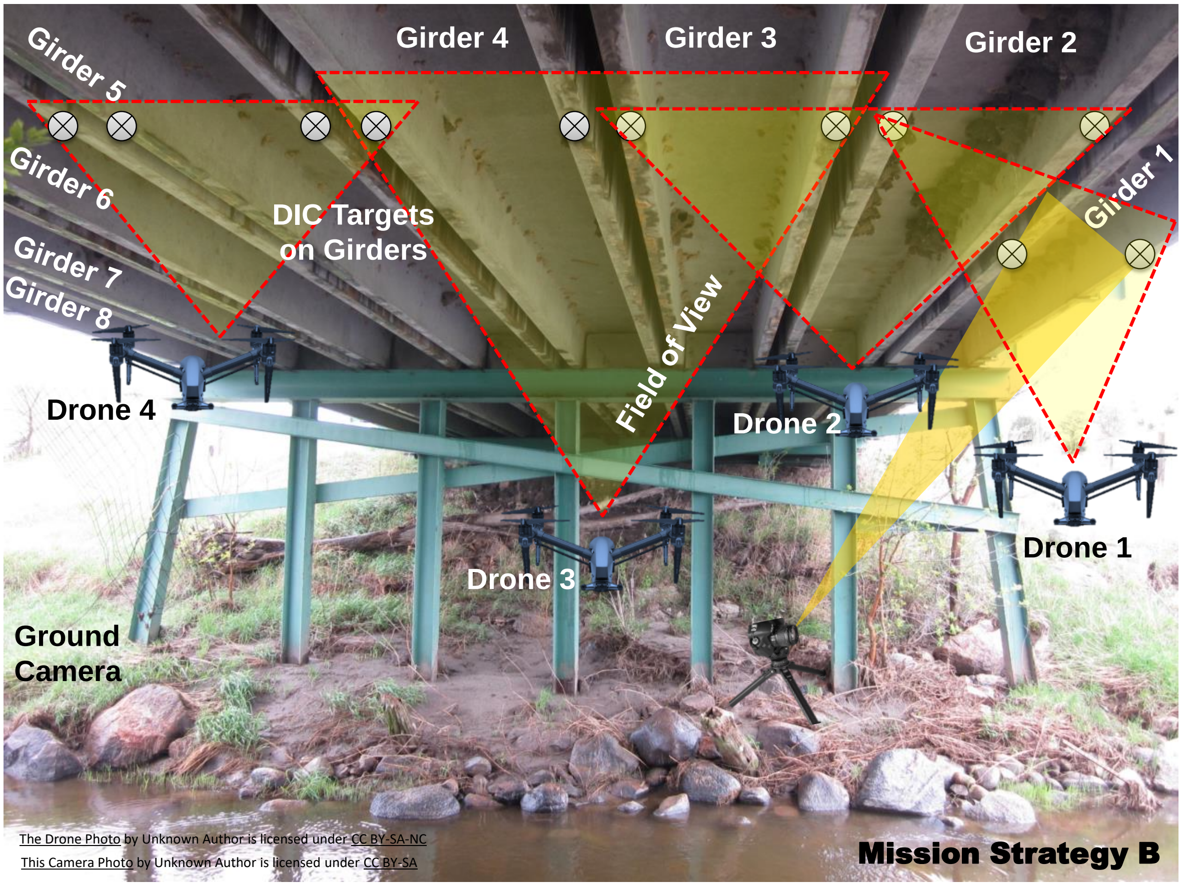

Figure 3.2. Proposed DIC Mission Strategy B Using Alternative Ground and Drone Cameras

3.2.3 Strategy C – Drone with Two Cameras

In the third strategy, a fleet of drones, each equipped with two DIC cameras, will monitor the bridge girder vertical displacements during the field testing (**Fig. 3.3**). For each drone, one camera acquires the position of the target markers on the bridge, whereas the second camera looks at the reference marker placed on the bridge components with negligible vertical displacements during testing such as bents and abutments. Virtual targets can also be utilized in this method. The difference between the DIC measurements from the reference and target makers is the girder displacement in which the drone motions are removed.

Strategy C is advantageous since it does not require any ground camera. Indeed, ground cameras have limited use on over-the-water bridges. Further, a single ground camera might not be able to capture all drones at a time thus multiple ground cameras might be needed. Due to these advantages, the present study will adopt Strategy C.

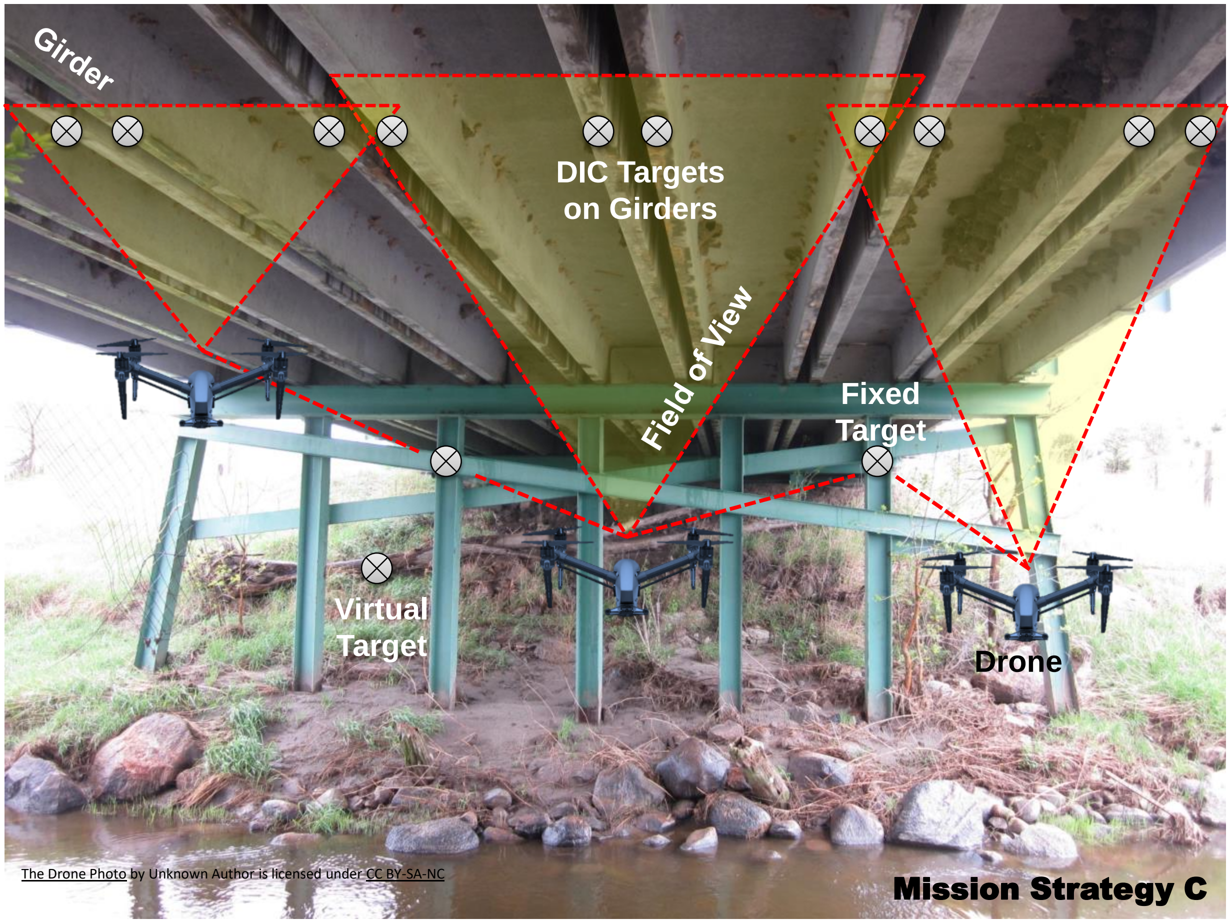

The Drone Photo by Unknown Author is licensed under CC BY-SA-NC

Figure 3.3. Proposed DIC Mission Strategy C Using Drone with Two Cameras

3.3 DIC Markers

The use of physical and natural (virtual) markers were discussed above. In this pilot study, we have used physical ArUco markers (**Fig. 3.4**). An ArUco marker is a synthetic square marker composed of a wide black border and an inner binary matrix that determines its identifier (ID). The black border facilitates its fast detection in the image, and the binary codification allows its identification and the application of error detection and correction techniques.

The marker size determines the size of the internal matrix. For instance, a marker size of 4×4 is composed of 16 bits. It must be noted that a marker can be found rotated in the environment. However, the detection process needs to be able to determine its original orientation, so that each corner is identified unequivocally. A marker dictionary is the set of markers that is considered in a specific application. It is simply the list of binary codifications of each of its markers. The main properties of a dictionary are the dictionary size and the marker size. The dictionary size is the number of markers that composes the dictionary. The marker size is the size of those markers (the number of bits). The ArUco module includes some predefined dictionaries covering a range of different dictionary sizes and marker sizes (OpenCV, 2022a). An example of a single ArUco marker is shown in **Fig. 3.4**.

In this project, both single ArUco markers and clusters composed of a set of 4, 9, and 16 ArUco markers (**Fig. 3.5**) were utilized to find the best option for bridge field testing. The dimension of the ArUco marker (or the cluster of markers) was selected based on the distance of the marker from the camera and the lens focal length. Note that the lens focal length affects the camera field-of-view (FOV) and consequently, the marker/image fill factor (i.e., how big is the marker with respect to the full image). Another important factor is that the marker should be printed on a flat surface and with a high contrast ratio. This reduced errors during the detection and pose estimation processes described in the next section.

Figure 3.4. Sample of ArUco Marker with a 4x4 Dictionary and ID of 0

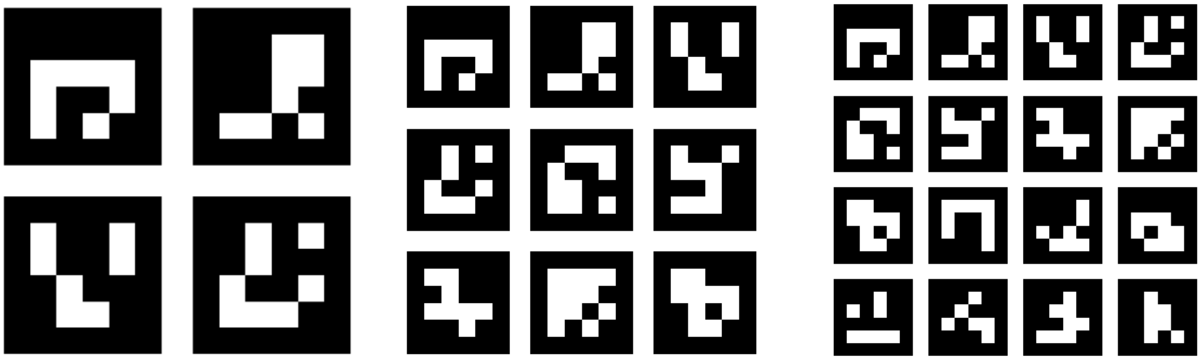

(a) Clusters of 4 Markers (b) Clusters of 9 Markers (c) Clusters of 16 Markers

Figure 3.5. Samples of ArUco Marker Clusters from 4x4 Dictionary

ID0 marker is located at the top left corner of each marker cluster

3.4 DIC Software

In this section, the camera calibration process and the DIC software that analyzes the recorded videos for structural displacements are introduced. Python is chosen as the programming language, in combination with OpenCV, an open-source computer vision library, which implements real-time computer vision algorithms.

3.4.1 Camera Calibration

Camera calibration estimates the parameters of a lens and an imaging sensor of a camera to correct lens distortion. Moreover, it can be used to measure the size of an object in world units or determine the location of the camera in the scene, if considering multiple cameras. A DIC system's resolution and accuracy of measurements rely on both the camera sensor and lens quality as well as the calibration process.

In this project, the camera calibration is performed using built-in functions of OpenCV (OpenCV, 2022b). These functions use a so-called pinhole camera model (**Fig. 3.6**). A pinhole camera is a simple camera without a lens and with a single small aperture. Light rays pass through the aperture and project an inverted image on the opposite side of the camera.

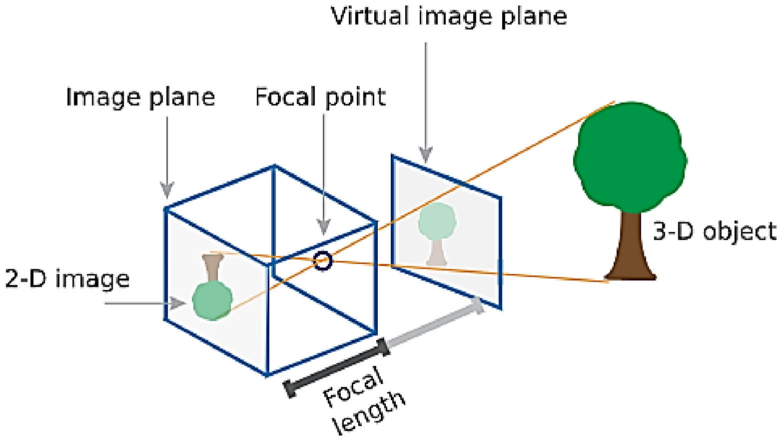

Figure 3.6. Pinhole Camera Model

The pinhole camera model does not account for lens distortion because an original pinhole camera does not have a lens. To accurately represent a real camera, the full camera model used by the algorithm includes radial and tangential lens distortions. The radial distortion causes straight lines to appear curved. The radial distortion becomes larger as points are further away from the center of the image. The radial distortion can be represented as:

$$\begin{aligned} x_{distorted} &= x(1 + k_1 r^2 + k_2 r^4 + k_3 r^6) \\ y_{distorted} &= y(1 + k_1 r^2 + k_2 r^4 + k_3 r^6) \\ r^2 &= x^2 + y^2 \end{aligned} \quad \text{(Eq. 3.1)}$$

where k_1 to k_3 are the radial distortion coefficients of the lens and x and y are the undistorted pixel locations.

The tangential distortion occurs when the lens and the image plane are not parallel. The amount of tangential distortion can be represented as:

$$x_{distorted} = x + [2p_1xy + p_2(r^2 + 2x^2)]$$

$$y_{distorted} = y + [2p_2xy + p_1(r^2 + 2y^2)] \qquad \text{(Eq. 3.2)}$$

$$r^2 = x^2 + y^2$$

where $p_{1,2}$ are the tangential distortion coefficients of the lens, and x and y are the undistorted pixel locations.

In both types of distortions, x and y are expressed in normalized image coordinates, which are calculated from pixel coordinates by translating to the optical center and dividing by the focal length in pixels. Thus, x and y are dimensionless. The vector of distortion coefficients can be defined as:

$$Distortion\ coefficients = [\,k_1 \ \ k_2 \ \ p_1 \ \ p_2 \ \ k_3] \qquad \text{(Eq. 3.3)}$$

In addition to this, intrinsic and extrinsic parameters of the camera must be determined. Intrinsic parameters are specific to camera and include information such as focal length (f_x, f_y) and optical centers (c_x, c_y). The focal length and optical centers are used to create a camera matrix to remove lens distortions of a specific camera. Therefore, the camera matrix is unique to each camera, so once calculated, it can be reused on other images taken by the same camera. It is expressed by a 3×3 matrix:

$$Camera\ matrix = \begin{bmatrix} f_x & 0 & c_x \\ 0 & f_y & c_y \\ 0 & 0 & 1 \end{bmatrix} \qquad \text{(Eq. 3.4)}$$

Extrinsic parameters correspond to a rotation matrix (*R*) and a translation vector (*t*). They translate a coordinate of a 3D point (world) to a camera coordinate system. The camera coordinates are then mapped into the image plane using the intrinsic parameters.

To estimate the camera parameters (intrinsic, extrinsic, and distortion coefficients), 3D world points and their corresponding 2D image points are needed. To find these correspondences, a calibration pattern, such as a checkerboard (**Fig. 3.7**), is usually utilized.

Figure 3.7. Calibration Boards Used for Cameras

The calibration process involves taking images (i.e., 2D image points) of a checkerboard at different locations and orientations (i.e., 3D real-world points). The 2D image points are locations where two black squares touch each other on the checkerboard. Several images are usually taken by moving the checkerboard in a way that it can fully cover the camera FOV, and by changing its orientations (**Fig. 3.8**). Using these correspondences, it is possible to obtain the camera parameters.

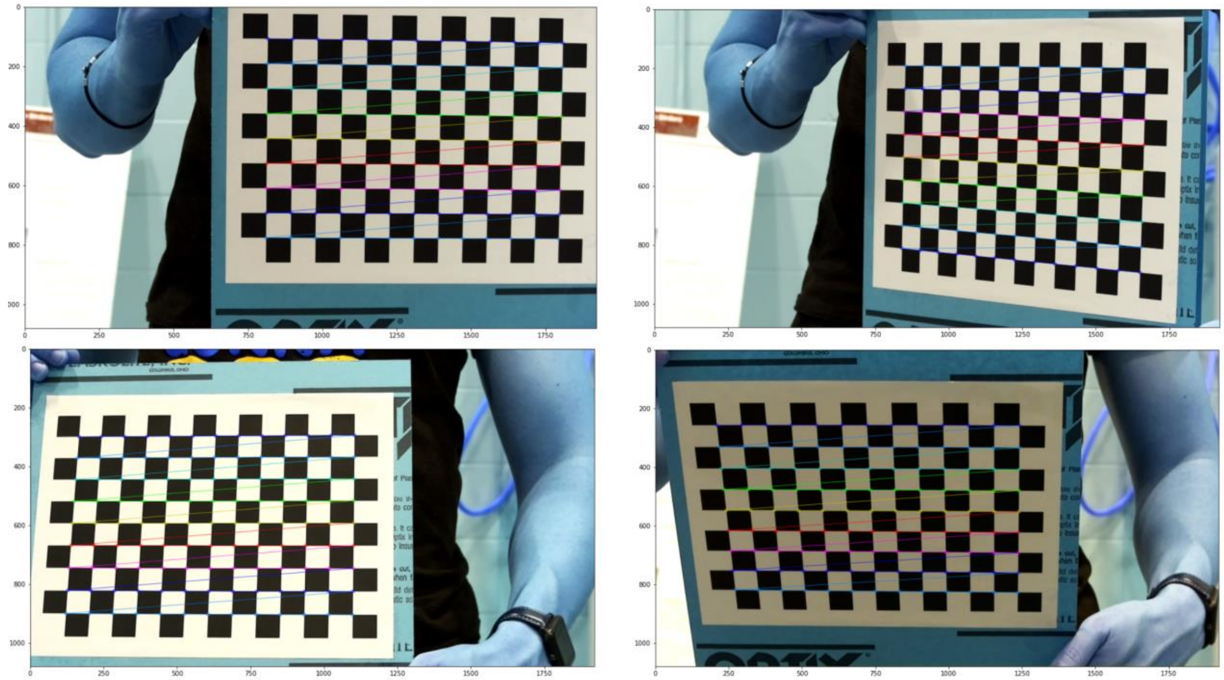

Figure 3.8. Sample Frames Used in Camera Calibration Process in OpenCV

Several images were taken at different locations and orientations to cover the camera FOV. The colored lines represent the checkerboard pattern that is retrieved by the software.

When the camera calibration process is complete, reprojection errors are calculated to evaluate the accuracy of the estimated parameters. The reprojection error measures the distance between the projected 2D point of a 3D point and its corresponding detected 2D feature point. The closer the re-projection error is to zero, the more accurate the parameters are. The arithmetical mean of the errors is calculated for all the calibration images as the average error.

3.4.2 DIC Marker-based Displacement Measurement Technique

As discussed in the previous section, the camera calibration provides camera parameters, specifically the camera matrix and distortion coefficients. Given the camera parameters and an image containing ArUco markers, the detection process returns a list of detected markers by using a built-in OpenCV function (OpenCV, 2022a). Each detected marker includes the position of its four corners in the image (in their original order), and the marker ID. In the marker detection process of this project, an option to refine the corner locations with subpixel accuracy was activated in OpenCV. **Figure 3.9** shows an example of detected ArUco markers attached to a bridge column tested at the Lohr structural laboratory at South Dakota State University (SDSU).

Figure 3.9. Sample of ArUco Marker Detection

When a marker is detected, the camera pose with respect to the marker can be computed as a 3D transformation from the marker coordinate system to the camera coordinate system. A built-in OpenCV function is used for the camera pose estimation, knowing the four corners of the detected ArUco marker, its dimension, and the camera calibration parameters. The function returns the markers' pose estimation with respect to the camera individually. For each marker, rotation and translation vectors are returned. The returned transformation is the one that transforms points from each marker coordinate system to the camera coordinate system. The marker coordinate system is centered in the middle of the marker, with the Z-axis perpendicular to the marker plane. Then, the rotation vector is converted to a rotation matrix. By knowing the rotation matrix, *R*, and the translation vector, *t*, the displacement of the ArUco marker between two consecutive frames can be retrieved. For a single marker appearing in two frames, the displacement *d* can be computed as:

$$d = R_1^T(t_2 - t_1) \qquad \text{(Eq. 3.5)}$$

where, R_1^T is the transpose of the rotation matrix at frame 1, and t_1 and t_2 are respectively the translation vector at frames 1 and 2.

For a cluster of markers, the rotation matrix of the cluster was calculated by extracting the four corners of the cluster of markers. A sample of corner identification is shown in **Fig. 3.10** in which the four corners are marked with red dots. Subsequently, the cluster rotation matrix, R_c, was retrieved using the camera calibration parameters, the cluster dimensions, and the cluster's corners, all as the inputs of the OpenCV built-in function for the pose estimation. Using information of two frames, the displacement *d* was computed as:

$$d = R_{c1}^T(\bar{t}_2 - \bar{t}_1) \qquad \text{(Eq. 3.6)}$$

where, R_{c1}^T is the transpose of the cluster rotation matrix at frame 1, and $\bar{t}_1$ and $\bar{t}_2$ are the mean translation vectors of all the single markers in the cluster at frames 1 and 2.

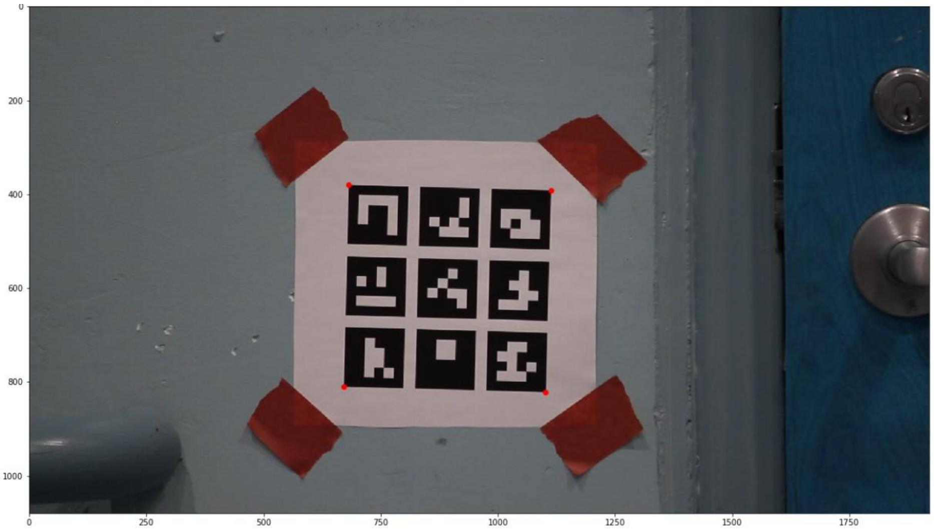

Figure 3.10. Four Corners of a Cluster of ArUco Markers Shown with Red Dots

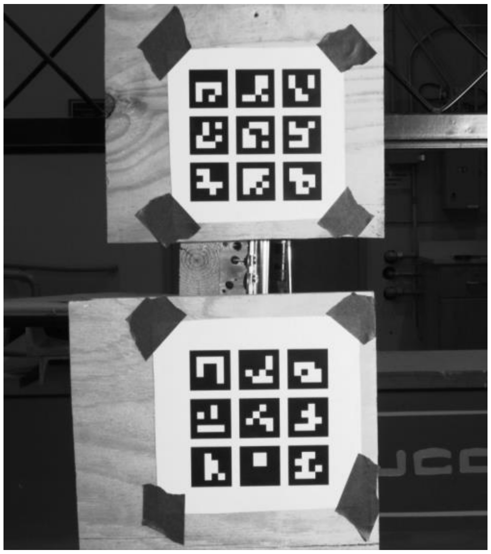

Figure 3.11. Sample of Two Clusters of Markers, one Reference (bottom) and one Target (top)

As will be discussed later in **Ch. 4**, two markers, one as the reference marker and another as the target, will be incorporated in some tests. Specifically, they comprise two individual markers, or two clusters of markers (**Fig. 3.11**). The reference marker is steady during the test, whereas the target marker is attached to the surface of interest for measuring structural displacements. For the two-individual markers case, the displacement of the target marker with respect to the reference marker (d_{tr}) can be computed as:

$$\begin{gathered} d_{tr} = R_{r_i}^{T}\left(b_{t_i} - b_{r_i}\right) \\ b_{r_i} = \left(t_{r_i} - t_{r_o}\right) \\ b_{t_i} = \left(t_{t_i} - t_{t_o}\right) \\ with\ \ i = 1, \dots, n_{frames} \end{gathered} \qquad \text{(Eq. 3.7)}$$

where, $t_{t_o}$and t_{r_o} are the translation vectors of the target and reference markers at the initial frame, respectively, t_{t_i} and t_{r_i} are the translation vectors of the target and reference markers at the subsequent frames, and $R_{r_i}^T$ is the transpose of the rotation matrix of the reference marker at the i^{th} frame. The rotation matrix is used to project the target marker into the reference marker frame to find the displacement of the target with respect to the reference. In addition, for practical purposes, it must be noted that $t_{t_o}$and $t_{r_o}$are usually the mean value of the first *n* initial frames. In this way, it is possible to reduce the noise and uncertainties of the measurements (i.e., spikes in the retrieved measurements) when there is no motion in the markers, thus a stable value of the displacement close to zero can be obtained at the initial frames.

In a similar manner, for the two-clusters of markers cases, the displacement, d_{tr} of the target marker with respect to the reference marker can be computed as:

$$\begin{gathered} d_{tr} = R_{r_i}^T\left(b_{t_i} - b_{r_i}\right) \\ b_{r_i} = \left(\bar{t}_{r_i} - \bar{t}_{r_o}\right) \\ b_{t_i} = \left(\bar{t}_{t_i} - \bar{t}_{t_o}\right) \\ with\ i = 1, \ldots, n_{frames} \end{gathered} \qquad \text{(Eq. 3.8)}$$

where, $\bar{t}_{t_o}$and $\bar{t}_{r_o}$ are respectively the mean translation vectors of all the single markers within the target marker cluster and the reference marker cluster at the initial frame, $\bar{t}_{t_i}$ and $\bar{t}_{r_i}$ are the mean translation vectors of all the single markers within the target and reference marker clusters in the subsequent frames, and $R_{r_i}^T$ is the transpose of the rotation matrix of the reference marker cluster at the i^{th} frame.

3.5 DIC-Drone Hardware

In this section, drone specifications and payload are described in detail.

3.5.1 Drones

A UAV is characterized by several subsystems and specific features. The main UAV subsystems consist of a frame, propellers, motors, batteries, a flight controller module, and a payload. The frame is the main structural element of a UAV serving as the main support for other elements. The propeller converts rotational motions into thrusts and reaction torques. Aircraft propellers are characterized by the size, pitch, number of blades, and type of material. Carbon fiber propellers are more expensive than plastic ones and provide better performance. They are more rigid and thus produce less vibration when spinning. In addition, they are lighter. Plastic propellers instead are more durable as they are pliable. Regarding the motors, usually brushless DC (BLDC) motors are adopted, because of their reliability, easy control, and efficient power transmission. A crucial element related to brushless motors is the electronic speed controller (ESC), which controls the rotation frequency of the motors. ESCs are typically rated according to the maximum current. They support NiMH, LiPo, and LFP batteries with a range of input voltages. The rotation frequency is controlled using pulse width modulation (PWM). PWM is provided by the autopilot control board. The payload is the object which is being carried by the drone. In the present project, it is mainly composed of a set of cameras, a mini-pc, and batteries. **Table 3.1** presents a list of battery powered commercial UAVs including their characteristics and specifications, such as dimension, weight, payload capacity, wind resistance, flight speed, altitude, and flight time.

Table 3.1. List of Commercial UAV Systems

Drone	Payload (kg)	Flight speed (mph)	Endurance (min)	Flight altitude (m)	Wind resistance (mph)	Weight (kg)
Aertos 120	0	-	10	-	-	2.72
Albris	0	27	14-22	-	22	1.8
Alta 6	6.8	-	10-45	-	-	13.6
Alta 8	9.1	-	8-35	-	-	18.1
Anafi	0	15	25	4500	31	0.32
Aibotix A6 V2	2	18	30	1000	Yes	3.4
Autel Robotics X-Star Premium	0.18	35	25	2000	-	1.6
Blade Chroma	0.2	-	30	400	-	1.3
DJI Inspire 1	1.7	49	18	2000	22	3.06
DJI Inspire 2	0.81	58	23-27	-	22	4.25
DJI Inspire 3	0.31	58	27	3800-7000	22	4.31
DJI Matrice 100	1.13	38	22-40	5000	22	2.43
DJI Matrice 210	2.3 | 1.57	51	13-38	-	22	3.8 | 4.6
DJI Mavic 3	0	47	46	6000	27	0.9
DJI Mavic Pro	0	40	27	5000	22	0.734
DJI Phantom 3	0.5	35	25	6000	-	1.216
DJI Phantom 4	0.5	44	28	6000	22	1.38
Draganflyer X4-ES	0.8	31	15	2438	-	1.675
Draganflyer X4-C	0.335	31	15	2438	-	0.835
Draganflyer X4-P	0.8	31	15	2438	-	1.67
Draganflyer X6	0.335	31	15	2438	-	1.31
Draganflyer Guardian	0.42	31	15	2438	-	1.05
McNair/TIGHITCO	11.8	-	15-45	-	-	-
MD4-200	0.2	18	30	1000	-	1.1
MD4-1000	1.2	27	88	4000	-	2.65
MD4-3000	3	36	45	1000	-	10.4
SenseFly Albis	-	27	22	2000	22	1.8
Skycamusa	-	-	10	1000	10	-
Skydio 2+	0	36	27	4500	25	0.8
SteadiDrone QU4D X	8	-	60	-	Strong winds	3.58
SteadiDrone QU4D	0.8	-	60	-	Strong winds	1.5
SteadiDrone MAVRIK	2	-	18	-	Strong winds	1.2
Trimble UX5	-	50	50	2500	40	2.5
Trimble X100	-	50	45	2500	40	2.2
Walkera Voyager 3	0.32	49	25	1000	-	3
Yuneec Typhoon 4K	0.6	-	25	800	-	1.7
Yuneec Typhoon H	0.6	22	22	122	Yes	1.8
Yuneec Typhoon H Plus	-	30	28	500	Yes	2.09

In the present project, the UAV system that was built in-house consisted of a Tarot FY690S Full 6 axis Carbon Fiber frame 3K Folding hexacopter (**Fig. 3.12a**), six Tarot high power BLDC motors with carbon propellers (**Fig. 3.12b**), a Cube Orange Standard Set, with H7 Processor and ADS-B Carrier Board (**Fig. 3.12c**), Flycolor 40A ESC, and daier ESC power distribution board, a Pixhawk 2.1 Power Module, a Cubepilot Here 3, and a high precision Global navigation satellite system (GNSS). In addition, a Herelink HD Video Transmission System (**Fig. 3.12d**) was used as an integrated remote controller, ground station, and wireless digital transmission system. It allowed remote control, HD video, and telemetry data to be transmitted up to 12.4 miles (20 km) between the ground station and the air unit. The hexacopter had a final total weight of 4.1 kg, allowing a maximum payload of 2 kg, and a maximum flight time of 18 min, with a 5000 mAh battery (**Fig. 3.13**).

(a) Tarot FY690S Full 6-axis Carbon Fiber Frame 3K Folding exacopter

(b) Tarot High Power BLDC Motors with carbon Propellers

(c) Cube Orange Standard Set

(d) Herelink HD Video Transmission System

Figure 3.12. Drone Components Built in Present Project

Figure 3.13. UAV Built in Present Project with Off-the-shelf Hardware

3.5.2 Camera system

An experimental study was conducted to determine the best camera option(s) for use in DIC-drone applications. The trade-off in selecting the camera system was based on the following criteria:

- Weight
- Image sensors: complementary metal oxide semiconductor (CMOS) versus charge-coupled device (CCD). CMOS allows higher frame rates, is cheaper, and its quality and capabilities are now similar to CCD. In addition, CMOS sensors have a smaller size and lower power consumption than CCD sensors (Holst and Lomheim, 2011).
- Pixel size: large pixel results in a higher dynamic range and signal-to-noise ratio, but lower spatial resolution with respect to a small pixel size.
- High lens focal length means low FOV, and vice versa.
- Maximum lens focal length depends on the type of lens mount.
- Depending on the marker size and its distance from the camera, high lens focal length (e.g., ≥ 50 mm) or small camera pixel size (or both) may be required.
- A camera that supports different lenses and lens focal lengths might be necessary.
- A minimum frame rate of 20 fps.
- A camera characterized by both high resolution and high frame rate is more expensive than a camera that has only one of the two features.

Four cameras were included in the evaluation study: an Intel RealSense D435i, a Canon EOS 7D, a Blackfly S USB3, and a GoPro HERO4. **Table 3.2** presents the specifications of these cameras.

Table 3.2 Cameras Used in Evaluation Study

Camera	**Shooting Mode**	**Resolution**	**Pixel Size (μm)**	**Frame per Second (FPS)**	**Focal Length (mm)**
INTEL d435i	Photo	1920 × 1080	3.0 × 3.0	N.A.	26
CANON EOS 7D	Photo	5184 × 3456	4.305 × 4.305	N.A.	250
Blackfly S USB 3	Video	2448 × 2048	3.45 × 3.45	24	16
GoPro HERO4	Narrow Video	1920 × 1080	9.4 × 9.4	30	27

The experimental evaluation study included two test methods. The first test involved taking multiple pictures of a steady marker and extracting the position of the marker from the images to assess the noise and uncertainty level of a still image. As reported in **Table 3.3**, single and clusters of markers with different sizes and distances between the camera and its marker system were varied to obtain an equivalent marker/image fill factor. In these tests, the orientation between the camera and the marker was not changed. Between 11 to 13 pictures were taken per test, then the mean position of the center of the marker and the maximum error range were computed. The plane *x*-*y* was the image plane, whereas the *z* axis was in the direction of the camera to the marker. These tests showed that the use of a cluster of markers reduced the mean error (**Table 3.3**). Note that the highest uncertainty was in the *z* direction due to the nature of projection. This was expected since these kinds of algorithms are more accurate on the *x*-*y* plane.

Table 3.3. Camera Performance in Multi-Pictures Steady Marker Tests

Camera	Marker Type	Size of Marker or Cluster [mm]	Distance Camera-Marker & Orientation [mm, deg]	No. of Pictures Taken	Max Error Range: (x,y,z_{max} - x,y,z_{min}) [mm]	Mean Error [mm]
INTEL d435i	Single	50	~ 500, ~ 0°	11	[0.70729499, 0.32629607, 1.87060171]	[0.10364237, 0.08041678, 0.24473287]
INTEL d435i	Single	100	~ 500, ~ 0°	11	[0.38325395, 0.1435364, 1.34576703]	[0.06238352, 0.01996761, 0.23484935]
INTEL d435i	Cluster of 4	53.5	~ 500, ~ 0°	11	[0.34768867, 0.27331899, 1.06840426]	[0.08506479, 0.07904892, 0.23483284]
INTEL d435i	Cluster of 9	53.5	~ 500, ~ 0°	11	[0.29006421, 0.0853771, 0.62307165]	[0.06358246, 0.01925977, 0.12188215]
CANON EOS 7D	Single	50	~ 4000, ~ 0°	11	[0.14134592, 0.16649806, 9.17299842]	[0.02679793 0.04099162 1.84633134]
CANON EOS 7D	Single	100	~ 4000, ~ 0°	11	[0.08419858, 0.1156979, 7.43055069]	[0.02404497, 0.03428245, 2.35331069]
CANON EOS 7D	Cluster of 4	53.5	~ 4000, ~ 0°	13	[0.13862035, 0.2363077, 7.04230433]	[0.02976877, 0.05741215, 1.83004584]
CANON EOS 7D	Cluster of 9	53.5	~ 4000, ~ 0°	13	[0.09948255, 0.09204869, 4.35900761]	[0.0202815, 0.02515111, 0.95365478]
BlackFly S USB 3	Single	50	~ 1000, ~ 0°	11	[0.04263552, 0.01296088, 0.09334041]	[0.02114158, 0.00642688, 0.0462845]
BlackFly S USB 3	Single	100	~ 1000, ~ 0°	11	[0.08118058, 0.21256184, 0.94471688]	[0.01156839, 0.03531521, 0.28035114]
BlackFly S USB 3	Cluster of 4	53.5	~ 1000, ~ 0°	11	[0.08730189, 0.1005179, 1.4607653]	[0.02003177, 0.02696268, 0.38739014]
BlackFly S USB 3	Cluster of 9	53.5	~ 1000, ~ 0°	11	[0.17941115, 0.1999079, 1.98008717]	[0.06792838, 0.06746458, 0.70058971]
GoPro HERO4	Single	50	~ 725, ~ 0°	12	[0.9109068, 2.4222313, 16.80418196]	[0.12680235, 0.37270901, 2.49031638]
GoPro HERO4	Single	100	~ 725, ~ 0°	12	[0.50114097, 0.54649299, 6.67234439]	[0.09570662, 0.08345835, 1.15264032]
GoPro HERO4	Cluster of 4	53.5	~ 725, ~ 0°	12	[0.44115575, 0.48099492, 8.21845413]	[0.11689049, 0.12799922, 2.293381]
GoPro HERO4	Cluster of 9	53.5	~ 725, ~ 0°	12	[0.21330474, 0.23576169, 2.5881666]	[0.04342314, 0.0444306, 0.62923192]

The second series of the camera evaluation tests were focused on the measurement of the vertical (*y* direction) displacement of a marker in which the marker was manually displaced by 10.3666 mm (**Fig. 3.14**). At the beginning of each test, the marker was placed on the top of a spacer with a depth of 10.3666 mm, which was measured using a caliper. Subsequently, the spacer was removed. Pictures were taken with different cameras before and after removing the spacer. Note that the camera was fixed.

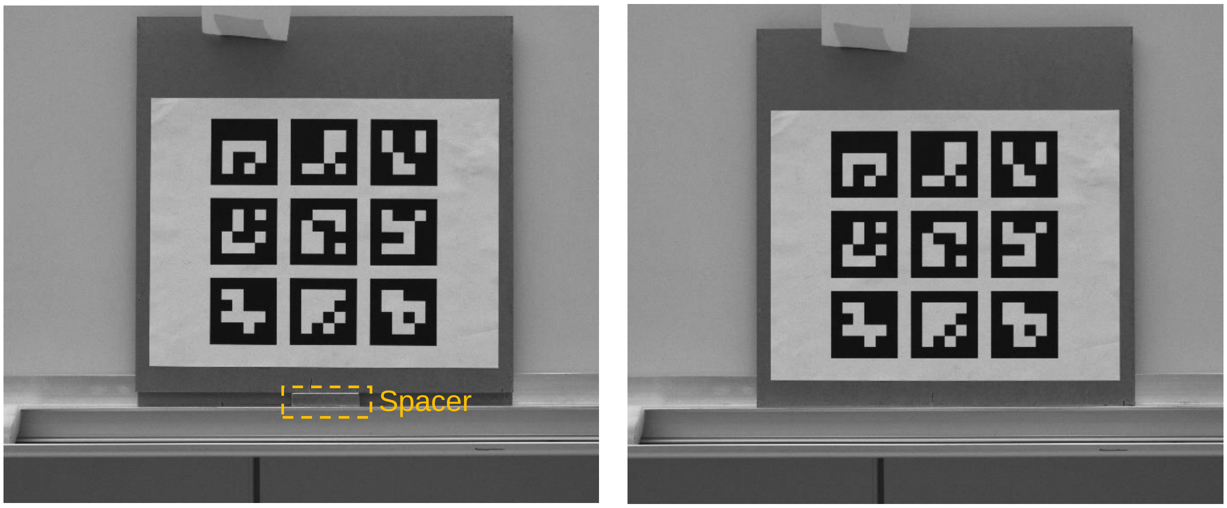

(a) Maker on Spacer (b) Maker when Spacer Removed

Figure 3.14. Displacing Markers to a Known Position

Blackfly Camera, cluster of 9 markers at 1000 mm distance and 0° orientation

Using these two pictures or frames, the displacement in the *y*-direction using the DIC methods described in the previous section was estimated. This process was repeated six times and the mean percentage error, and the maximum percentage error of the measurement were computed.

A summary of the test results for all cameras is presented in **Table 3.4**. Furthermore, **Fig. 3.15** is a graphical representation of the table specifically the mean percentage error and its equivalent physical value. It can be seen that the least mean percentage errors were usually achieved when a cluster of markers was used, specifically the cluster of 9 markers. Since the cluster of 16 markers had the same overall size as the cluster of 9 markers, their constitutive markers were smaller in the 16-marker case. This reduced the software's accuracy in detecting and extracting markers' positions at the pixel level. In addition, the use of a cluster increased the accuracy of the displacement measurements by merging results from multiple markers at the same time. Another finding was that an increase in the orientation between camera and marker always adversely affected the displacement measurements. Parallel measurements (i.e., 0°) are recommended.

Based on these evaluation tests, Blackfly S camera was selected for further investigations (**Ch. 4**) due to its high accuracy and cost effectiveness.

Table 3.4. Camera Performance in Known Displaced Marker Tests

Camera	Marker Type	Size of Marker or Cluster [mm]	Distance Camera-Marker & Orientation [mm, deg]	No. of Pictures Taken	ArUco, Mean Percentage Error [%]	ArUco, Max Percentage Error [%]
INTEL d435i	Single	50	~ 500, ~ 0°	12	3.68	4.41
INTEL d435i	Single	100	~ 500, ~ 0°	12	1.32	-2.89
INTEL d435i	Cluster of 4	53.5	~ 500, ~ 0°	12	2.11	3.27
INTEL d435i	Cluster of 9	53.5	~ 500, ~ 0°	12	1.50	1.84
CANON EOS 7D	Single	50	~ 4000, ~ 0°	12	2.18	5.20
CANON EOS 7D	Single	100	~ 4000, ~ 0°	12	2.82	-5.66
CANON EOS 7D	Cluster of 4	53.5	~ 4000, ~ 0°	12	2.76	4.13
CANON EOS 7D	Cluster of 9	53.5	~ 4000, ~ 0°	12	0.77	1.72
BlackFly S USB 3	Single	50	~ 1000, ~ 0°	12	1.74	4.02
BlackFly S USB 3	Single	100	~ 1000, ~ 0°	12	0.58	1.59
BlackFly S USB 3	Cluster of 4	53.5	~ 1000, ~ 0°	12	0.81	-1.07
BlackFly S USB 3	Cluster of 9	53.5	~ 1000, ~ 0°	12	0.30	0.83
BlackFly S USB 3	Single	100	~ 725, ~ 45°	12	7.55	-9.51
BlackFly S USB 3	Cluster of 9	53.5	~ 725, ~ 45°	12	3.66	5.23
BlackFly S USB 3	Cluster of 16	25.5	~ 725, ~ 45°	12	9.26	-15.47
GoPro HERO4	Single	50	~ 725, ~ 0°	12	3.07	12.06
GoPro HERO4	Single	100	~ 725, ~ 0°	12	0.57	0.56
GoPro HERO4	Cluster of 4	53.5	~ 725, ~ 0°	12	1.14	2.04
GoPro HERO4	Cluster of 9	53.5	~ 725, ~ 0°	12	0.62	-0.50
GoPro HERO4	Cluster of 9	34.5	~ 725, ~ 0°	12	0.87	-2.89
GoPro HERO4	Cluster of 16	25.5	~ 725, ~ 0°	12	0.33	-0.82
GoPro HERO4	Single	50	~ 725, ~ 45°	12	40.52	59.96
GoPro HERO4	Single	100	~ 725, ~ 45°	12	3.53	-6.76
GoPro HERO4	Cluster of 4	53.5	~ 725, ~ 45°	12	9.33	26.08
GoPro HERO4	Cluster of 9	53.5	~ 725, ~ 45°	12	4.94	-10.94
GoPro HERO4	Single	50	~ 725, ~ 45°	12	12.97	-33.10
GoPro HERO4	Single	100	~ 725, ~ 45°	12	27.23	-55.77
GoPro HERO4	Cluster of 4	53.5	~ 725, ~ 45°	12	19.21	-61.13
GoPro HERO4	Cluster of 9	53.5	~ 725, ~ 45°	12	13.51	-24.09
GoPro HERO4	Cluster of 9	34.5	~ 725, ~ 45°	12	6.56	12.49
GoPro HERO4	Cluster of 16	25.5	~ 725, ~ 45°	12	2.51	4.38

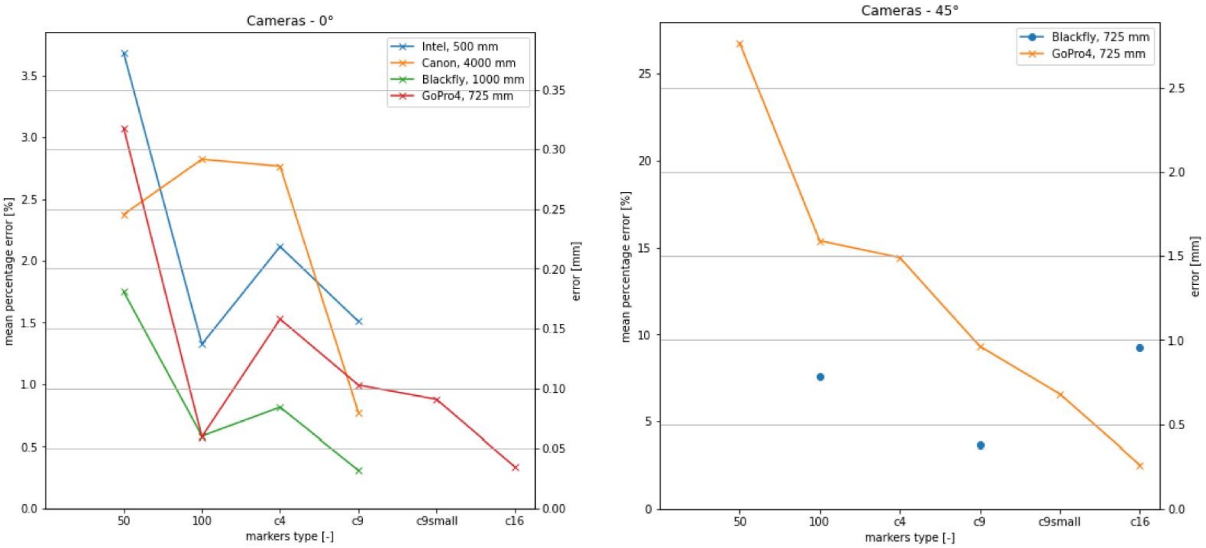

(a) Camera Sensor Parallel to Marker (b) Camera Sensor Oriented at 45° of Marker

Figure 3.15. Camera Performance in Known Displaced Marker Tests

3.5.3 Payload

The payload consisted of a carbon fiber plate placed at the bottom of the drone accommodating the battery, the mini-PC, and the camera system (**Fig. 3.16**). This configuration allowed an adequate distribution of weights, balance, and flight stability. The on-board computer was a MeLE Fanless Mini PC Quieter3Q Intel Celeron N5105 with 8GB of RAM and 500 GB of SSD storage, whereas the battery was a HRB 4S 14.8v 5000mAh 50C Lipo Battery. The camera system was composed of two Blackfly S USB3 cameras (Model: BFS-U3-51S5M-C: 5.0 MP, 75 FPS, Sony IMX250, Mono), and mounting lenses with different focal lengths. The lenses adopted were either a 16-mm (0.63-in.) focal length Kowa LM16JC5M2, or a 50-mm (1.97-in.) focal length Edmund Optics. Two USB 3.0 cables were used to power the cameras. Two Hirose HR10 (6 Pin) GPIO cables and a simple circuit were utilized to synchronize the capturing of frames. Lastly, an HDMI cable was used to stream the camera feeds to the Herelink HD Video Transmission System for real-time first person view (FPV). This was necessary to check if the markers were within the camera FOV. The total weight of this payload with the 50-mm lens was 1.58 kg.

Figure 3.16. Payload Attached to UAV Built in Present Project

CHAPTER 4. LABORATORY VERIFICATION OF DIC-DRONE BASED DISPLACEMENT MEASUREMENT TOOLS

4.1 Introduction

In this chapter, the accuracy of the proposed DIC-drone based displacement measurement tools is evaluated. Bridge specimen, test setup, instrumentations, and test methods are described first. Then, the test results are presented. All experiments were performed in the Lohr Structures Laboratory at South Dakota State University.

4.2 Experimental Program

In this section, bridge test specimen, test setup, and different testing methods are described.

4.2.1 Bridge Test Specimen

As was discussed in **Chapter 2**, both displacement and strain data can be obtained from bridge field testing. Strain measurements are more common these days since strain sensors do not need a reference point. **Table 2.1** presents a summary of the past field testing and their peak measurements. In the present study, the girder displacement was the target. Since the measured girder displacement in all past tests was less than 20 mm (0.79 in.), the target displacement in the present study was assumed to be less than 10 mm (0.4 in.) to cover different bridge types. A bridge model was selected in which it could be loaded to 10 mm (0.4 in.) without the use of hydraulic actuators or heavy equipment. The bridge model was a truss made of three parts, as shown in **Fig. 4.1**. Each part was 1.5 m (59 in.) in length and had a square cross section with a side dimension of 203 mm (8 in.). The total length of the truss bridge was 4.5 m (177 in.).

As shown in **Fig. 4.2**, the truss bridge was placed on the top of a series of concrete blocks, to reach a height that was easy to load the bridge without any equipment and to fly drones. At the bridge midspan, a piece of plywood was attached to the bridge using a bolt to secure the target DIC marker. The target in this study is the point of interest to obtain displacements. Another marker was added in some tests (e.g., Fig. **4.1c**) to serve as the reference marker. A pedestal was positioned underneath the bridge at its midspan to install displacement sensors, and the reference DIC marker.

Over the course of the study, the research team modified the location of the displacement sensors to find the most representative data as the baseline of the comparison with DIC measurements. In early tests, two sensors were placed underneath the truss bridge on its bottom front and back chords (**Fig. 4.1a**). However, the displacement of the board was slightly different than the bridge. Subsequently, one sensor was installed on the bridge and another on the plywood. Later, both displacement sensors were installed on the left and right side of the plywood to capture possible rotation of the board (**Fig. 4.1b**). After several trials and in the final stage of the study when the reference marker was used to remove the drone movements, both sensors were placed on the bridge (**Fig. 4.1c**).

Unless specified otherwise, the 117.5-mm (4.62-in.) DIC marker was a cluster of nine individual markers, each with a side dimension of 34.5 mm (1.36 in.). The proposed clustering was based on the preliminary experimental findings presented in **Chapter 3**.

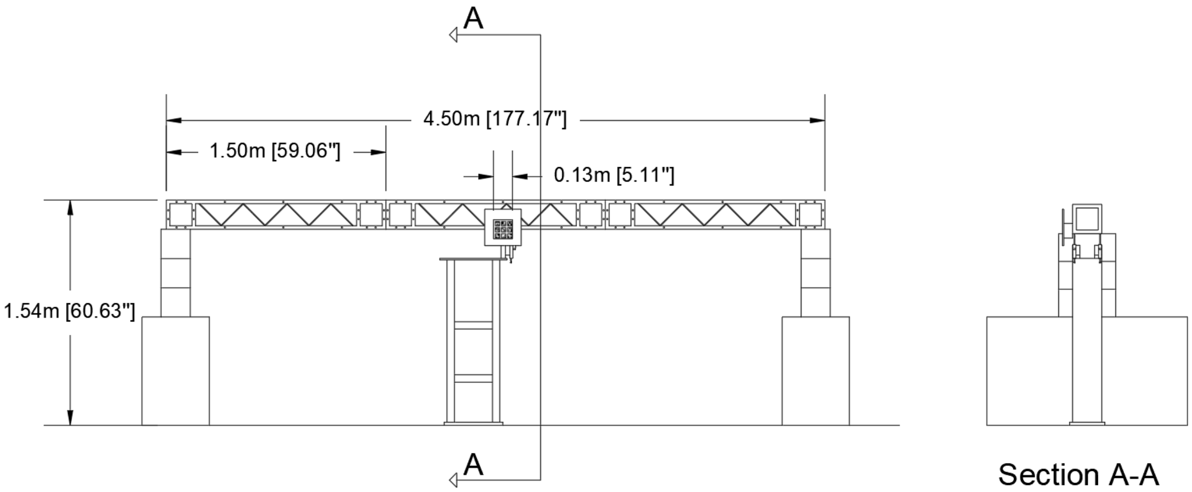

(a) One marker and Two Displacement Sensors on Front and Back Faces of Bridge

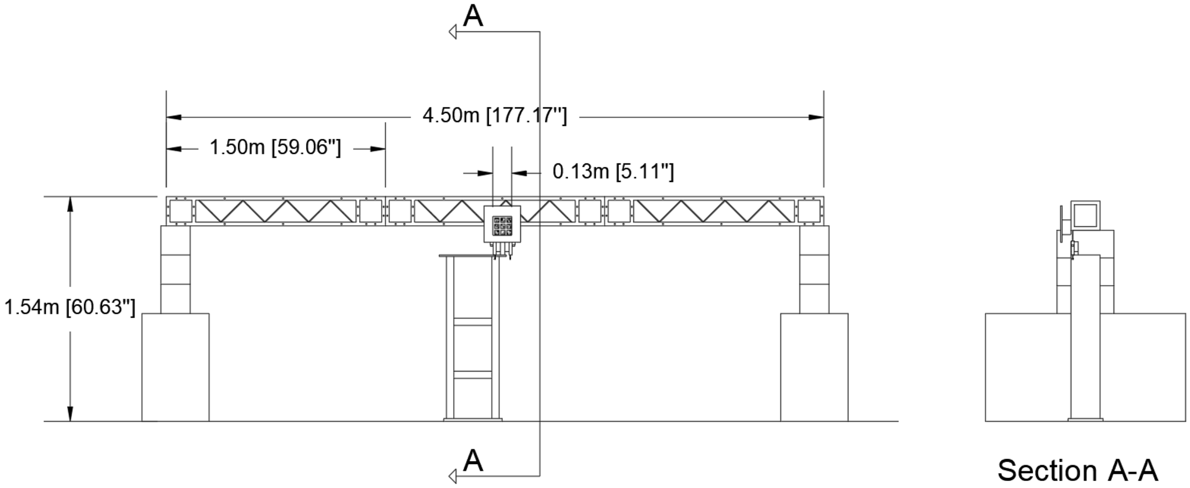

(b) One Marker and Two Displacement Sensors on Marker

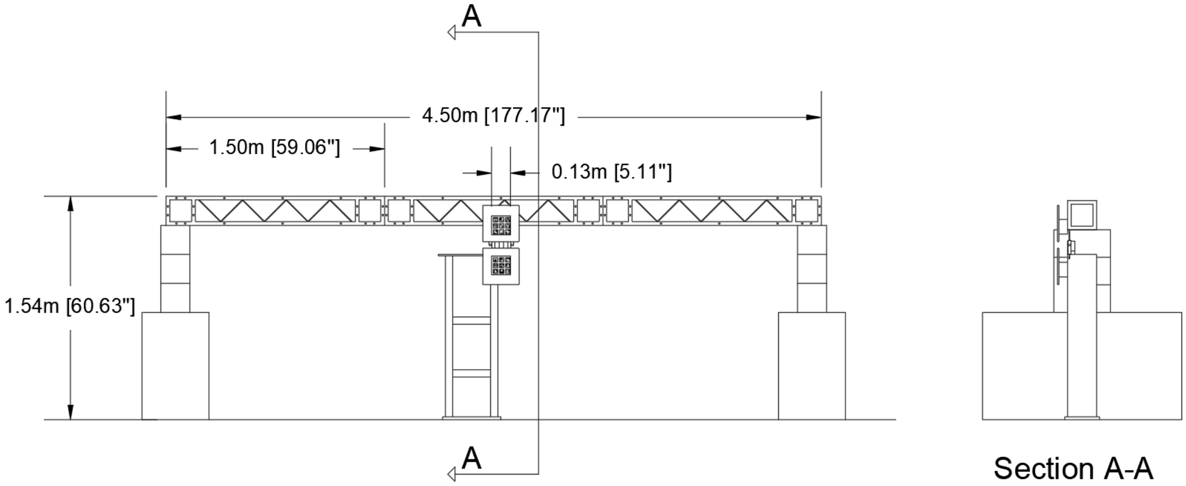

(c) Two Markers, Target (top) and Reference (bottom), and Two Displacement Sensors on Target Marker

Figure 4.1. Truss Bridge Model and Test Setup

Figure 4.2. Photograph of Truss Bridge Model and Test Setup

4.2.2 Displacement Sensors

Conventional displacement sensors were used in all experiments to measure vertical displacements of the bridge test model under different loading. Linear Variable Differential Transformers (LVDTs) Series TR / TRS by Novotechnik were used in the tests (**Fig. 4.3**). These LVDTs can measure displacements as small as 0.002 mm (0.00008 in.). The linearity error is within 0.15% for the 2-in. (51-mm) long stoke LVDTs used in the tests. The LVDT measurements were assumed as the ground truth and were used to evaluate the accuracy of the displacements measured by the DIC technique. **Figure 4.4** shows two LVDTs that were mounted on the bridge test model. One was installed on the bottom face of the bridge, and another was to measure the vertical displacement of the board holding the DIC markers. In a perfect setup, both should produce the same measurements.

Figure 4.3. Displacement Sensor Used in Experiments

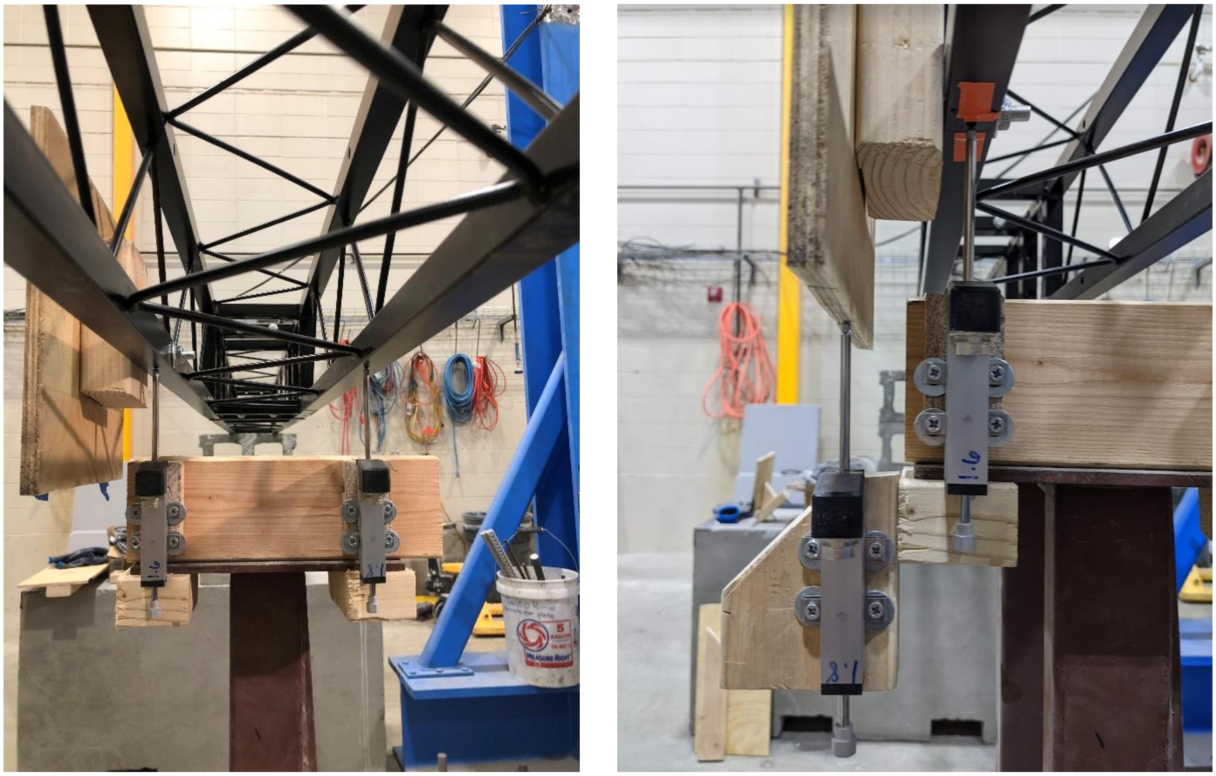

(a) LVDTs on Bridge (b) LVDTs on Bridge and Board

Figure 4.4. Instrumentation of Bridge Test Model

The LVDTs were connected to a Vishay Data Acquisition (DAQ) System, and the data was recorded using StrainSmart software. The 128-channel DAQ can record up to 2000 measurements per second. In the present study, a rate of 10 or 100 data per second was used. The 10-Hz sampling rate was sufficient for static tests, but 100 Hz was used in dynamic tests.

4.2.3 Camera Configurations for DIC Measurements

Based on the camera system trade-off and promising results reported in **Sec. 3.5.2**, Blackfly S USB3 was selected for the DIC measurement in the bridge testing. Furthermore, a Raspberry Pi HQ camera with a 16-mm (0.63-in.) telephoto lens was also utilized as a possible low-cost alternative.

The Raspberry Pi HQ camera was implemented with Raspberry Pi, a low-cost small single-board computer used in several areas of research and industry. Being extremely light weighted and characterized by a low energy consumption, the Pi camera-board system might be a viable option in drone applications.

Different configurations or combinations of cameras were used over the course of the experimental study, which were:

- Tests with a single camera in which either the Blackfly or Pi camera was used.
- Tests with two cameras but without synchronization in which a combination of the Blackfly and Pi cameras were used. In some cases, two Blackfly cameras were used.
- Tests with two synchronized cameras in which both cameras were Blackfly.

In tests with the dual camera setup (**Fig. 4.5**), in some cases the two cameras were faced toward the bridge, and in other cases one camera was monitoring the marker on the bridge and another camera was monitoring another marker in the opposite direction of the bridge camera.

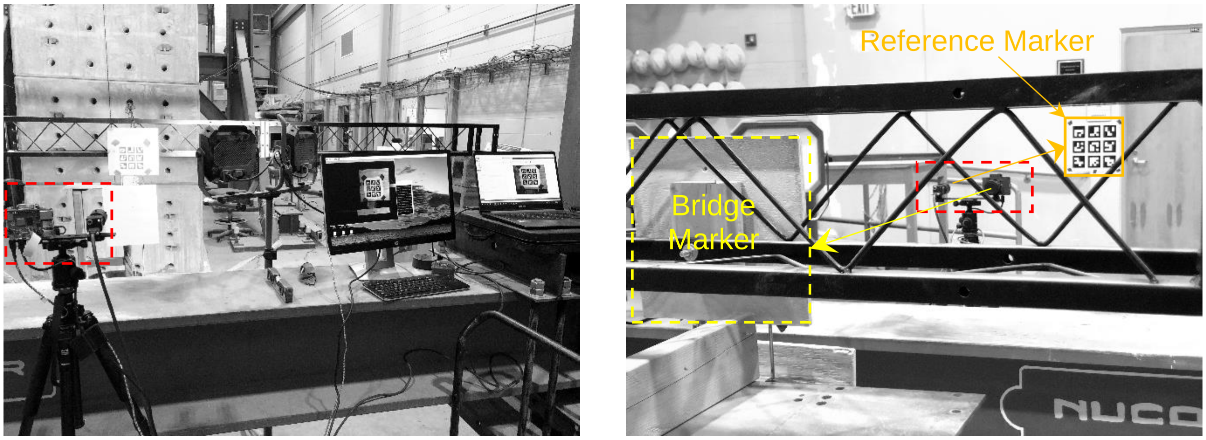

(a) Camera Faced Toward Bridge (b) Cameras Faced in Opposite Directions

Figure 4.5. Camera Orientation in Bridge Model Testing

4.2.4 Testing Methods

In bridge field testing, either static or dynamic loading can be applied to the bridge. Static tests are those in which the truck is stationary or moving very slowly. In dynamic tests, the truck moves over the bridge at the speed limit. Both types of testing were included in the experimental program of the present study. Furthermore, the camera can be grounded or can be on drones. Fixed and moving cameras should be included in the testing. The following sections describe how all these variations were included in the present study.

4.2.4.1 Static Testing

The static testing of the bridge model was performed by slowly adding weights on the top of the bridge at its midspan (**Fig. 4.6**). Steel channels were used to load the bridge. The total weight placed on the bridge in different tests was between 822 N (185 lbs.) and 1045 N (235 lbs.) to achieve a displacement less than 10 mm (0.4 in.). The truss bridge was moved in the laboratory a few times and its stiffness degraded after several tests due to loosening of its connections. Note the truss bridge was made of three parts. Therefore, to compensate for stiffness variations, there was a range of the load. Whenever the stiffness degradation was large, the bolts were retightened, and the load was adjusted to achieve the target displacement.

Figure 4.6. Static Loading Applied to Bridge Test Model

4.2.4.2 Dynamic Testing

The dynamic testing of the bridge model was performed by either suddenly releasing a heavy bucket, which was attached to the bridge, or pulling down the bridge manually. **Figure 4.7** shows the dynamic setup.

Figure 4.7. Dynamic Loading of Bridge Test Model

4.2.4.3 Bridge Testing with Moving Cameras

Prior to the incorporation of the proposed DIC system on drones, it was desired to mimic the drone movements in a controlled setup and to further fine tune the DIC measurements. To achieve this goal, the research team implemented two techniques. In the first method, the camera system was secured on the top of a moving cart (**Fig. 4.8a**), which was then manually displaced 50 to 100 mm (2 to 4 in.) back and forth.

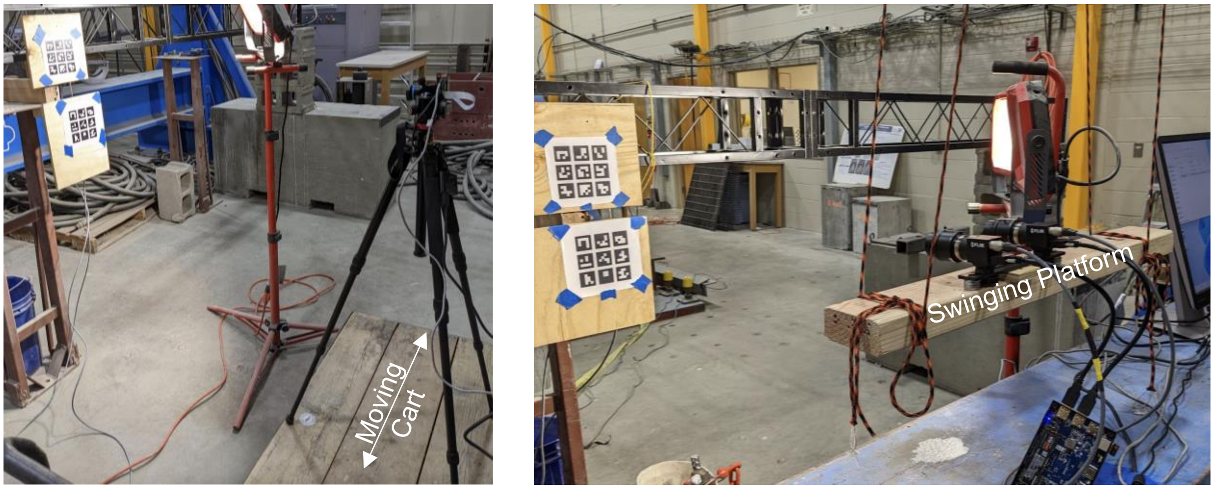

(a) Moving Cart (b) Oscillating Platform Hanged from a Frame

Figure 4.8. Bridge Testing with Moving Cameras

In the second method, we built an oscillating platform on the top of which the camera system was secured to simulate a more realistic drone movement (**Fig. 4.8b**). In this case, the movement was obtained by gently tapping the wood platform.

4.2.4.4 Bridge Testing with Drone Mount Cameras

As discussed in **Chapter 3**, we built a drone system in-house, which can carry two cameras and a mini-PC for data processing. Due to time limitations, we were not able to successfully use this drone inside the laboratory due to weak GPS signals. The GPS mounted on the drone allows the drone to enter a stable controlled flight and reduce hovering oscillations. This is especially important when a drone is watching a DIC marker. We have tried to fly the drone indoor without the use of GPS, in manual mode, but the pilot had difficulties to maintain the drone stable enough to see the marker throughout the flight. For these issues, the proposed DIC system was mounted on a different drone, a DJI MATRICE 210 V2 (**Fig. 4.9**). This drone has a maximum flight time of 38 min, a maximum payload of 2.34 kg (5.15 lbs.), a wind resistance of 12 m/s (26.8 mph) and can operate in -20 °C to 45 °C (-4 °F to 113 °F).

After a few test flights, we found that this DJI drone can fly both outdoors and indoors. Subsequently, the DIC system was mounted to this drone (**Fig. 4.10**) then a few tests were performed indoors to validate the DIC measurement.

Figure 4.9. DJI MATRICE 210 V2 Used for Indoor Testing

Figure 4.10. DJI Drone with DIC Payload and Field of View of Cameras

4.3 Experimental Results

In this section, a summary of 70 experiments is presented. As mentioned earlier, four testing methods were exercised. In the early tests, the feasibility of retrieving the vertical displacement of the truss bridge was explored by extracting data from only one marker attached to the bridge (referred to as the target marker) using a single fixed (or ground) camera looking at the bridge. Based on the findings of these experiments and since the ultimate goal of the project was to mount the camera system on a drone, a reference marker attached to a stationary point was included. This allowed the measurement of the vertical displacement of the bridge with respect to the reference marker using only one camera, and consequently to counteract the motion of the drone that otherwise would be unknown. Then, since the marker/image fill factor influenced the results, as mentioned in **Chapter 3**, one camera was not sufficient to include both target and reference markers in its FOV. Therefore, two cameras were utilized to improve the measurements in a more realistic manner. In the last rounds of testing, two cameras were mounted on a drone.

In a few dual-camera experiments, a combination of the Blackfly S USB3 with 16-mm (0.63-in.) or 50-mm (1.97-in.) focal length lenses and the Raspberry Pi HQ camera with a 16-mm (0.63-in.) telephoto lens were used. Nevertheless, these two different cameras could not be synchronized. Subsequently, we used two Blackfly cameras with in-house programming to resolve the synchronization issues. Finally, we have mounted the dual Blackfly camera system on the drone to investigate the feasibility of the proposed DIC-drone measurement technique. The following sections summarize the key results of different tests.

4.3.1 Single Ground Camera Tracking Target Marker in Static Tests

In this series of testing, bridge vertical displacements were retrieved by using a single camera, a Raspberry Pi HQ camera equipped with a 16-mm (0.63-in.) telephoto lens, and a single ArUco marker as the target, which was attached to the truss bridge (e.g., **Fig. 4.1a**). The bridge was tested statically. For static tests discussed herein, the camera was approximately 1.27 m (50 in.) away from the truss bridge. In the first round of static testing on the truss bridge, the effects of the camera resolution, ISO (International Standards Organization, defined as the sensitivity of the camera sensor), aperture, and marker-camera distance were investigated. After a few trials, a resolution of 1920×1080, a shutter speed between 0.01 and 0.05 sec, the lowest ISO value of the Pi camera, and an aperture value between f/stops 4-7 depending on the illumination, were selected for further investigation. These settings allowed to reach a frame rate of 30 fps, which is sufficient in bridge dynamic tests. Past studies (e.g., Ngeljaratan and Moustafa, 2020) confirmed the suitability of this frame rate when a bridge was tested on a shake table.

Figure 4.11 compares the measured vertical displacement of the bridge following a static testing discussed in **Sec. 4.2.4.1** using both the DIC method and LVDTs as the ground truth. Included in these and following figures are error margins based on the LVDT response. For example, a legend with "LVDT 1%" indicates errors with a 1% margin. Three cases were analyzed, based on the relative inclination of the target marker with respect to the camera. The relative inclinations were 0°, 22°, and 45° (**Fig. 4.12**). These tests were to investigate how the DIC calculated measurements change when the camera sensor and the marker were not parallel. This is an important factor in an actual bridge field testing to approximate the tolerance for turbulence when the drone is monitoring a target. The graphs show that as the relative inclination increases the accuracy of the DIC calculated displacement decreases. At the 0°-relative inclination, the displacement error between the DIC marker and LVDTs at the peak load was less than 1%, whereas the error reached 3% for the 45° inclination. Note 1% error was equivalent to 0.08 mm (0.003 in.) of displacement. Furthermore, the DIC displacements were noisier at higher relative inclinations, due to mathematical limitations of equations built-in with OpenCV. Overall, these testing showed that a turbulence causing up to 45° inclination between the camera and marker during a drone flight is acceptable as they result in up to 3% error in displacement measurements.

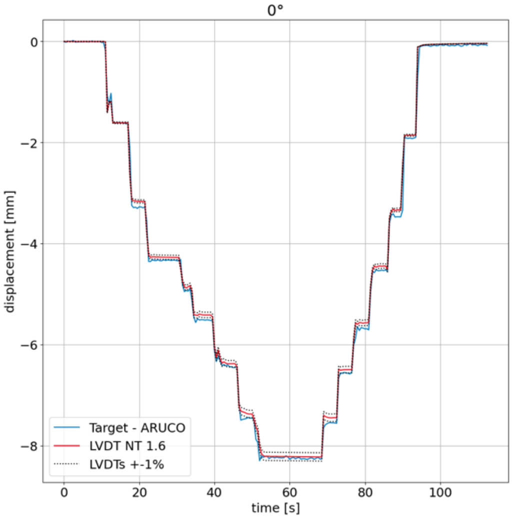

(a) 0° Relative Inclination; 1% error at the peak load was equal to 0.08 mm (0.003 in.)

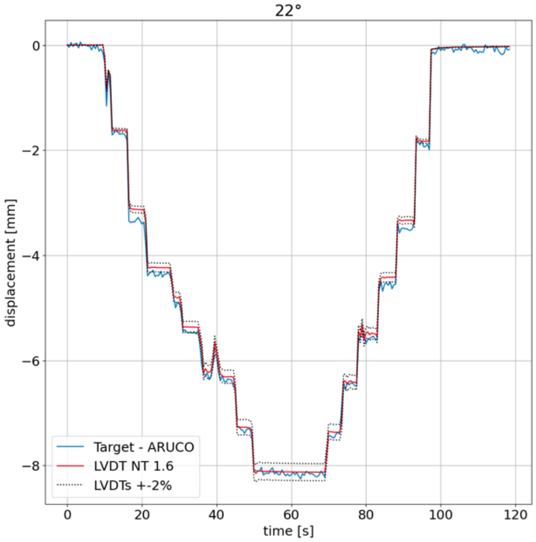

(b) 22° Relative Inclination; 2% error at the peak load was equal to 0.16 mm (0.006 in.)

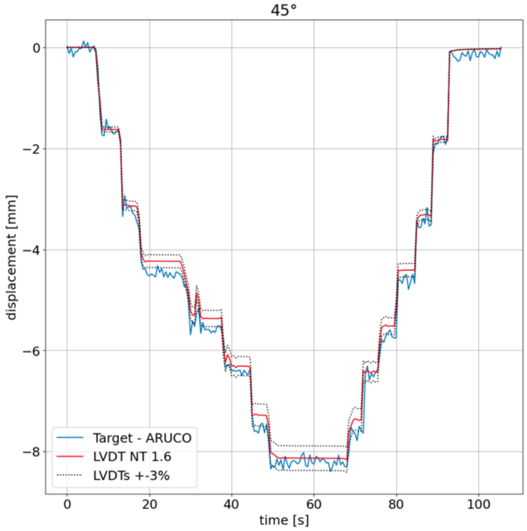

(c) 45° Relative Inclination; 3% error at the peak load was equal to 0.24 mm (0.009 in.)

Figure 4.11. Static Test Results with Different Relative Inclinations between Camera and Marker

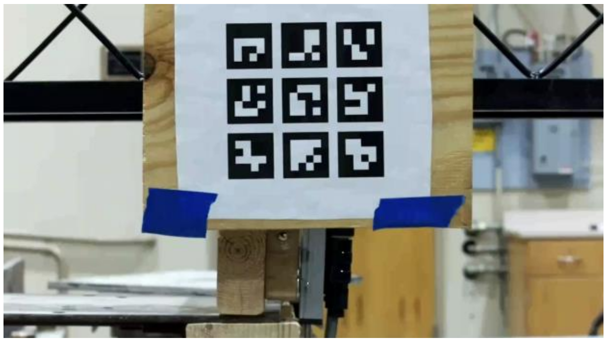

(a) 0° Relative Inclination

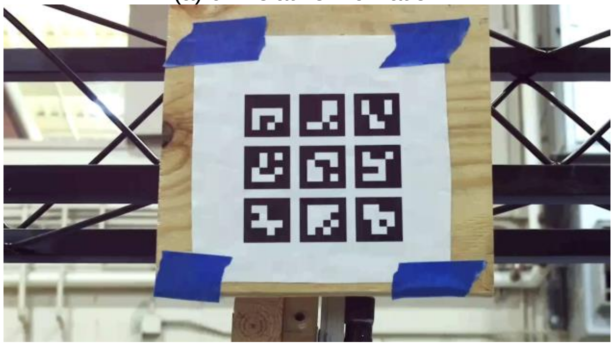

(b) 22° Relative Inclination

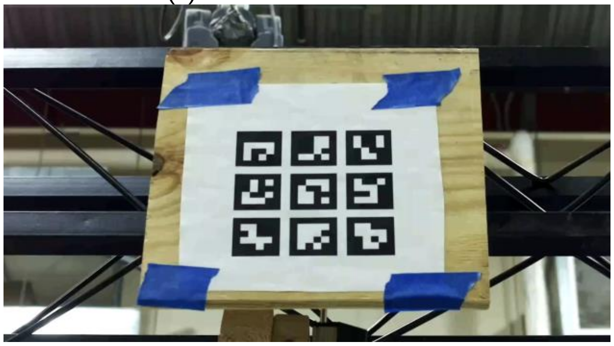

(c) 45° Relative Inclination

Figure 4.12. Raspberry Pi HQ Camera Frames at Different Relative Inclinations

4.3.2 Single Ground or Moving Camera Tracking Two Markers

The experimental results of a single camera, a Blackfly S USB3 or a Raspberry Pi HQ camera, with two ArUco markers, the target and reference markers, are presented herein. The target marker was attached to the truss bridge, whereas the reference marker was placed on a pedestal below the target marker, as shown in **Fig. 4.1c**. The Blackfly S USB3 was equipped with a 16-mm (0.63-in.) focal length lens and recorded the videos at a rate of 24 fps. The Raspberry Pi HQ camera was equipped with a 16-mm (0.63-in.) telephoto lens and could record videos at 30 fps. Static and dynamic tests were performed, with the camera located at approximately 1.27 m (50 in.) from the truss bridge.

Figure 4.13 shows the measured vertical displacement of the bridge in a static testing detailed in **Sec. 4.2.4.1** using the Raspberry Pi HQ camera. The plot shows the displacement of each individual ArUco marker (the reference and target), and the combination of the two, called the "total displacement". The total displacement at any given time was the displacement by target marker minus the reference marker and then projected into the reference marker frame (**Eq. 3.8**). The figure shows that the total displacements (shown in green) matched well those of the LVDTs with less than 1% error at the peak load. Note that 1% error at the peak load in this test was equal to 0.09-mm (0.0035-in.) displacement. Further, the displacements toward the end of the testing were not zero, which might be due to a slight movement of the bridge during testing, or a slight slip of the LVDTs. Overall, the vertical displacements of the bridge by both DIC and LVDTs were the same.

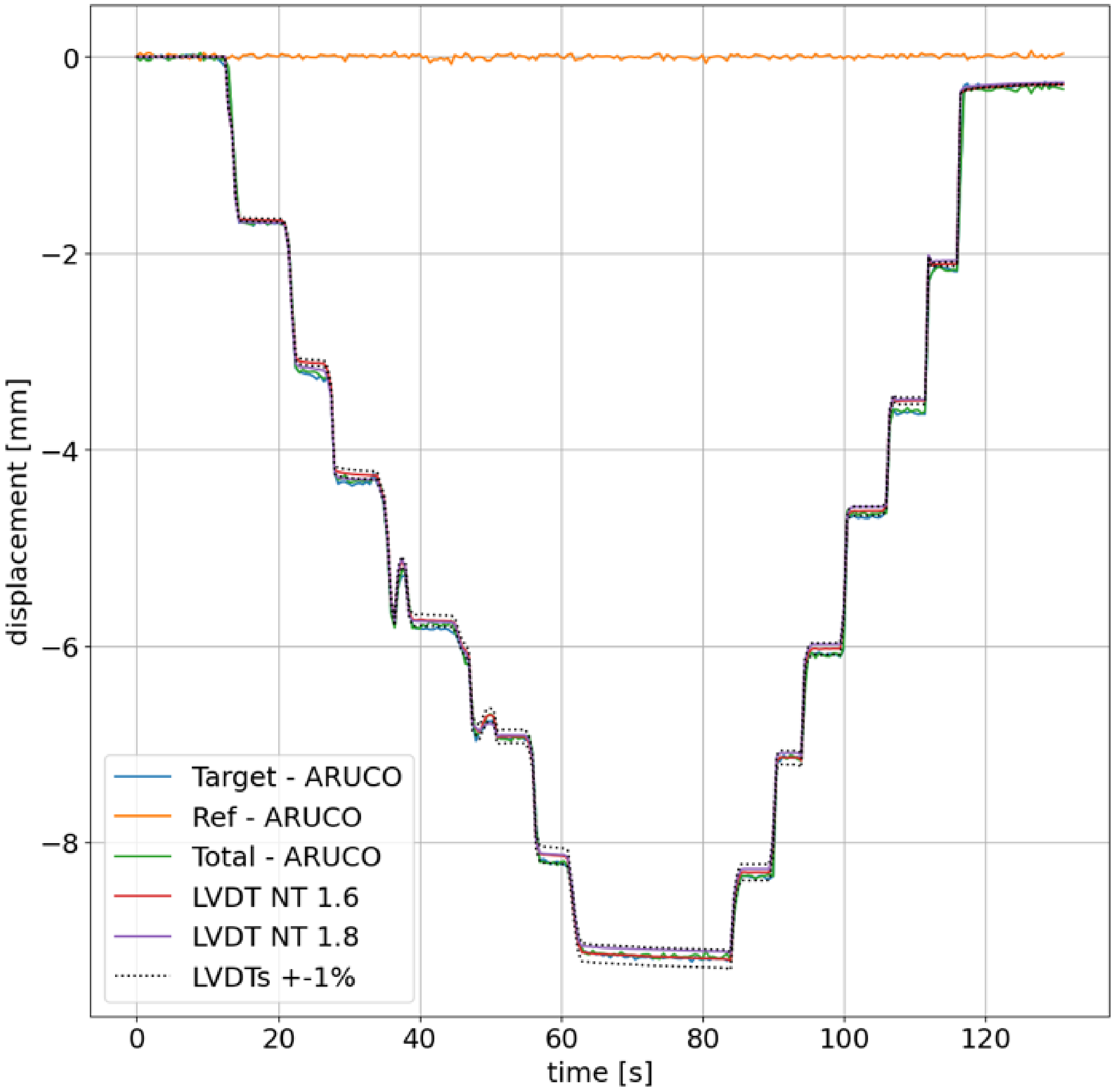

Figure 4.13. Static Test Result with Ground Raspberry Pi HQ Camera with Two Targets

1% error at peak load is equal to 0.09 mm (0.0035 in.)

Figure 4.14 shows the result of a static testing with the Raspberry Pi HQ camera moved using a cart as detailed in **Sec. 4.2.4.3**. The plot includes the displacement of each individual ArUco marker (the target and reference) and the total displacement as defined in the previous section. In this test, the camera was placed on the top of a cart, which was displaced about 50 mm (2 in.) at approximately 50 seconds from the start of the test. Large spikes can be seen in the DIC measurements during the cart movement. These inaccuracies might be due to the vibration of the cart-tripod-camera system during movement caused by an unsmooth laboratory floor and friction, or the limitation of OpenCV. Whenever the cart-camera system was not moving, the total displacement follows those of LVDTs with less than 1% error, which was equivalent to 0.09 mm (0.0035 in.) displacement.

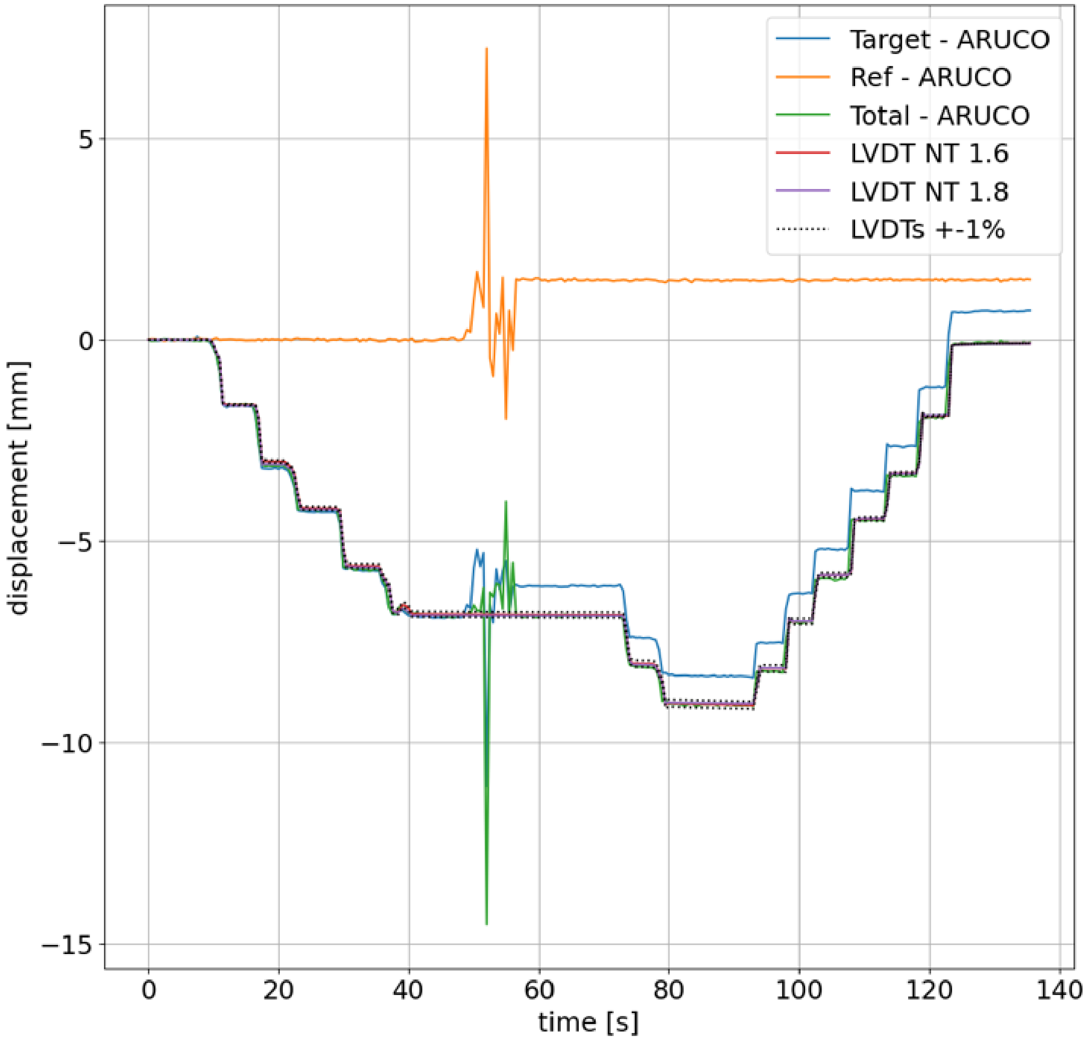

Figure 4.14. Static Test Result with Raspberry Pi HQ Camera on Moving Cart

1% error on the peak load was equal to 0.09 mm (0.0035 in.)

Figure 4.15 shows the result of another static test but using the Blackfly camera on the moving cart. Similar to the previous test, the figure shows the displacement of each individual ArUco marker (the target and reference) and the total displacement. During this static test, the cart was displaced twice at approximately 45 and 90 seconds. Despite the cart-tripod-camera system vibration, the total displacements (marked with green) match well with those of LVDTs with less than 2% error at the peak load. The error in this test was equal to 0.18-mm (0.007-in.) displacement. Furthermore, the Blackfly camera performed better than the Pi camera since no large spike in the displacement was seen when the Blackfly camera was used.

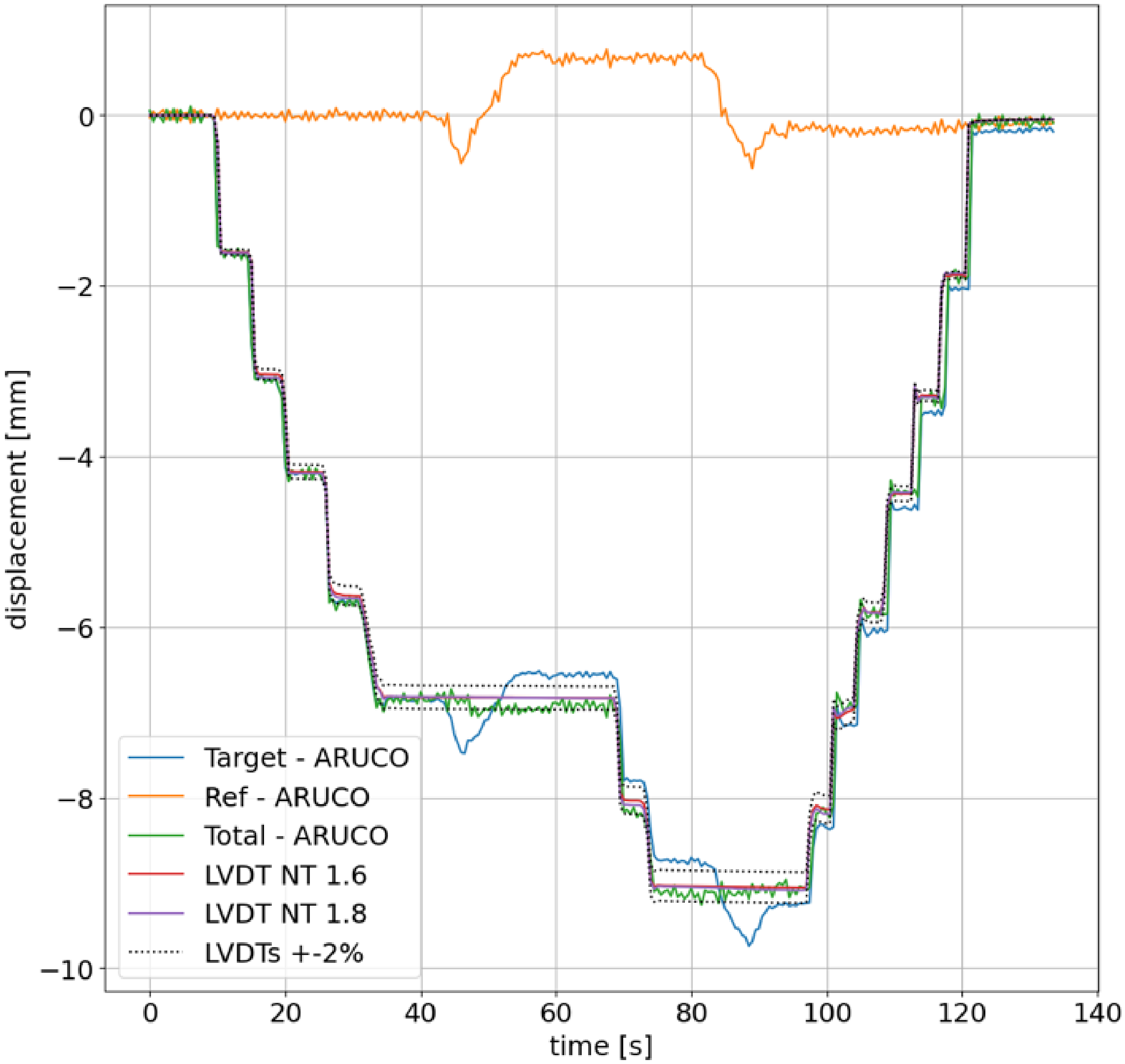

Figure 4.15. Static Test Result with Blackfly Camera on Moving Cart

2% error at the peak load was equal to 0.18 mm (0.007 in.)

Overall, **Fig. 4.14** and **4.15** confirm that the proposed DIC method using a single camera and two markers is viable for static testing as it can measure the bridge displacements with high accuracy. The method can successfully remove camera motions caused by a moving platform from structural displacements.

4.3.3 Two Unsynchronized Ground and Moving Cameras Tracking Two Markers

Further tests were performed using two cameras, the Blackfly S USB3 with 16-mm (0.63-in.) or 50-mm (1.97-in.) focal length lenses, and the Raspberry Pi HQ camera with a 16-mm (0.63-in.) telephoto lens, monitoring two different markers, one marker per camera. Static tests with ground or moving cameras were carried out (following methods discussed in **Sec. 4.2.4.3**), in which the cameras were either 1.2 m (3.93 ft) or 1.5 m (4.92 ft) away from the truss bridge. Two ArUco markers, the target and reference, were included. The target marker was attached to the truss bridge (**Fig. 4.16**), while the reference marker was placed either below the target marker or on the opposite side of the target marker (as shown in **Fig. 4.5**). When the markers were not in the same direction, the reference marker was placed on a pedestal either at the same distance between the camera and its target marker (**Fig. 4.17a**), or at a farther distance of approximately 6 m (19.70 ft). At the 6-m (19.70-ft) distance, larger markers with a size dimension of 406.5 mm (16 in.) (**Fig. 4.17b**) or 1064.5 mm (41.9 in.) (**Fig. 4.17c**) were used as an alternative to the original marker with a side dimension of 117.5 mm (4.62 in.). Only the Blackfly camera equipped with either 16-mm (0.63-in.) or 50-mm (1.97-in.) focal length lens were used for these reference markers. The Blackfly and Raspberry Pi HQ cameras recorded videos at 24 fps and 30 fps, respectively. Since the frame rate for two cameras were different, 2 fps were utilized in the post-processing to obtain the total vertical displacements. Furthermore, due to the use of two different types of cameras, the frames could not be synchronized. Manual synchronizations such as flagging the start frames by hand covering the cameras then removing the hands simultaneously were devised.

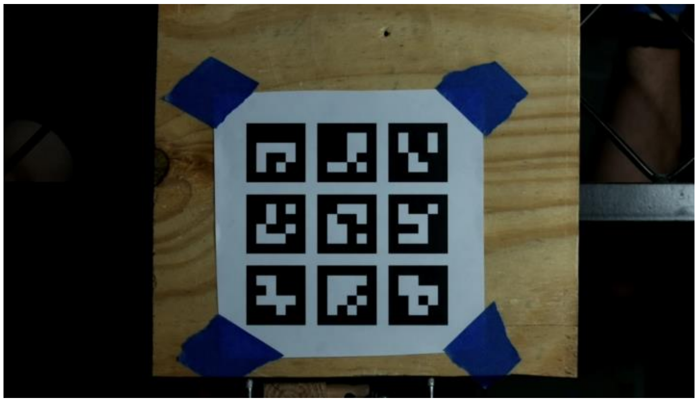

Figure 4.16. A Frame by Raspberry Pi HQ Camera with 16-mm (0.63-in.) Telephoto Lens Looking at Target Marker Attached to Truss Bridge at 1.2 m (3.93 ft) Distance

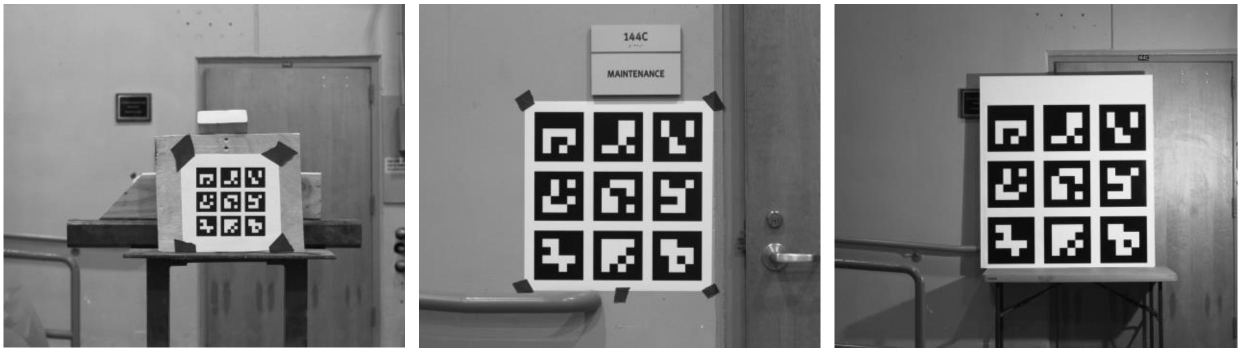

(a)16-mm focal length lens looking at 117.5-mm reference marker at approximately 1.5 m

(b) 50-mm focal length lens looking at 406.5-mm reference marker at approximately 6 m

(c) 16-mm focal length lens looking at 1064.5-mm reference marker at approximately 6.0 m

Figure 4.17. Sample Frames of Reference Marker by Blackfly S USB3 Camera

Figure 4.18 shows the result of a static test with the 117.5-mm (4.62-in.) target marker at 1.2 m (3.93 ft) from the Pi camera, and the 117.5-mm (4.62-in.) reference marker at 1.5 m (4.92 ft) from the Blackfly. The markers were in the opposite direction. The figure includes the displacement of each individual ArUco marker (the target and reference) and the total displacement, which is the bridge displacement by DIC. It is evident that the total displacements (shown in green) were very close to those measured by LVDTs (red) with less than 1% error at the peak load. Note 1% error in this test was equivalent to 0.082 mm (0.003 in.) displacement.

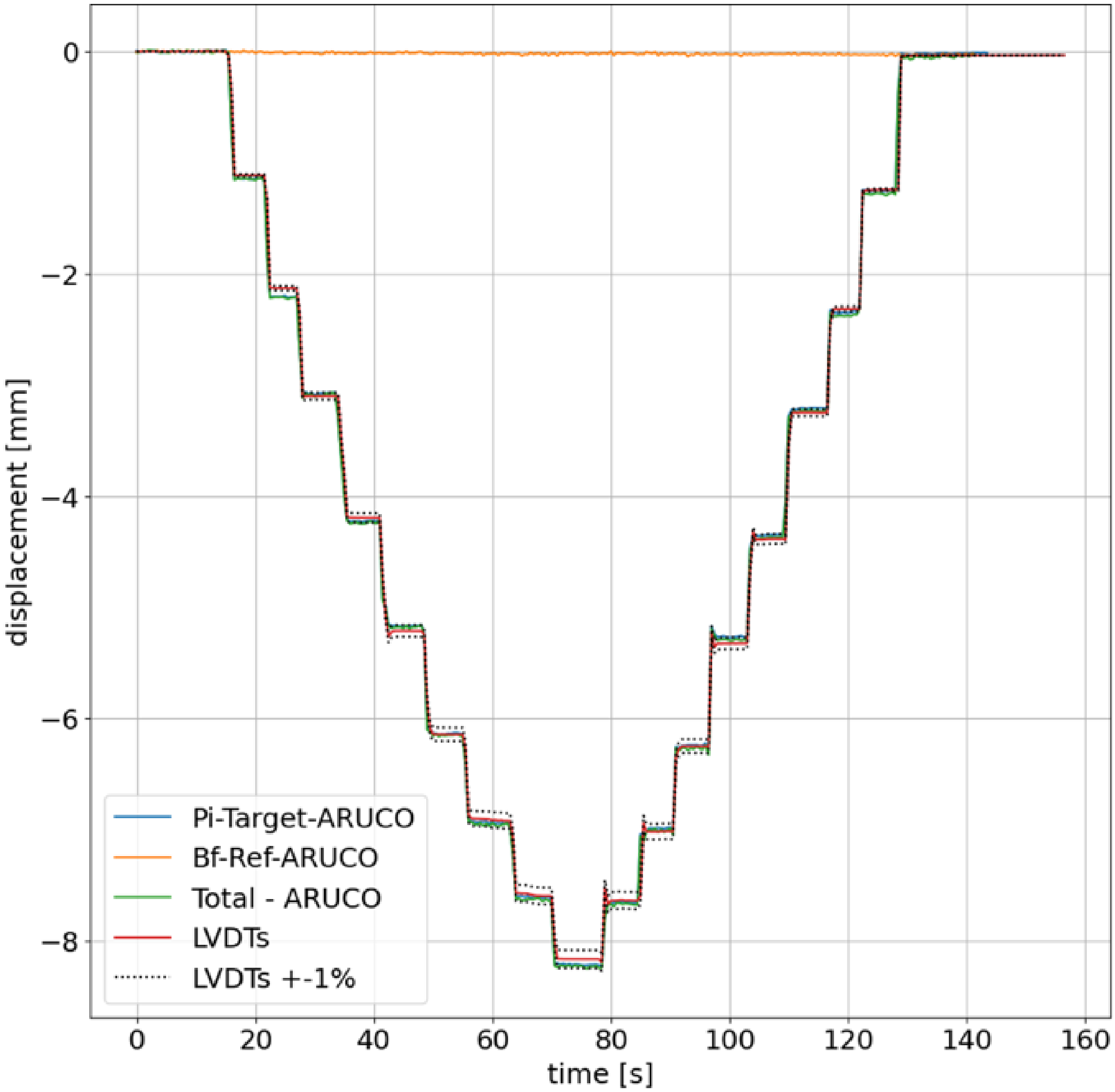

Figure 4.18. Static Test Results with Two Unsynchronized Cameras and Two Markers

1% error at the peak load was equal to 0.082 mm (0.003 in.)

Similar static tests were performed but using larger reference markers placed at a longer distance. **Figure 4.19** shows the results of these static tests performed with the 406.5 mm (16 in.) or 1064.5 mm (41.9 in.) reference markers at 6 m (19.70 ft) from the Blackfly, while the Pi camera was kept at 1.2 m (3.93 ft) and 1.5 m (4.92 ft) from the truss bridge. The total displacements were very close to those of LVDTs.

These tests confirmed that cameras with a smaller focal length measuring displacements of large markers placed at further distance perform approximately the same as cameras with higher focal lengths placed closer to the marker with a smaller size. However, errors are larger as the reference marker is smaller or at longer distance. This is evident in **Fig. 4.19a** by a noisy response from the reference marker.

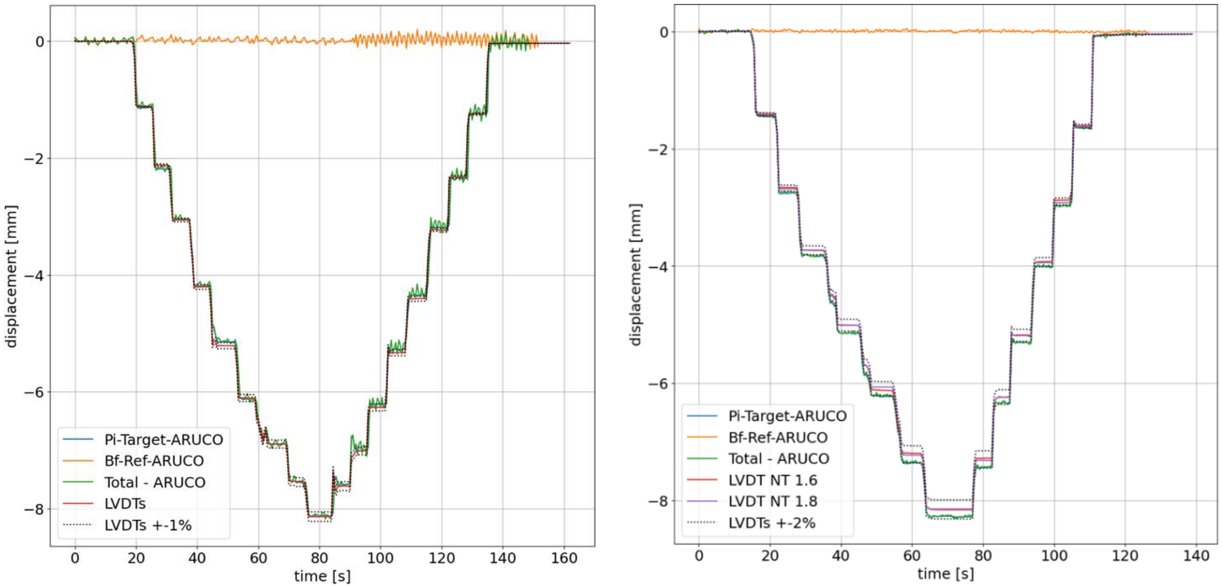

(a) 406.5 mm (16 in.) Reference Marker, 1% error was equal to 0.082 mm (0.003 in.) displ. at peak load

(b) 1064.5 mm (41.9 in.) Reference Marker, 2% error was equal to 0.163 mm (0.006 in.) displ. at peak load

Figure 4.19. Static Test Results with Two Unsynchronized Cameras and Markers with Different Sizes

Figure 4.20 shows the result of another static test with two moving cameras on an oscillating platform as detailed in **Sec. 4.2.4.3**. In this test, the 117.5-mm (4.62-in.) target marker was at 1.2 m (3.93 ft) from the Pi camera, and the 117.5-mm (4.62-in.) reference marker was also at 1.2 m (3.93 ft) from Blackfly. The figure shows the total displacement by the DIC method. Several spikes with large displacement errors can been seen (**Fig. 4.20a**). Lack of camera synchronization in time and frame rates (**Fig. 4.20b**) was the main source of this inferior performance compared with other static tests. To resolve this issue, a manual synchronization was performed in which the response of one of the cameras (marked orange) was shifted back in time to match with the response of the other camera (blue). Despite this initial synchronization, the total displacement was also noisy (**Fig. 4.21**), probably due to a lack of full synchronization.

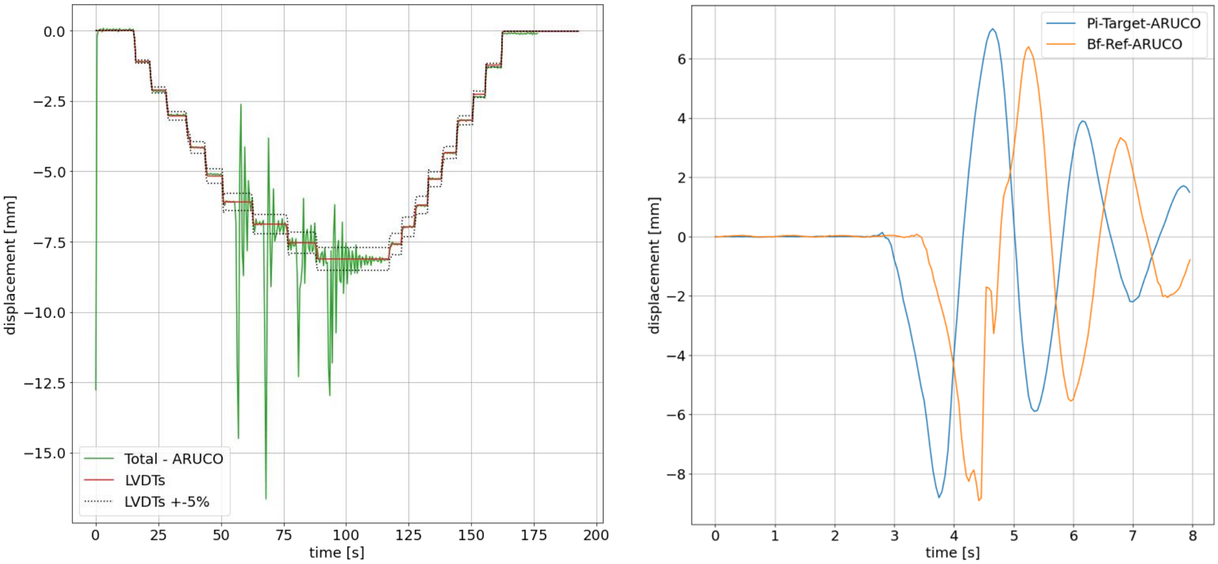

(a) Total Displacement

(b) Time Discrepancy

Figure 4.20. Static Test Results with Two Unsynchronized Oscillating Cameras

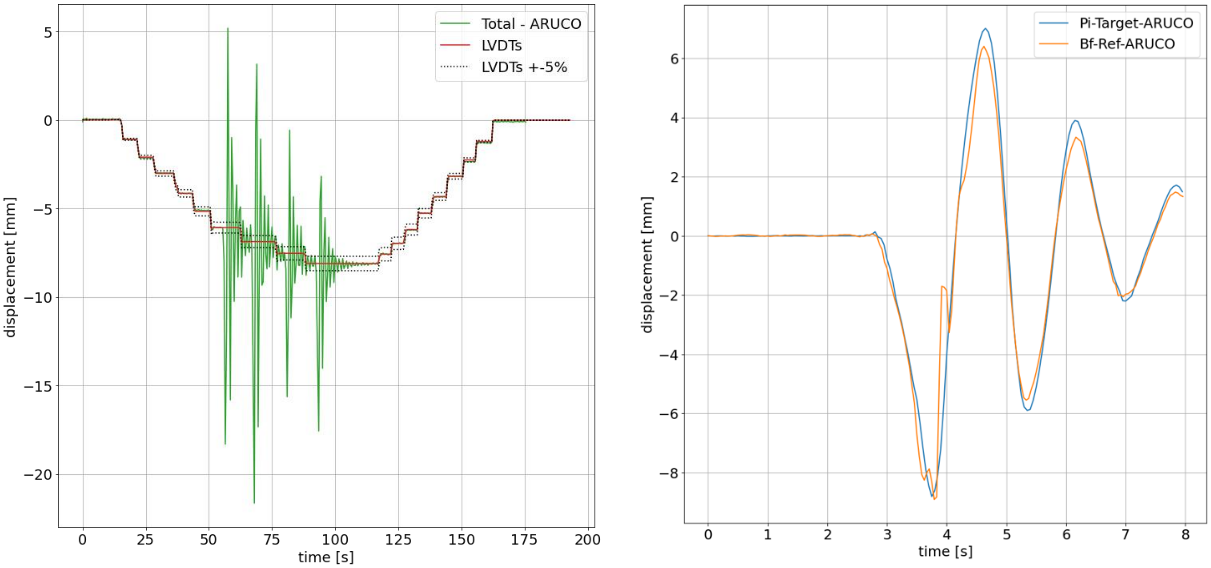

(a) Total Displacement

(b) Initial Manual Synchronization

Figure 4.21. Static Test Results with Two Unsynchronized Oscillating Cameras with Initial Synchronization

4.3.4 Two Synchronized Ground and Moving Cameras Tracking Two Markers

The synchronization issues were discussed in the previous section. Further tests were performed but using two Blackfly cameras which were synchronized using in-house programming. Both cameras could simultaneously read at a frame rate of 20 fps. Static and dynamic tests were performed using either ground or oscillating cameras located at approximately 1.2 m (3.93 ft.) from the truss bridge.

As shown in **Fig. 4.22**, both reference and target ArUco markers were utilized. The reference marker was placed at the bottom and the target marker at the top if both cameras were in the same direction. Otherwise, the reference marker was placed in the opposite direction of the target marker. Two different marker sizes were used: the small and original marker with a side dimension of 117.5 mm (4.62 in.) and a medium size marker with a side dimension of 406.5 mm (16 in.). The medium marker was used only as the reference marker when it was placed at a farther distance of 6 m (19.70 ft.). The camera looking at the reference marker was equipped with 16 mm or 50 mm focal length lenses when the marker was at longer distance.

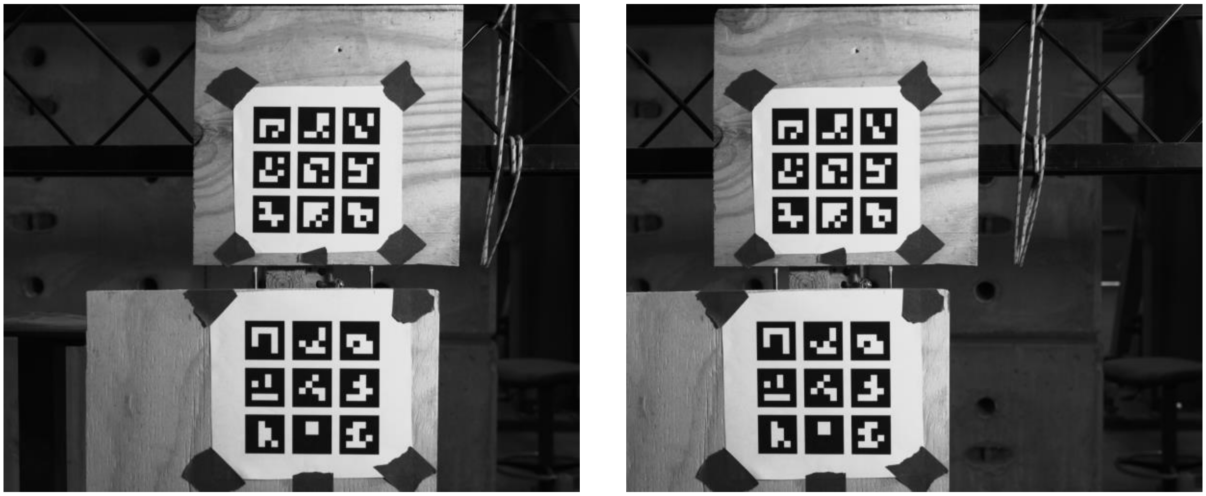

(a) Blackfly-1 facing both target (top) and reference (bottom)markers using 16 mm focal length lens

(b) Blackfly-2 facing both target (top) and reference (bottom) markers using 16 mm focal length lens

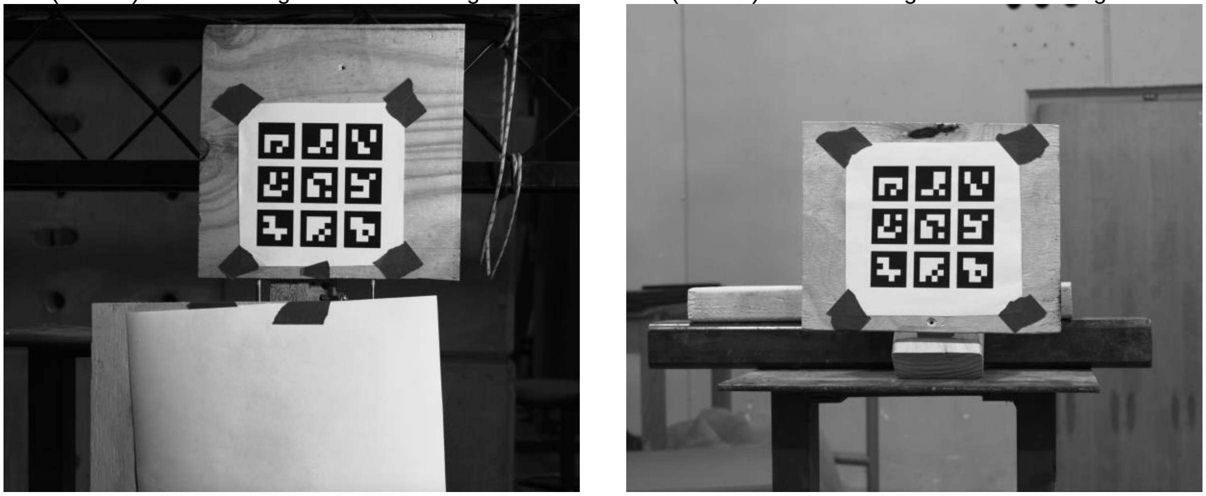

(c) Blackfly-1 facing target marker on bridge using 16 mm focal length lens

(d) Blackfly-2 facing reference marker in the opposite direction of target using 16 mm focal length lens

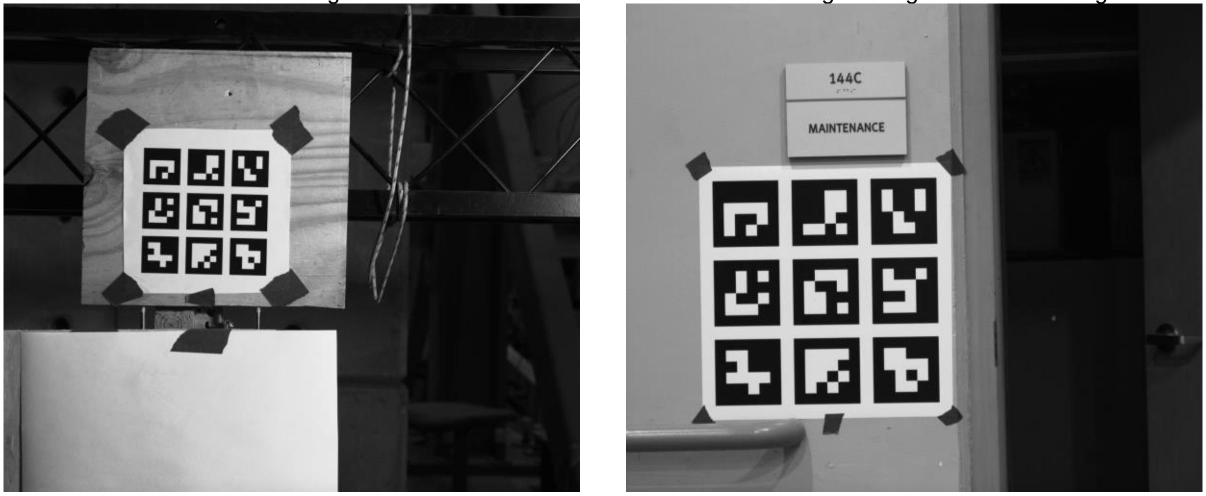

(e) Blackfly-1 facing target marker on bridge using 16 mm focal length lens

(f) Blackfly-2 facing reference marker in the opposite direction of target at 6 m using 50 mm focal length lens

Figure 4.22. Sample Frames from Two Synchronized Blackfly Cameras

Figure 4.23 shows the results of a static test in which the cameras had 16-mm (0.63-in.) focal length lenses and were located at approximately 1.2 m (3.93 ft.) of the truss bridge. The reference and target markers were in the same direction and both with the small size ArUco marker. The figure includes the displacement of each individual ArUco marker (reference and target), and the total displacement colored in green. It can be seen that the DIC total displacements were very close to the LVDT displacements (colored in red), with less than 3% error at the peak load. This error was equivalent to 0.24 mm (0.009 in.) displacement in this test.

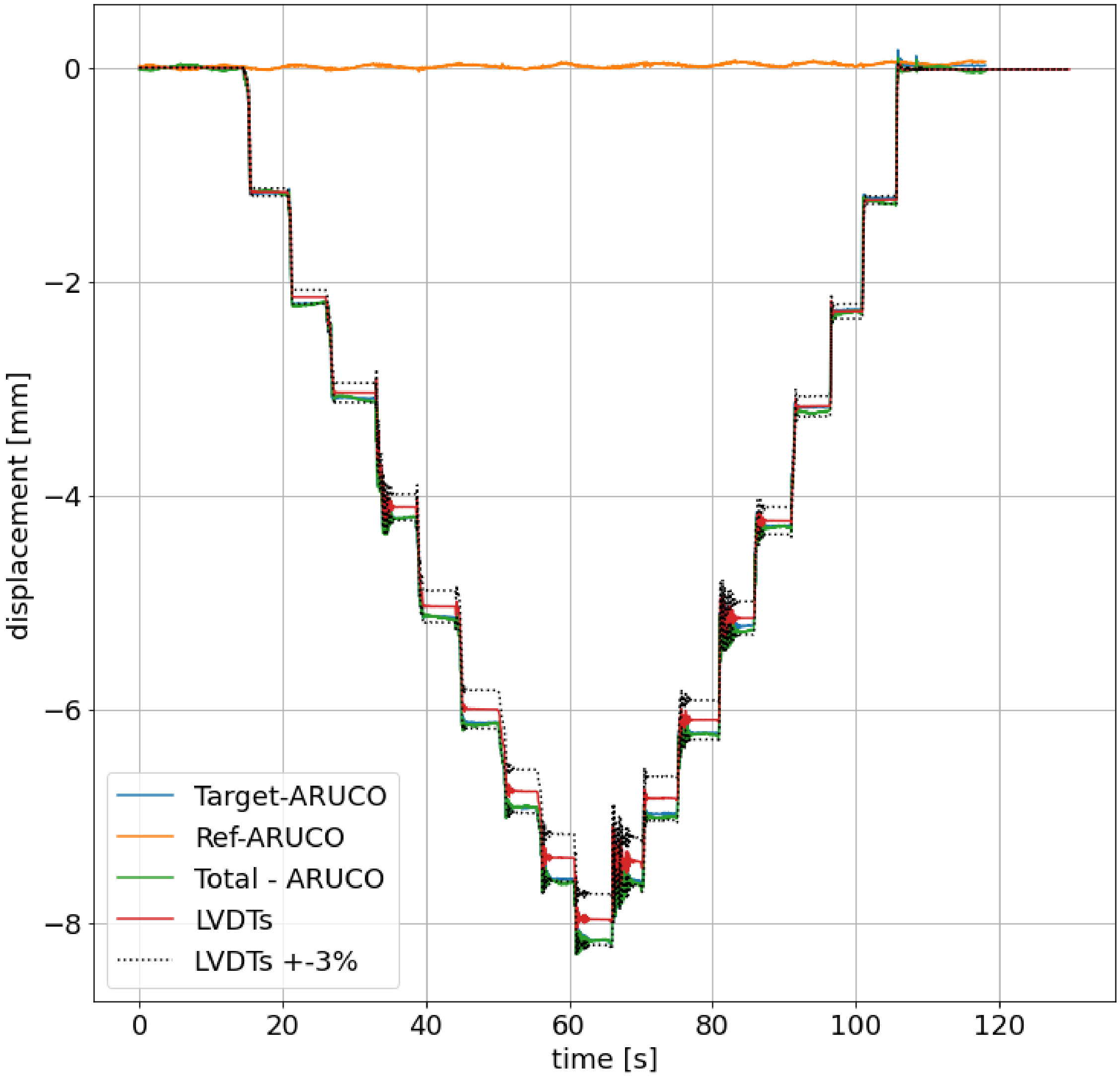

Figure 4.23. Static Test Results with Two Synchronized Cameras and Two Markers in Same Direction

3% error at the peak load was equal to 0.24 mm (0.009 in.)

Further static tests were performed in which the synchronized cameras were on the oscillating platform discussed in **Sec. 4.2.4.3**. Both cameras had 16-mm (0.63-in.) focal length lenses. In one test, both cameras were looking at the markers in the same direction, and in another test the cameras were looking at markers in opposite directions. The distance between the camera system and the two small size ArUco markers (the reference and target) was approximately 1.2 m (3.93 ft.). During each test, the camera platform was tapped three times to oscillate, which can be easily distinguished in the response (**Fig. 4.24**). It can be seen that the DIC displacements in both tests were close to the LVDT displacements with less than 5% errors, which was equal to 0.41 mm (0.016 in.). Note that the right-side images are the same as the left ones but just showing the total displacements by DIC. There were several spikes in the signal during the camera motions, which might be due to blurred images and limitations of the proposed system. The spikes were minimal when the camera motion stopped. Comparing **Fig. 4.21** with **4.24**, it is evident that syncing two cameras in terms of timing and frame rate can significantly improve the DIC measurements by reducing the number and amplitude of spikes resulting in a better displacement measurement.

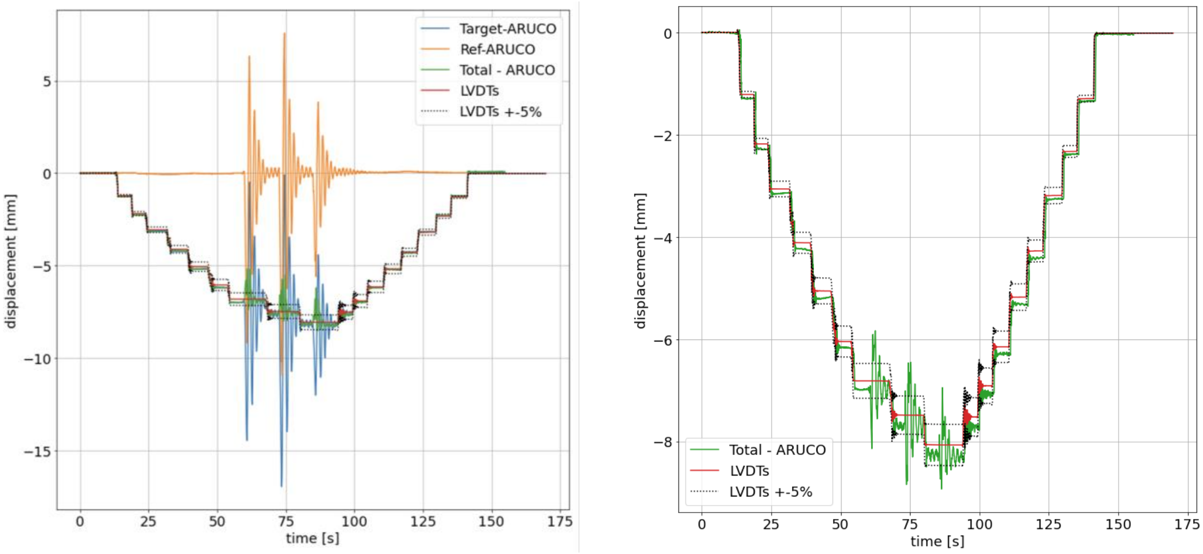

(a) Cameras facing the same direction, right showing DIC and LVDT response

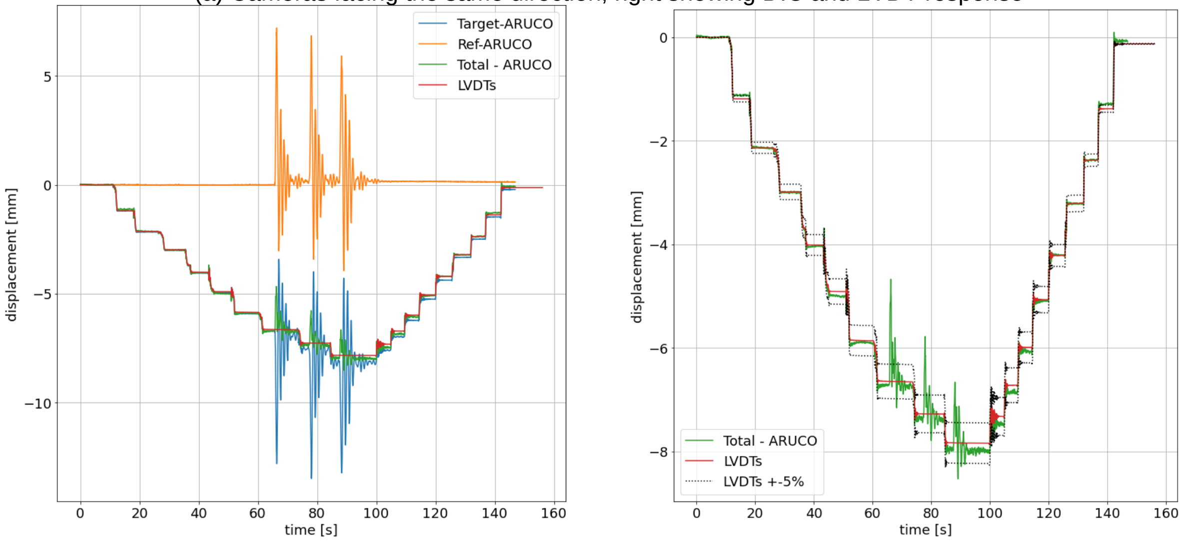

(b) Cameras facing opposite directions, right showing DIC and LVDT response

Figure 4.24. Static Test Results with Two Synchronized Oscillating Cameras

5% error at the peak load was equal to 0.41 mm (0.016 in.)

Figure 4.25 shows the results of a dynamic test following the method discussed in **Sec. 4.2.4.2** utilizing two synchronized cameras on the oscillating platform discussed in **Sec. 4.2.4.3**. In other words, this test was to evaluate the accuracy of the DIC method when the bridge was dynamically loaded, and the cameras were oscillating. Both cameras had 16-mm (0.63-in.) focal length lenses. In one test, both cameras were looking at the markers in the same direction, and in another test the cameras were looking at markers in opposite directions. The distance between the camera system and the two small size ArUco markers (the reference and target) was approximately 1.2 m (3.93 ft.). During each dynamic test, the camera platform was tapped four times to oscillate. The DIC total displacements followed well the LVDT response (**Fig. 4.25**) in the dynamic testing in which each the period of the load was less than 1.0 second and its amplitude was 4 to 5.5 mm (0.16 to 0.21 in.). The error at each peak was 2% (0.08 mm or 0.003 in.), 14.1% (0.57 mm or 0.02 in.), 6% (0.29 mm or 0.01 in.), 15% (0.71 mm or 0.027 in.), and 7.3% (0.38 mm or 0.015 in.) for the test reported in **Fig. 4.25a.**, and 3.2% (0.14 mm or 0.005 in.), 6.4% (0.3 mm or 0.011 in.), 5.9% (0.27 mm or 0.01 in.), 2.47% (0.12 mm or 0.005 in.), 2.36% (0.125 mm or 0.005 in.) for the test reported in **Fig. 4.25b**.

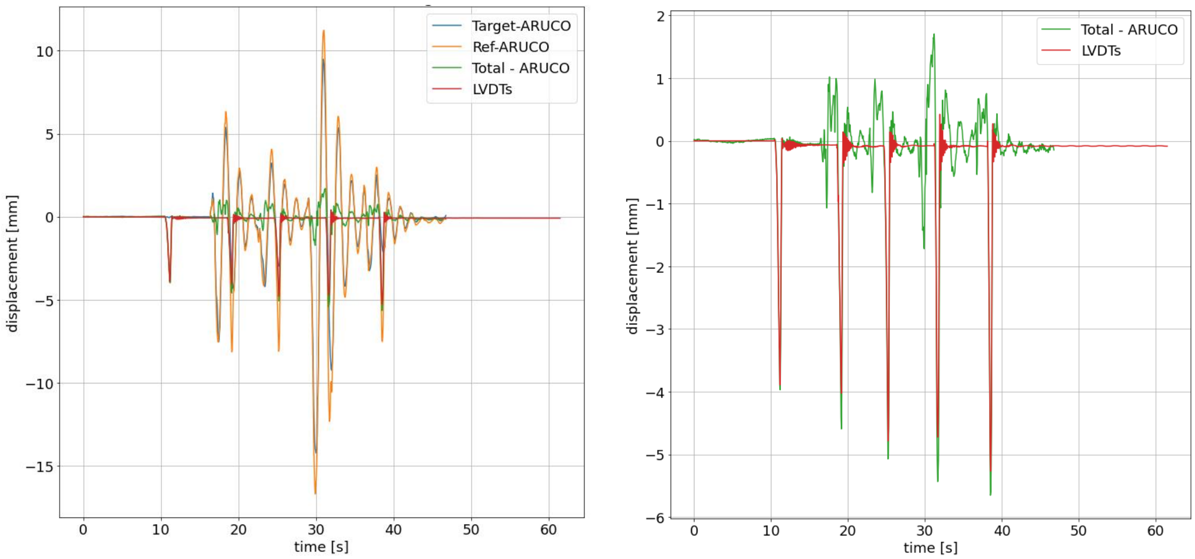

(a) Cameras facing the same direction, right showing DIC and LVDT response

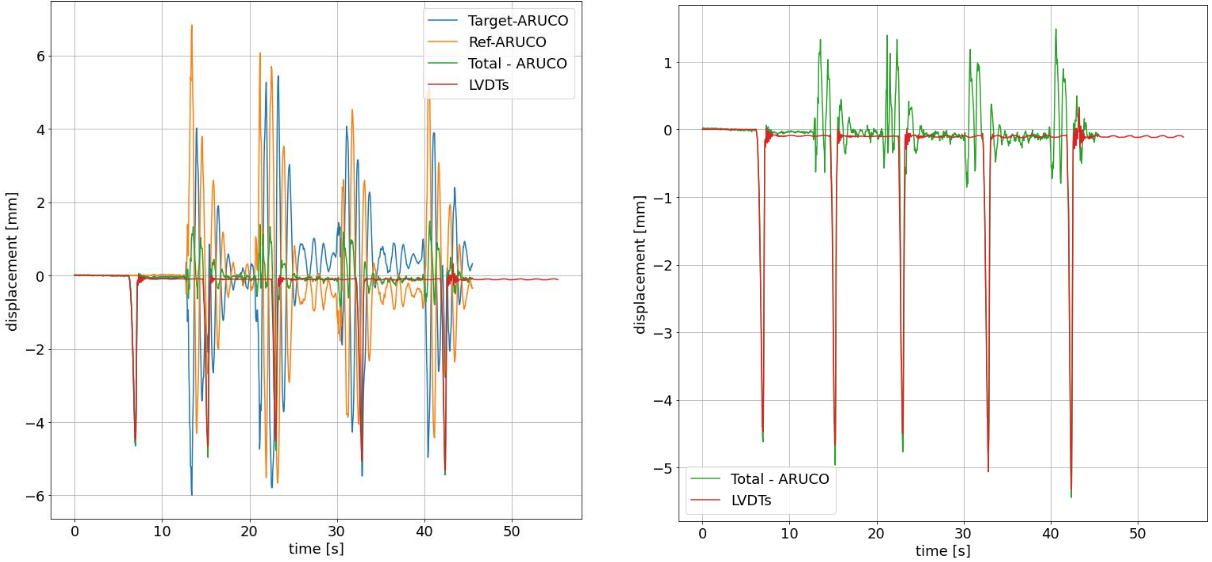

(b) Cameras facing opposite directions, right showing DIC and LVDT response

Figure 4.25. Dynamic Test Results with Two Synchronized Oscillating Cameras

Another dynamic test similar to that discussed above was carried out; however, a medium size (406.5-mm or 16-in.) marker as the reference was placed approximately 6 m (19.70 ft.) away from the cameras. The camera system was kept at 1.2 m (3.93 ft.) of the truss bridge. In addition to the dynamic test, a static test was also performed. The results of the dynamic and static tests are shown in **Fig. 4.26**. The results of these tests were not as promising as the previous ones, since the reference marker was placed at a long distance from the camera system while measuring very small displacements. In other words, the proposed DIC method incorporating the equipment used herein while the camera system is oscillating is viable only at close ranges of the bridge.

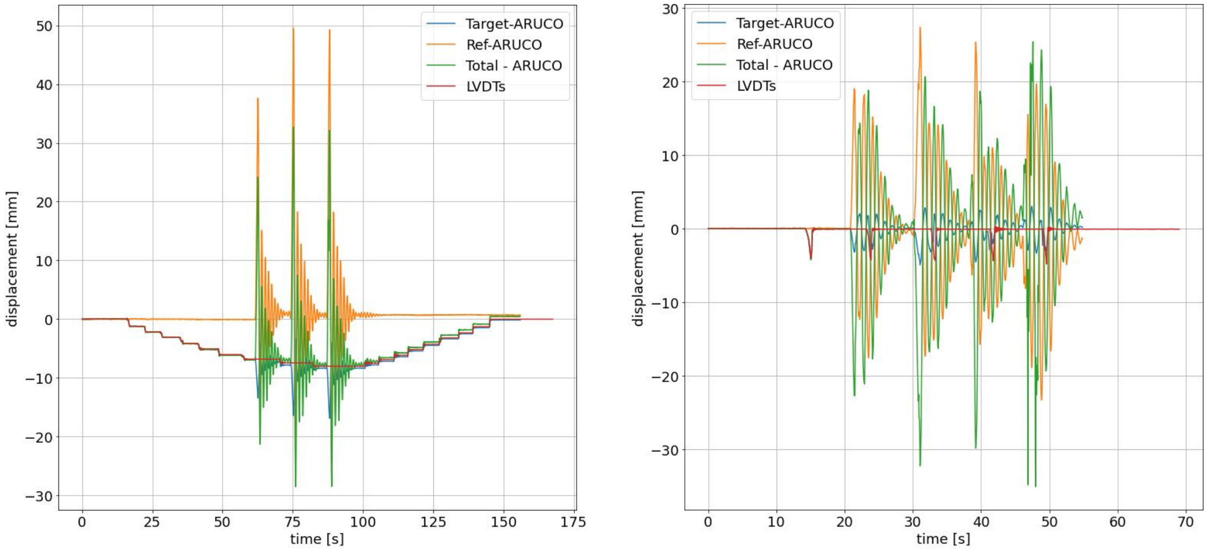

(a) Static Tests with with Oscillating Cameras, 406.5-mm Reference Marker at 6 m

(b) Dynamic Test with Oscillating Cameras, 406.5-mm Reference Marker at 6 m

Figure 4.26. Static and Dynamic Test Results with Two Synchronized Oscillating Cameras at Opposite Directions

4.3.5 Two Synchronized Cameras Mounted on Drone

The last series of testing in this project was to mount the camera system on a drone to evaluate the accuracy of the proposed DIC method. Based on the lessons learned from the previous experiments, two Blackfly cameras each equipped with a 16-mm (0.63-in.) focal length lens were synchronized and then attached to a mini-PC for data recording. The camera-PC system was mounted on the DJI MATRICE 210 V2 as shown in **Fig. 4.10**. Both static and dynamic tests were exercised. During each test, the drone was flying at approximately 1.5 m (4.9 ft.) from the truss bridge and the video was recorded at 20 fps. The reference (bottom) and the target (top) ArUco markers were included, as shown in **Fig. 4.27**. These markers had a side dimension of 117.5 mm (4.62 in.).

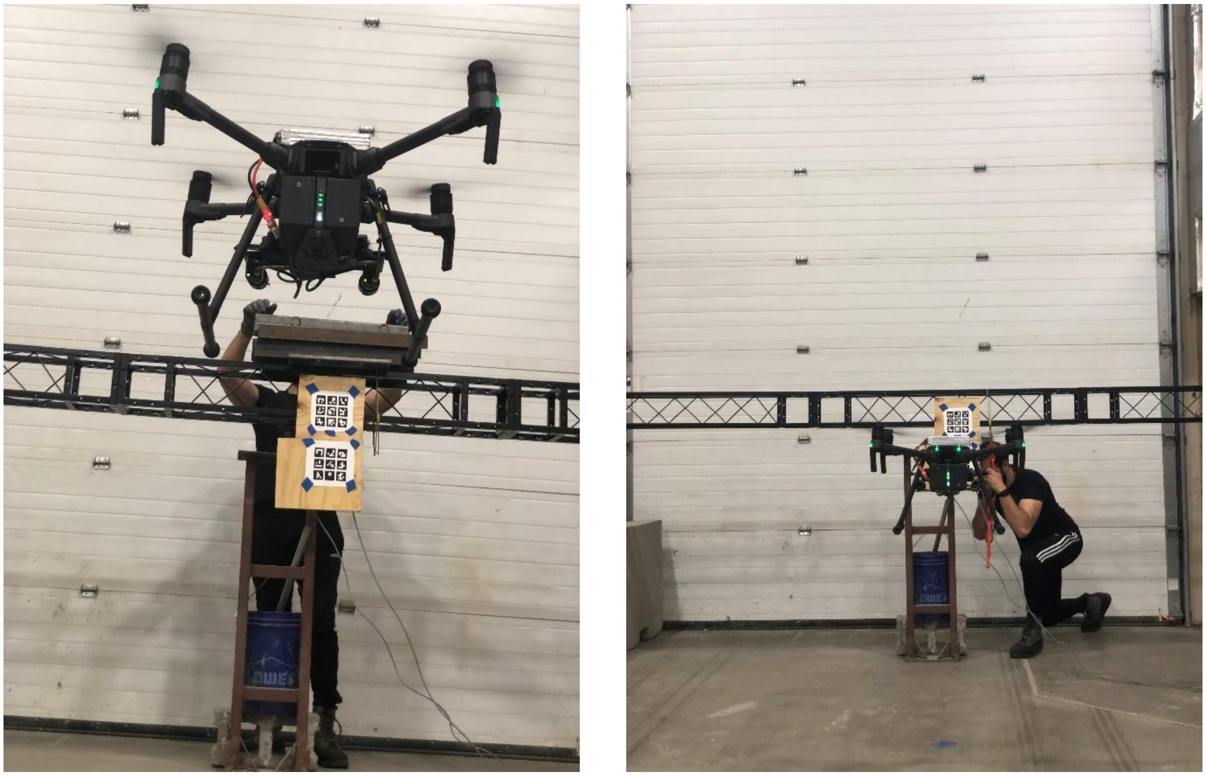

(a) Static Testing by Adding Weights

(b) Dynamic Testing by Pulling Bridge Down

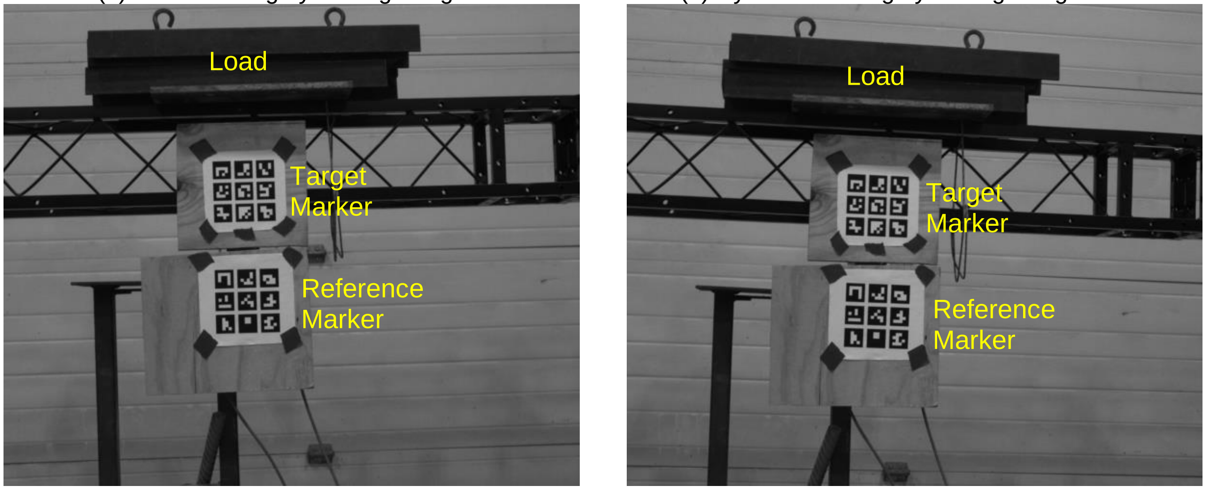

(c) Image by Blackfly-1 Camera

(d) Image by Blackfly-2 Camera

Figure 4.27. Sample Frames from Two Synchronized Blackfly Cameras Mounted on Drone

The truss bridge vertical displacement caused by the vertical load was of interest. In the proposed DIC method, the total vertical displacement of the target marker with respect to the reference marker is the bridge vertical displacement. Since both cameras were in the same direction, it was feasible to extract the displacement of both markers using a single camera, and also assigning one camera to each marker. The latter will be more realistic in actual bridge field testing as both markers won't be in the FOV of a camera. **Figure 4.28** shows the bridge displacement under a static testing in which a single camera of the drone was used to calculate the DIC displacements of both markers. The plots on the left side include the displacement of each individual ArUco marker and the total displacement in green. It can be seen that the total displacements were close to those of LVDTs (in red). The plot on the right does not include individual DIC marker response for ease of comparison. Several spikes can be seen which were due to the motion of the drone that caused blurry images and are the limitations of the proposed system. To improve the response, a low-pass filter with a cut-off frequency of 0.25 Hz was used to smoothen the signal. The filtered total displacement had 5% error at the load peak compared with the LVDT displacements. This level of error was equivalent to 0.375-mm (0.014-in.) of displacement.

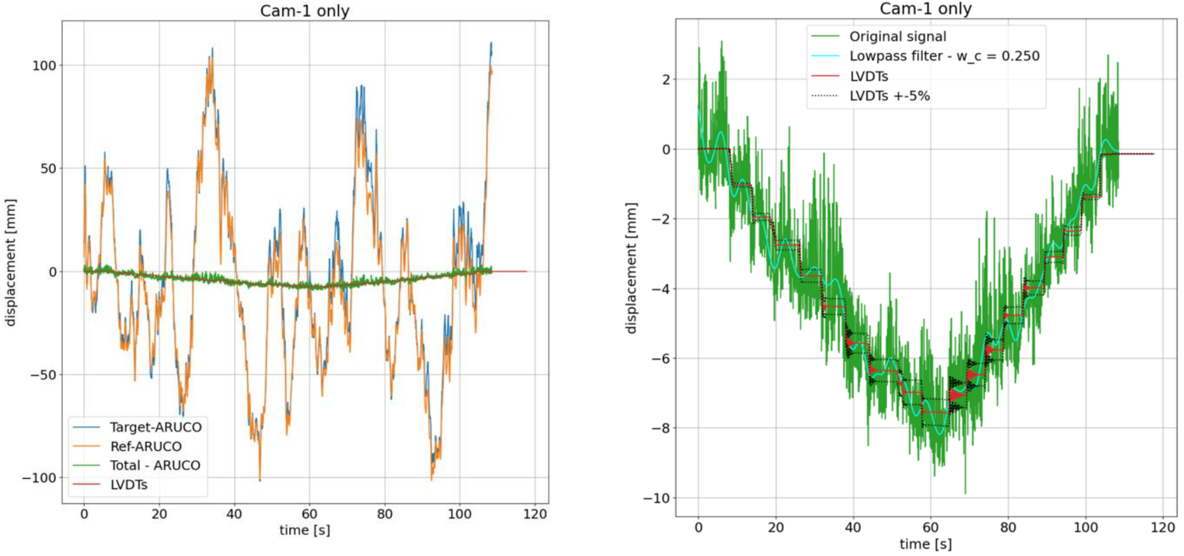

(a) Blackfly-1 Camera Only, Right Showing DIC and LVDT Response

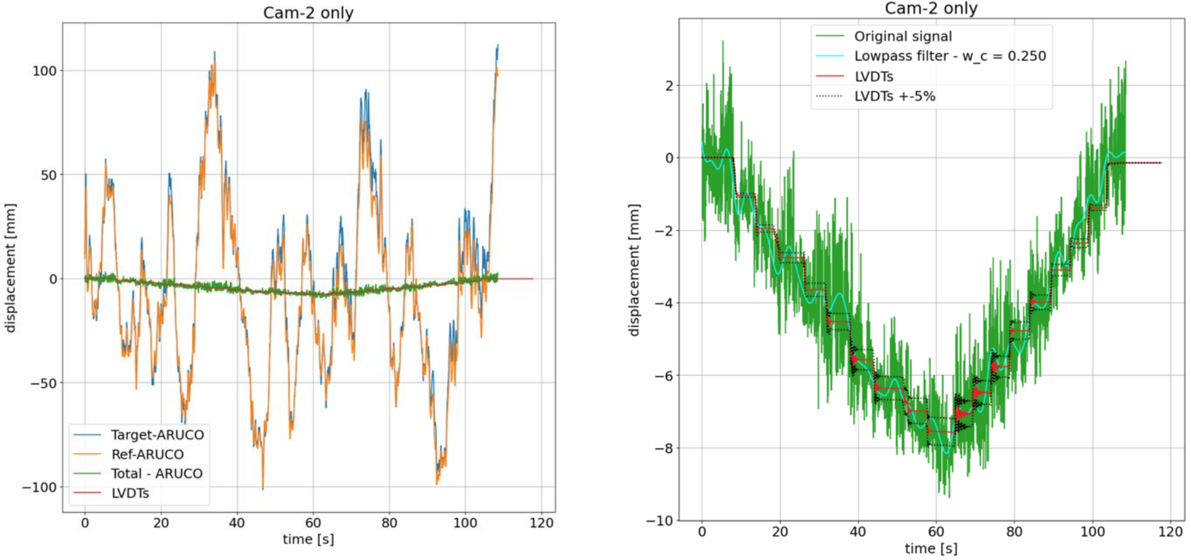

(b) Blackfly-2 Camera Only, Right Showing DIC and LVDT Response

Figure 4.28. Static Test Results with Drone using Single Camera Data

Figure 4.29 shows the bridge displacement calculated by assigning one camera to one marker. A larger error compared with the previous cases (one camera watching both targets) was observed. This was because the two cameras did not detect all the sub-markers of the target/reference markers in all frames. Note each marker had nine sub-markers as shown in **Fig. 4.27**. For example, a marker in Frame No. 2 was not detected by Camera-2, but it was detected by Camera-1. To overcome this issue, whenever the marker was not detected, instead of discarding the frame, the DIC characteristics (e.g., rotation and translation vectors) of the last detected frame were utilized in the calculation of the missing frame displacement.

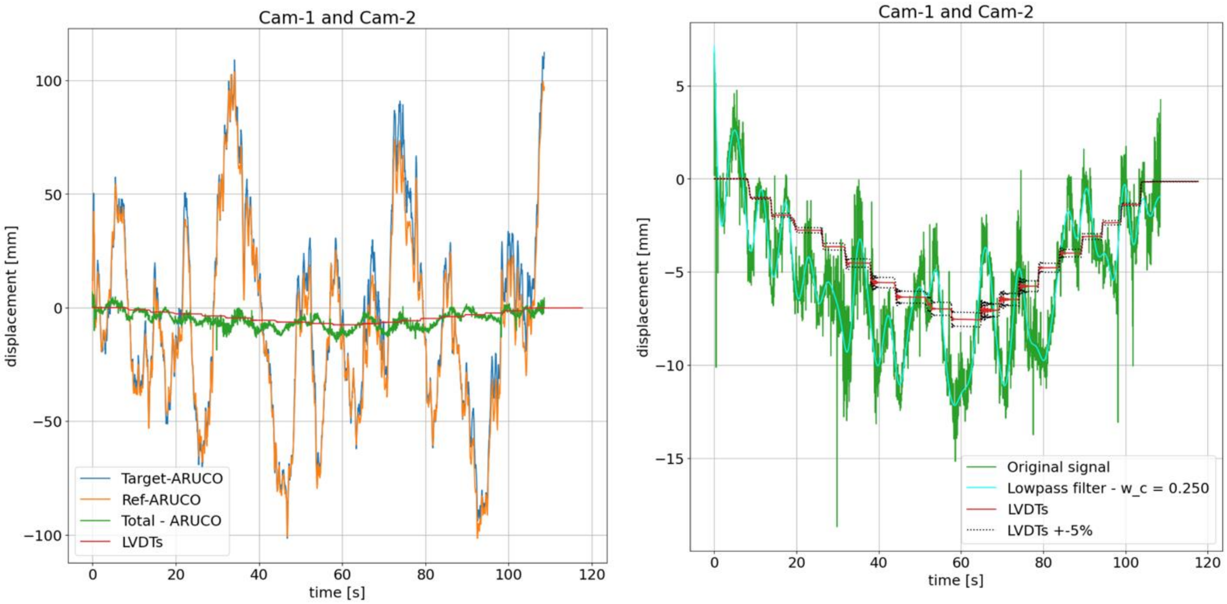

(a) Blackfly Cameras 1 & 2 Combined (b) Same as (a) but Showing DIC and LVDT Response

Figure 4.29. Static Test Results with Drone using Combination of Two Camera Data

To investigate the drone measured displacements under fast loading, dynamic tests were also performed. Similar to the static tests, the two cameras were synchronized and recorded videos at 20 fps while the drone was flying at approximately 1.5 m (4.9 ft.) of the truss bridge. The dynamic test was performed by quickly pulling the bridge down as shown in **Fig. 4.27b**. **Figure 4.30** shows the bridge displacements by DIC and LVDTs. The total displacement retrieved by individual camera followed well the LVDT response under this dynamic loading in which each load cycle was less than one second with an amplitude of 5.5 mm (0.21 in.). The error at each peak was 3.89% (0.20 mm or 0.0078 in.), 10% (0.54 mm or 0.02 in.), 1.09% (0.062 mm or 0.0024 in.), 3.85% (0.21 mm or 0.0085 in.), and 11.41% (0.68 mm or 0.027 in.) for the test reported in **Fig. 4.30a.**, and 15.84% (0.81 mm or 0.03 in.), 18.82% (1.12 mm or 0.04 in.), 10.73% (0.61 mm or 0.024 in.), 0.04% (0.0025 mm or 0.000099 in.), and 4.15% (0.25 mm or 0.009 in.) for the test reported in **Fig. 4.30b**.

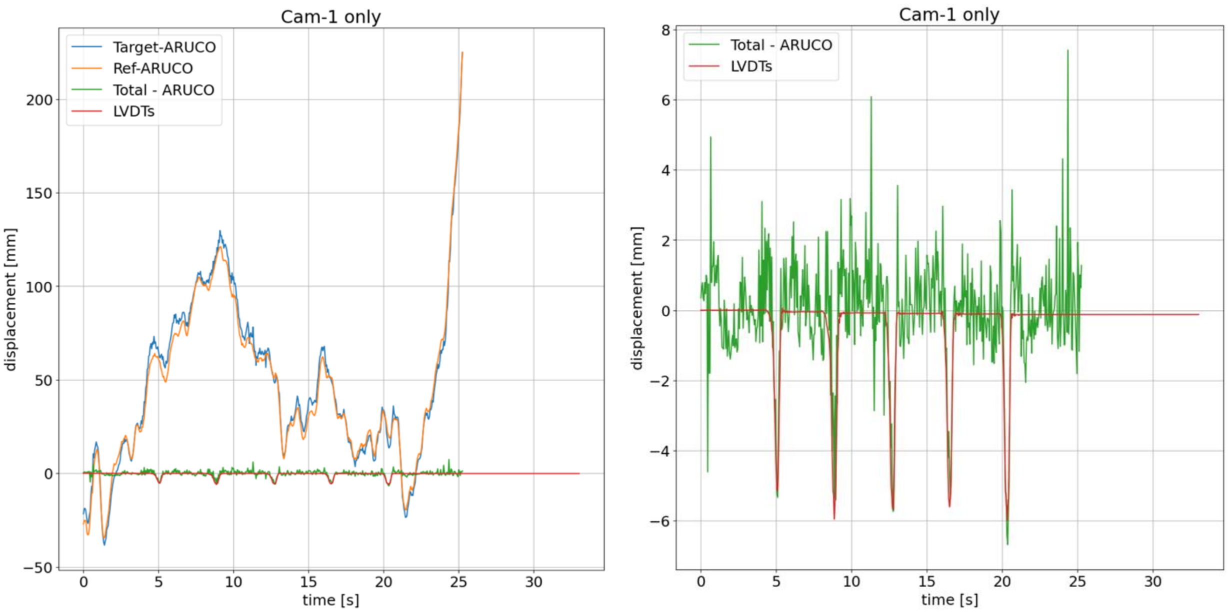

(a) Blackfly-1 Camera Only, Right Showing DIC and LVDT Response

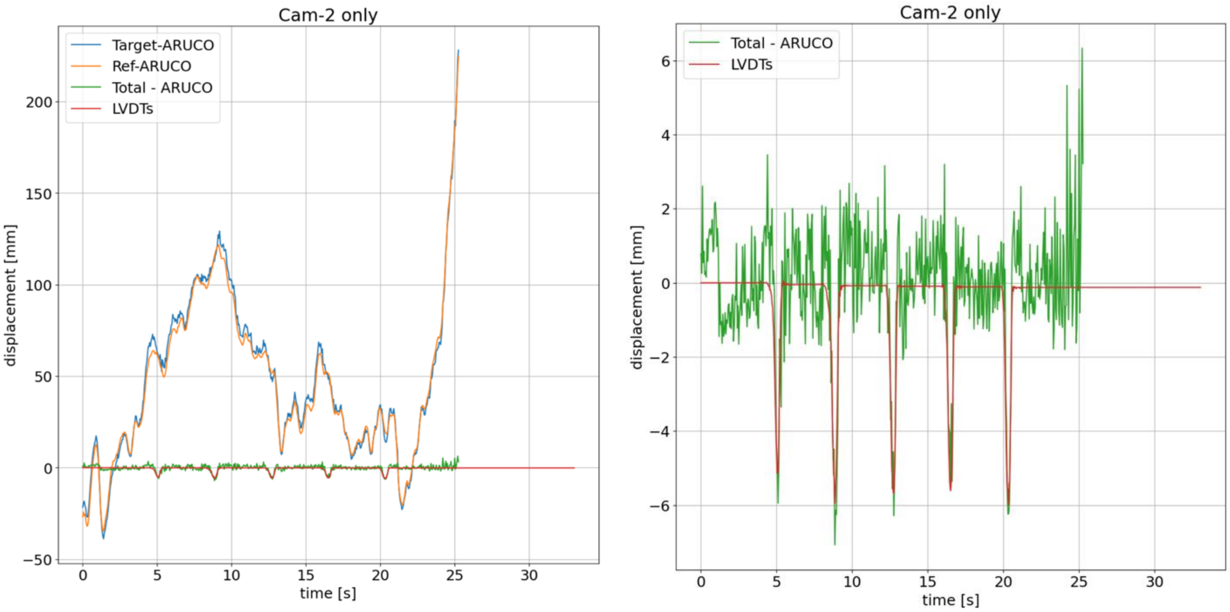

(b) Blackfly-2 Camera Only, Right Showing DIC and LVDT Response

Figure 4.30. Dynamic Test Results with Drone using Single Camera Data

Fig. 4.31 shows the displacement of the bridge calculated using combined data from both drone cameras, as opposed to a single camera response presented in the previous section. The combined use of drone data (one for reference, one for target) showed some level of accuracy as can be seen in **Fig. 4.31**. The results in the dynamic tests were more accurate than those in the static tests since the marker detection issue was not as present as before. Even though the peak displacements were better matched with the LVDT response compared with the static test, several spikes exist, and the error was higher than those of a single camera response.

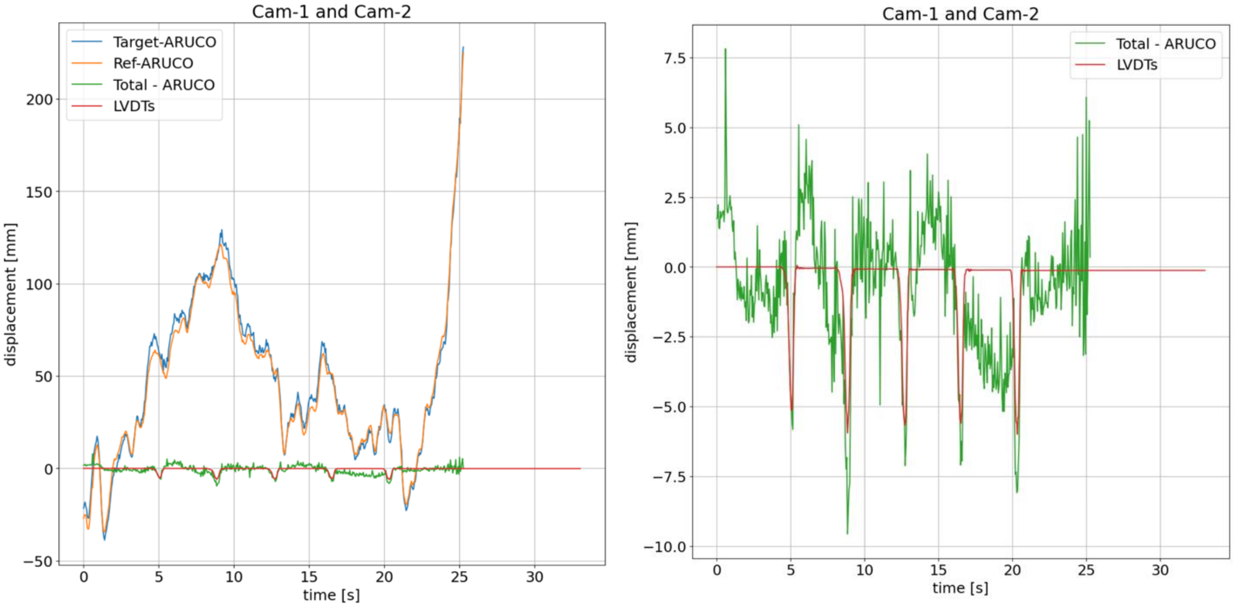

(a) Blackfly Cameras 1 & 2 Combined (b) Same as (a) but Showing DIC and LVDT Response

Figure 4.31. Dynamic Test Results with Drone using Combination of Two Camera Data

To improve the results, the frequency content of the total displacement was calculated. As shown in **Fig. 4.32**, the signal was affected by noise with frequencies less than 2 Hz. To compensate for this effect, we applied a high-pass filter (HPF) with a cut-off frequency equal to 0.22 Hz. We further applied Savitzky–Golay filter to the signal to smoothen the data. The Savitzky-Golay is a type of low-pass filter, particularly suited for smoothing noisy data. The main technique in this approach is to fit a least-square polynomial of high order over an odd-sized window centered at the point. By selecting a 13th order polynomial, the new signal appears to be smoother than only using a high-pass filter, as shown in **Fig. 4.33**. In turn, using a combination of HPF and Savitzky-Golay filter, it was possible to remove the high frequency noise and to smoothen the signal, without losing significant information related to the truss bridge vertical displacements. With this signal processing, the error at each peak was 14.45% (0.74 mm or 0.03 in.), 16.17% (0.96 mm or 0.037 in.), 5.41% (0.306 mm or 0.012 in.), 1.53% (0.085 mm or 0.0033 in.), and 10.85% (0.65 mm or 0.025 in.).

Note that this approach is suitable for dynamic tests. If it (HPF) is used in static tests, it will flatten the signal.

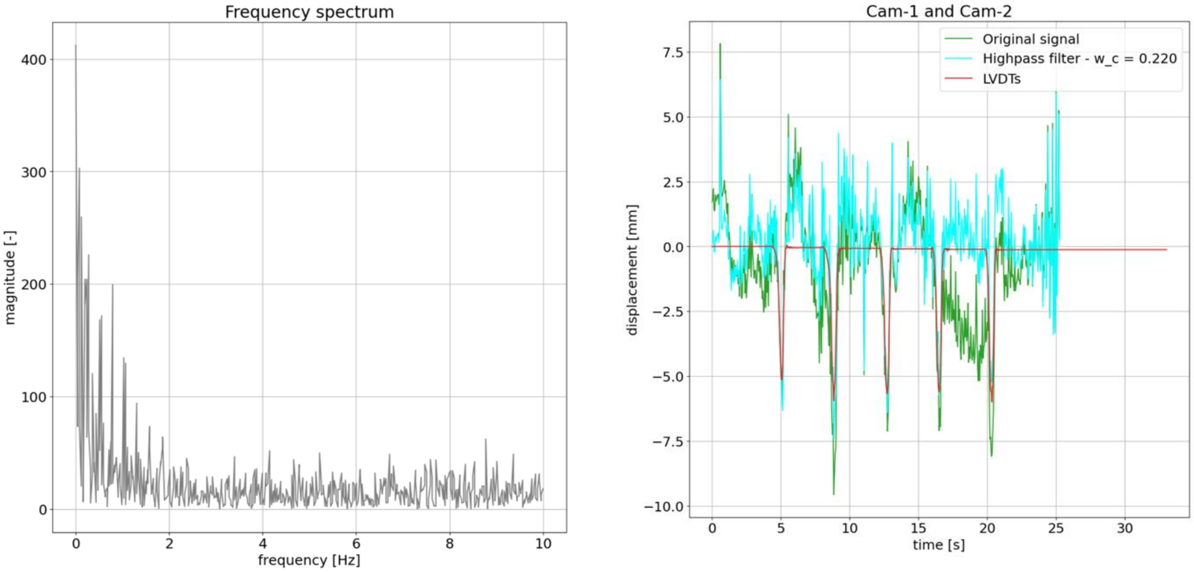

(a) Frequency Spectrum (b) High-pass Filter on Total Displacement

Figure 4.32. Signal Processing of Drone Total Displacement

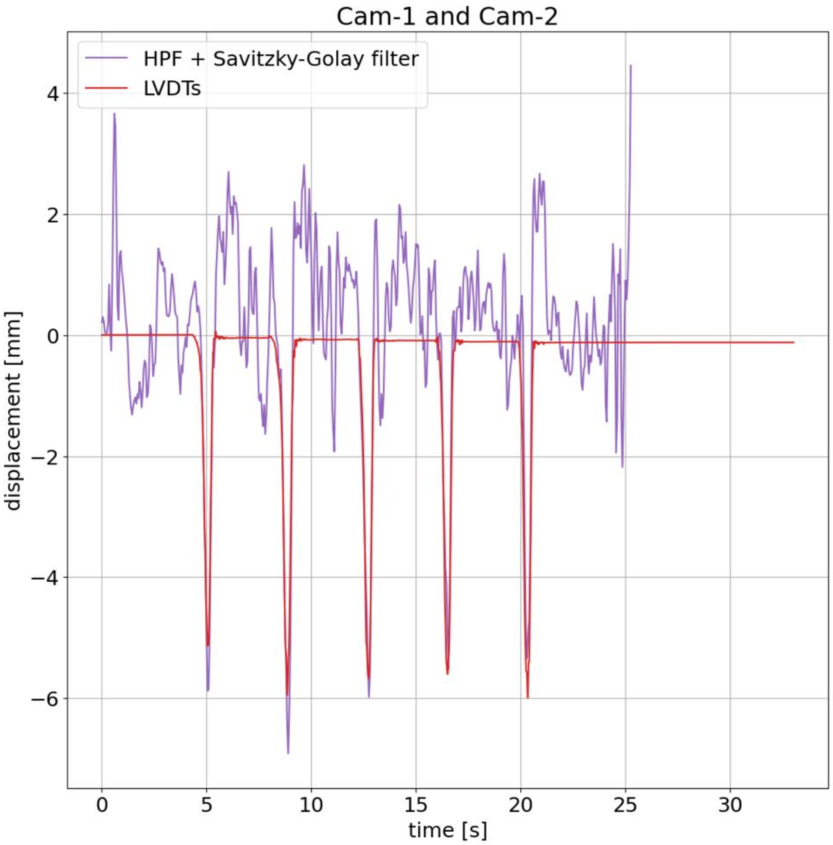

Figure 4.33. Drone Measured Total Displacement of Bridge after Applying High-Pass and Savitzky–Golay Filters

CHAPTER 5. SUMMARY AND CONCLUSIONS

5.1 Summary

More than 40% of the US in-service bridges are at least 50 years old, and the cost to repair the US bridges in their current condition is $125 billion. When a bridge is old or deteriorated, the evaluation of its load carrying capacity, usually referred to as "load rating", is necessary to ensure the safety of the traveling public and to prevent excessive damage and, possibly, collapse. Even though field testing offers actual insight into bridge behavior, it is not a common practice for bridge evaluation. Instead, analytical load rating is often used. One main reason is the cost associated with field operations. For bridge field testing, the cost is higher compared with an inspection due to the use of sensors, data acquisition system, test trucks, and data processing. One effective method to reduce the inspection cost is to utilize drones. Furthermore, digital image correlation (DIC) has been used to extract full-field structural displacements and strains from videos.

The main goal of the present study was to develop a novel solution for bridge field testing in which drones equipped with DIC cameras are used to measure bridge displacements, instead of conventional sensors. The results could then be used in load rating. To achieve the project goal, several cost-effective camera configurations were studied to determine the best camera candidates for use in the DIC-drone applications. Subsequently, different mission strategies were proposed in which a drone (or a fleet of drones) equipped with a set of cameras is deployed to perform bridge field testing using DIC techniques. A DIC system was developed using an open-source computer program and the best DIC marker was selected using a preliminary experimental study. A drone platform was then built using off-the-shelf hardware, aiming to prove the mission feasibility, and to reduce the total costs with respect to other commercial or professional drones available in the market. The accuracy of the proposed DIC-drone based displacement measurement tools was then evaluated by performing more than 70 tests on a truss bridge. Different camera configurations, test methods, and camera movement scenarios were included in the experimental study.

5.2 Conclusions

The following conclusions were drawn based on the experimental investigations:

- The proposed mission strategy C, in which one drone is equipped with two DIC cameras, was selected for tool development in this project since this method does not require a ground camera.

- The dimension of ArUco markers (or a cluster of markers) should be selected based on the distance of the marker from the camera and the lens focal length. The lens focal length affects the camera field of view (FOV) thus the marker/image fill factor (i.e., how big is the marker with respect to the full image).

- A DIC marker-based displacement measurement technique was developed in OpenCV, which can detect and estimate the pose of ArUco markers. In the proposed method, two DIC markers must be included, a target marker attached to the bridge, and a reference marker with zero displacements during bridge testing. The bridge vertical displacements are retrieved by measuring the relative displacement of the target marker with respect to the reference marker.

- A cluster of nine ArUco markers was found as the best candidate for use in bridge applications since they resulted in the least displacement errors. Furthermore, the use of a cluster of markers increased the accuracy of the displacement measurements by merging results from multiple markers at the same time. Another finding was that an increase in the orientation between camera and marker always adversely affected the displacement measurements. Parallel measurements (i.e., 0°) are recommended. Among all low-cost cameras, the Blackfly S USB3 camera exhibited the highest accuracy in displacement measurements than Intel RealSense D435i, Canon EOS 7D, and GoPro HERO4. Both Blackfly S USB3 and Raspberry Pi HQ, as a low-cost alternative to Blackfly, were included in the truss bridge model testing.

- Compared with conventional displacement sensors (LVDTs), Raspberry Pi HQ as the ground camera tracking the target marker on the truss bridge measured vertical displacements in the static tests with less than 1% error (equivalent to 0.08 mm or 0.003 in. displacement error) at 0° camera-to-marker inclination, 2% error (0.16 mm or 0.006 in. displacement error) at 22° inclination, and 3% error (0.24 mm or 0.009 in. displacement error) at 45° inclination.

- Compared with LVDTs, Raspberry Pi HQ as the ground camera tracking two markers in static tests measured displacements with less than 1% error at the peak load, which was equal to 0.09 mm (0.0035 in.) displacement error.

- Raspberry Pi HQ placed on the top of a moving cart tracking two markers in static tests exhibited large spikes in the DIC measurements during the cart movement. When the cart-camera system was not moving, the DIC displacement followed those of LVDTs with less than 1% error.

- Blackfly S placed on the top of a moving cart tracking two markers in static tests produced displacements that matched well those of LVDTs with less than 2% error at the peak load, which was equivalent to 0.18 mm (0.007 in.) displacement error. The Blackfly camera performed better than the Raspberry Pi HQ camera since no large spike in the displacement was seen when the Blackfly camera was used.

- Two unsynchronized ground cameras (Blackfly S and Raspberry Pi HQ) tracking the target and reference markers in the opposite directions in static tests resulted in less than 1% displacement error at the peak load. Nevertheless, the same two unsynchronized cameras mounted on an oscillating platform tracking the target and reference markers in static tests produced several spikes with large displacement errors. These tests showed that the lack of camera synchronization was the main source of large spikes and errors.

- Two synchronized ground Blackfly S cameras tracking the target and reference markers respectively at 117.5 mm (4.62 in.) and 1200 mm (47.27 in.) distance in static tests resulted in less than 3% displacement error at the peak load, which was equivalent to 0.24 mm (0.009 in.) displacement error.

- Two synchronized oscillating Blackfly S cameras tracking the target and reference markers both at 1200 mm (47.27 in.) distance in static tests resulted in less than 5% errors in displacements compared with those of LVDTs. Therefore, synchronization improves displacement measurements in a multi-camera DIC system.

- Two synchronized oscillating Blackfly S cameras tracking the target and reference markers both at 1200 mm (47.27 in.) distance in dynamic tests produced displacements with errors ranging from

2% (0.08 mm or 0.003 in.) to 15% (0.71 mm or 0.027 in.). When the reference marker was placed at further distance, the displacement error significantly increased.

- Two synchronized Blackfly S cameras mounted on a drone tracking the target and reference markers both at a 1500 mm (59.05 in.) distance in static tests measured displacements that had less than 5% errors (0.375 mm or 0.014 in. displacement error) compared with those of LVDTs. A low pass filter was used.

- Two synchronized Blackfly S cameras mounted on a drone tracking the target and reference markers both at 1500 mm (59.05 in.) distance in dynamic tests measured displacements with an error range of 1.53% (0.085 mm or 0.0033 in. displacement error) to 16.17% (0.96 mm or 0.037 in. displacement error). A high pass filter to remove signal noises and the Savitzky-Golay filter to smoothen the data were included.

Overall, the proposed DIC-drone based displacement measurement strategy and computational tools were found feasible with submillimeter level accuracies significantly advancing the state-of-the-art methodologies.

5.3 Future Works

Promising results were obtained using the proposed DIC-drone based displacement measurement method. Nevertheless, more work is needed to improve the accuracy and repeatability of the results. The DIC software should be tested in different environments and bridge configurations to understand its limitations. Cameras with a higher resolution or speed might be utilized to enhance measurement accuracy. Drone performance flying underneath bridges must be evaluated. Actual bridge field testing with the best camera-drone combination must be performed to fully evaluate the feasibility of the proposed DIC-drone based displacement measurement technique.

REFERENCES

AASHTO MBEI. (2013). “Manual for bridge element inspection (1st Edition) with 2015 Interim Revisions,” American Association of State Highway and Transportation Officials (AASHTO), 406 pp.

ASCE Report Card (2021). “The American society of civil engineers’ report card for America’s infrastructure,” https://infrastructurereportcard.org/.

Catt, S., Fick, B., Hoskins, M., Praski, J., and Baqersad, J. (2019). “Development of a semi-autonomous drone for structural health monitoring of structures using digital image correlation (DIC)”, Structural Health Monitoring, Photogrammetry & DIC, Vol. 6, DOI: 10.1007/978-3-319-74476-6_7.

Chajes, M. J., Shenton, H. W., & O’Shea, D. (2000). “Bridge-condition assessment and load rating using nondestructive evaluation methods”, Transportation Research Record, Vol. 1696, No. 1, pp. 83–91. https://doi.org/10.3141/1696-48

Chen, S., Laefer, D., Mangina, E., Zolanvariand, S. M. I., and Byrne, J. (2019). “UAV bridge inspection through evaluated 3D reconstructions”, Journal of Bridge Engineering, ASCE, Vol. 24, No. 4, 05019001, 10.1061/(ASCE)BE.1943-5592.0001343.

Chen, C., Liang, Q., Zhong, W., Gao, X., and Cui, F. (2021), “Homography-based measurement of bridge vibration using UAV and DIC method”, Measurement, Vol. 170, 108683, DOI: 10.1016/j.measurement.2020.108683.

Dong, C.Z., and Catbas, F.N. (2019). “A non-target structural displacement measurement method using advanced feature matching strategy”, Advances in Structural Engineering Vol. 22, No. 16, pp. 3461-3472. DOI:10.1177/1369433219856171.

Dong, C., Celik, O., Catbas, N., OBrien, E., and Taylor, S. (2019). “Structural displacement monitoring using deep learning-based full field optical flow methods”, Structure and Infrastructure Engineering, Vol. 16, pp. 1-21. DOI: 10.1080/15732479.2019.1650078.

Dong, C., Bas, S., and Catbas, N. (2020). “A portable monitoring approach using cameras and computer vision for bridge load rating in smart cities”, Journal of Civil Structural Health Monitoring, Vol. 10. DOI: 10.1007/s13349-020-00431-2.

Garnica, G.I.Z., Lantsoght E.O.L., and Yang, Y. (2022). “Monitoring structural responses during load testing of reinforced concrete bridges: a review”, Structure and Infrastructure Engineering, Vol. 18, No. 10-11, pp. 1558-1580, DOI: 10.1080/15732479.2022.2063906.

Holst, G. and Lomheim, T. (2011). “CMOS/CCD sensors and camera systems”, Second Edition, DOI: 10.1117/3.2524677.

Hoskere, V., Park, J-W., Yoon, H., and Spencer, B. (2019). “Vision-based modal survey of civil infrastructure using unmanned aerial vehicles”, Journal of Structural Engineering, Vol. 145, DOI: 10.1061/(ASCE)ST.1943-541X.0002321.

Islam, AKM.A., Li, F., Hamid, H., and Jaroo A. (2014). “Bridge condition assessment and load rating using dynamic response”, The Ohio Department of Transportation Office of Statewide Planning & Research, State Job Number 134695, 128 pp.

Issa, M.A., and Shahawy, M.A., (1993). "Dynamic and static tests of prestressed concrete girder bridges in Florida", Structural Research Center, MS 80 Florida Department of Transportation, 35 pp.

Jalinoos, F., Agrawal, A.K., Brooks C., Amjadian, M., Banach, D., Boren, E.J., Dobson, R., and Ahlborn, T. (2019). "Post-hazard engineering assessment of highway structures using remote sensing technologies", Minnesota Department of Transportation, 88 pp.

Khaloo, A., Lattanzi, D., Cunningham, K., Dell'Andrea, R. and Riley, M. (2018). "Unmanned aerial vehicle inspection of the Placer River Trail Bridge through image-based 3D modelling", Structure and Infrastructure Engineering, Vol. 14, No. 1, pp. 124-136, DOI: 10.1080/15732479.2017.1330891.

Khuc, T., Nguyen, T.A., Dao, H., and Catbas, F.N. (2020) "Swaying displacement measurement for structural monitoring using computer vision and an unmanned aerial vehicle", Measurement, Vol. 159, 107769, DOI: 10.1016/j.measurement.2020.107769.

Lattanzi, D., and Miller, G.R. (2014). "3D scene reconstruction for robotic bridge inspection", Journal of Infrastructure Systems, Vol. 21, 04014041. DOI: 10.1061/(ASCE)IS.1943-555X.0000229.

Lattanzi, D., Miller, G.R., Eberhard, M.O., and Haraldsson, O.S. (2015). "Bridge column maximum drift estimation via computer vision," Journal of Computing in Civil Engineering, ASCE, Vol. 30, No. 4, 04015051, 9 pp.

Liu, Y-F., Nie, X., Fan, J-S., Liu, X-G. (2020). "Image-based crack assessment of bridge piers using unmanned aerial vehicles and three-dimensional scene reconstruction", Computer Aided Civil Infrastructure; Vol. 35. Pp. 511-529, DOI: 10.1111/mice.12501.

Moreu, F., and Taha, M.M. (2018). "Railroad bridge inspections for maintenance and replacement prioritization using unmanned aerial vehicles (UAVs) with laser scanning capabilities", IDEA Program Transportation Research Board National Research Council, pp. 30.

Ngeljaratan, L., and Moustafa, M. A. (2020). "Structural health monitoring and seismic response assessment of bridge structures using target-tracking digital image correlation", Engineering Structures, Vol. 213, 110551, DOI: 10.1016/j.engstruct.2020.110551.

Nowak, A.S., and Saraf, V.K., (1996). "Load testing of bridges", Michigan Department of Transportation and Great Lakes Center for Truck and Transit Research, UMCEE 96-10, 144 pp.

Open Source Computer Vision - OpenCV, (2022a). "Detection of ArUco markers", URL: https://docs.opencv.org/4.x/d5/dae/tutorial_aruco_detection.html.

Open Source Computer Vision - OpenCV, (2022b). "Camera Calibration", URL: https://docs.opencv.org/4.x/dc/dbb/tutorial_py_calibration.html.

Perry, B.J., and Guo, Y. (2021), "A portable three-component displacement measurement technique using an unmanned aerial vehicle (UAV) and computer vision: A proof of concept", Measurement, Vol.176, 109222, DOI: 10.1016/j.measurement.2021.109222.

Phares, Brent & Wipf, Terry & Klaiber, Fred. (2005). "Implementation of physical testing for typical bridge load and superload rating", Transportation Research Record: Journal of the Transportation Research Board. 11s. DOI: 10.3141/trr.11s.5037130077853p72.

Popescu, C., Täljsten, B., Blanksvärd, T., and Elfgren, L. (2019). "3D reconstruction of existing concrete bridges using optical methods", Structure and Infrastructure Engineering, Vol. 15, No. 7, pp. 912-924, DOI: 10.1080/15732479.2019.1594315

Reagan, D., Sabato, A., and Niezrecki, C. (2017). "Feasibility of using digital image correlation for unmanned aerial vehicle structural health monitoring of bridges", Structural Health Monitoring: An International Journal, Vol 17. DOI: 10.1177/1475921717735326.

Rimal, S., Kidd, B., Tazarv, M., Seo, J., and Wehbe, N. (2019). “Methodology for load rating double-tee bridges”, Mountain-Plains Consortium, MPC 19-389, 232 pp.

Sanayei, M., Ford, A., Brenner, B., and Imbaro, R. (2015). “Load rating of a fully instrumented bridge: comparison of LRFR approaches”. Journal of Performance of Constructed Facilities, Vol. 30, No. 04015019. DOI: 10.1061/(ASCE)CF.1943-5509.0000752.

Schiff, S.D., Piccirilli, J.J., Iser, C.M., and Anderson, K.J., (2006). “Load testing for assessment and rating of highway bridges Phase III: Technology transfer to the SCDOT”, South Carolina Department of Transportation Research and Development Executive Committee, Research Project No. 655, 132 pp.

Suksawang, N. and Nassif, H. (2007). “Development of live load distribution factor equation for girder bridges”, Transportation Research Record, Vol. 2028, pp. 9-18. DOI:10.3141/2028-02.

Torres, V.J., (2016). “Live load testing and analysis of a 48-year-old double tee girder bridge”, MS Theses 4962, Utah State University, https://digitalcommons.usu.edu/etd/4962

Wells, J., and Lovelace, B. (2017). “Unmanned aircraft system bridge inspection demonstration project Phase II”, Minnesota Department of Transportation, 174 pp.

Wells, J., and Lovelace, B. (2018). “Improving the quality of bridge inspections using unmanned aircraft systems (UAS)”, Minnesota Department of Transportation, 345 pp.

Yoon, H., Shin, J., and Spencer, B. (2018). “Structural displacement measurement using an unmanned serial system”, Computer-Aided Civil and Infrastructure Engineering, Vol. 33, pp. 183-192. DOI: 10.1111/mice.12338.

Ziehl, P., Cousins, T., Ross, B., Huynh, N. (2020). “Assessment of structural degradation for bridges and culverts” South Carolina Department of Transportation, Federal Highway Administration, 151 pp.